Master's thesis

NTNU
Norwegian University of Science and Technology
Faculty of Natural Sciences
Department of Materials Science and Engineering

Jon Tobias Aga Karlsen

# Synthesis of Diatom-based $SiO_x$ Compounds and their Implementation on $SiO_x$/graphite Anodes for Lithium-ion Batteries

Master's thesis in Materials Science and Engineering
Supervisor: Maria Valeria Blanco
Co-supervisor: Weicheng Hua, Kesavan Thangaian, Ann Mari Svensson

June 2023

NTNU
Norwegian University of Science and Technology

Jon Tobias Aga Karlsen

# Synthesis of Diatom-based $SiO_x$ Compounds and their Implementation on $SiO_x$/graphite Anodes for Lithium-ion Batteries

Master's thesis in Materials Science and Engineering
Supervisor: Maria Valeria Blanco
Co-supervisor: Weicheng Hua, Kesavan Thangaian, Ann Mari Svensson
June 2023

Norwegian University of Science and Technology
Faculty of Natural Sciences
Department of Materials Science and Engineering

NTNU
Norwegian University of Science and Technology

# Preface

This thesis encompasses the work done in the course TMT4920 Materials Technology, Master's thesis, during the spring of 2023. I would like to thank my supervisor Adj. Assoc. Professor Maria Valeria Blanco for great support, motivation and help with both the laboratory work and writing of this thesis. I would also like to thank my co-supervisors Weicheng Hua and Kesavan Thangaian for support and assistance with laboratory work, writing and great conversations.

I would also like to acknowledge and thank Dr. Dmitry Chernysov and the team at the Swiss-Norwegian beamline at the European Synchrotron Radiation Facility for help, guidance and tips during the beamline experiment.

The Research Council of Norway is acknowledged for the support to project SUSTBATT 337463, project EPSABATT 315947 and the Norwegian Micro- and Nano-Fabrication Facility, NorFab, project number 295864.

The work is based and built upon the specialization project conducted during the fall of 2022. Most of the experimental work was done by the author, except for the magnesiothermic reduction and post reduction acid treatment, which was conducted by co-supervisor Kesavan Thangaian and Rietveld refinement was conducted by Pedro Alonso Sanchez of the University of Zaragoza. The in-situ synchrotron X-ray diffraction was an international collaboration between reasearch groups from NTNU and the University of Zaragoza, and I would like to express gratitude for the opportunity to join this beamline experiment.

Jon Tobias Aga Karlsen
Trondheim, June 2023

# Abstract

To meet the increasing demands of Li-ion batteries, combining $SiO_x$ with graphite into a composite anode has emerged as a promising option, benefiting from the high structural stability and excellent electrical conductivity in graphite, along with the high specific capacity of $SiO_x$. However, as the demand for Li-ion batteries is projected to increase alongside the need for a carbon neutral economy, the need for incorporating sustainable sourced raw materials for battery production is ever important.

In the current work, nanostructured $SiO_x$ compounds were obtained through magnesiothermic reduction of $SiO_2$ frustules from diatoms. For this, reaction parameters such as reaction temperature and molar ratio of reactants were adjusted. Synthesized $SiO_x$ compounds were characterized with a toolset of structural and electrochemical characterization techniques and successfully integrated into working anodes. Lastly, $SiO_x$/graphite anodes were fabricated, and their electrochemical performance was evaluated. In situ synchrotron X-ray diffraction experiments were performed on such $SiO_x$/graphite electrodes to track structural changes that $SiO_x$ and graphite components undergo during the two initial lithiation/delithiation reactions, with the goal of gaining insights on the effects of Si volume expansion on the graphite structure. The results from this work will serve to improve the cyclability of $SiO_x$/graphite composites and provides a facile pathway to obtain $SiO_x$ from sustainable sources.

The optimal parameters for magnesiothermic reduction were found and by using a Mg:$SiO_2$ molar ratio of 1:1 at a reaction temperature of 650°C, resulted in $SiO_x$ comprised of about 15% Si and about 85% $SiO_2$ after the post reduction acid treatment. The specific surface area of the frustules increased drastically from 85.4 $m^2g^{-1}$ in pristine $SiO_2$ frustules to 465.6 $m^2g^{-1}$ in the synthesized $SiO_x$, which is mainly attributed to the creation of new meso- and macropores in the material.

When implemented as active material in anodes, the $SiO_x$-based anode displayed a higher initial capacity of 1089 $mAhg^{-1}$ and coulombic efficiency of 89.2%, while lowering the initial capacity loss during the first cycles compared to that of 682 $mAhg^{-1}$ and 83.4% in anodes made with pristine $SiO_2$ frustules. However, the $SiO_x$-based anode experienced a continuous capacity decrease, with 805 $mAhg^{-1}$ in the $40^{th}$ cycle.

The $SiO_x$/graphite composite anode displayed a lower specific capacity than the pristine $SiO_x$ anode, but showcased better cycling stability, owing to the stabilizing

properties of graphite. Although the inclusion of $SiO_x$ was expected increase the anodes capacity, this was not observed, and the anode displayed a specific capacity of 402 $mAhg^{-1}$ after 40 cycles. Thus, further optimization of the $SiO_x$/graphite blend is needed.

In-situ synchrotron XRD on the $SiO_x$/graphite composite anode, revealed the distortion in the original lattice structure and amorphization of Si upon electrochemical cycling, whereas graphite maintained the original crystalline structure. The Si peaks were observed to shift towards higher and lower angles during electrochemical cycling, suggesting that Si and Li-ions form a solid solution before Si's phase transformations and amorphization occur.

# Sammendrag

For å møte den økende etterspørselen etter Li-ion-batterier, har kombinasjonen av $SiO_x$ med grafitt i en kompositttanode vist seg å være et lovende alternativ, ved å utnytte den høye strukturelle stabiliteten og den utmerkede elektriske ledningsevnen i grafitt, sammen med den høye spesifikke kapasiteten til $SiO_x$. Imidlertid, ettersom etterspørselen etter Li-ion-batterier forventes å øke sammen med behovet for en karbonnøytral økonomi, fremhever dette behovet for å inkludere bærekraftig råmaterialer i batteriproduksjon.

I dette arbeidet ble nanostrukturerte $SiO_x$-forbindelser oppnådd gjennom magnesiotermisk reduksjon av $SiO_2$-frustuler fra kieselalger. For dette ble reaksjonsparametere som reaksjonstemperatur og molforhold mellom reaktantene justert. Syntetiserte $SiO_x$-forbindelser ble karakterisert med et sett av strukturelle og elektrokjemiske karakteriseringsteknikker og ble integrert vellykket i anoder. Til slutt ble $SiO_x$/grafitt-anoder fabrikkert, og deres elektrokjemiske ytelse ble evaluert. In situ synkrotron røntgendiffraksjon ble utført på slike $SiO_x$/grafitt-elektroder for å spore strukturelle endringer som $SiO_x$- og grafittkomponenter gjennomgår under de to første litierings/delitierings-reaksjonene, med mål om å få innsikt i effektene av volumekspansjon av Si på grafittstrukturen. Resultatene fra dette arbeidet vil hjelpe til med å forbedre syklisiteten til $SiO_x$/grafitt-kompositttene og gir en enkel vei for å oppnå $SiO_x$ fra bærekraftige kilder.

De optimale parameterne for magnesiotermisk reduksjon ble funnet, og ved å bruke et Mg:$SiO_2$-molforhold på 1:1 ved en reaksjonstemperatur på 650°C, ble $SiO_x$ , som bestod av ca 15% Si og ca 85% $SiO_2$ etter syrebehandling, syntetisert. Det spesifikke overflatearealet til frustulene økte drastisk fra 85,4 $m^2g^{-1}$ i $SiO_2$-frustuler til 465,6$m^2g^{-1}$ i det syntetiserte $SiO_x$, som i hovedsak kommer av nye meso- og makroporer dannet under reaksjonen.

Når $SiO_x$ ble implementert som aktivt materiale i anoder, så viste den $SiO_x$-basert anoden en høyere startkapasitet på 1089 $mAhg^{-1}$ og koulombisk effektivitet på 89,2%, mens det opprinnelige kapasitetstapet ble redusert under de første syklusene sammenlignet med 682 $mAhg^{-1}$ og 83,4% i anoder laget med $SiO_2$-frustuler. Imidlertid opplevde den $SiO_x$-baserte anoden en kontinuerlig kapasitetsnedgang, med 805 $mAhg^{-1}$ i den 40. syklusen.

$SiO_x$/grafitt-kompositttanoden viste en lavere spesifikk kapasitet enn $SiO_x$-anoden, men viste bedre syklingsstabilitet, grunnet de stabiliserende egenskapene til grafitt.

Selv om implementeringen av $SiO_x$ forventet å øke anodens kapasitet, ble dette ikke observert, og anoden viste en spesifikk kapasitet på 402 $mAhg^{-1}$ etter 40 sykluser. Som dermed viser at det er et behov for ytterligere optimalisering av $SiO_x$/grafitt-blandingen.

In-situ synkrotron XRD på $SiO_x$/grafitt-kompositttanoden, avslørte forvrengningen i den opprinnelige gitterstrukturen og amorfisering av Si under elektrokjemisk sykling, mens grafitt opprettholdt sin opprinnelige krystallinske strukturen. Si-toppene ble observert å skifte mot høyere og lavere vinkler under elektrokjemisk sykling, noe som antyder at Si og Li-ioner danner en fast løsning før fasetransformasjoner og amorfisering oppstår i Si.

# Table of Contents

**Preface** i

**Abstract** iii

**Sammendrag** v

**List of Figures** x

**List of Tables** xiv

**List of Abbreviations** xv

**1 Introduction** 1

**2 Theory** 5

2.1 Galvanic cells and secondary batteries . . . . . 5

2.1.1 Fundamentals of Li-ion batteries . . . . . 5

2.1.2 Terminology in battery literature . . . . . 7

2.2 Components of a cell . . . . . 11

2.2.1 Anode materials . . . . . 11

2.2.2 Electrode binder . . . . . 14

2.2.3 Electrolyte and solid electrolyte interface . . . . . 14

2.3 Silicon anodes . . . . . 16

2.4 $SiO_2$ Anodes . . . . . 18

2.4.1 Lithiation of $SiO_2$ . . . . . 18

2.4.2 $SiO_2$ anodes in literature . . . . . 19

2.5 $SiO_x$ anodes . . . . . 20

2.5.1 Lithiation mechanism of $SiO_x$ . . . 20
2.6 $SiO_x$/graphite composite anodes . . . 21
2.6.1 Electrochemical behavior of composite anodes . . . 22
2.7 $SiO_x$ from sustainable sources . . . 22
2.7.1 Diatoms as a sustainable $SiO_2$ source and $SiO_x$ precursor . . . 22
2.8 Magnesiothermic reduction of $SiO_2$ . . . 24
2.9 Characterization techniques . . . 26
2.9.1 Electrochemical characterization techniques . . . 26
2.9.2 Structural characterization techniques . . . 27
2.10 Half-cell configuration for lab scale experiments . . . 32

**3 Experimental** **34**

3.1 Diatom species . . . 34
3.2 Magnesiothermic reduction of $SiO_2$ . . . 35
3.2.1 Characterization of $SiO_x$ . . . 36
3.3 Anode manufacturing, cell assembly and characterisation . . . 37
3.3.1 Slurry and binder preparation . . . 37
3.3.2 Assembly of cells . . . 39
3.3.3 Anode characterization . . . 40
3.4 In situ XRD analysis . . . 41
3.4.1 Assembly of in-situ cells . . . 41
3.4.2 Experimental setup . . . 41
3.4.3 Data processing . . . 42

**4 Results** **45**

4.1 Overview . . . 45

4.2 Magnesiothermic reduction . . . . . 45
4.2.1 XRD . . . . . 45
4.2.2 Surface area . . . . . 48
4.2.3 SEM & EDS . . . . . 50
4.3 Anode & Electrochemical characterization . . . . . 53
4.3.1 $SiO_x$-based anodes . . . . . 54
4.3.2 $SiO_x$/graphite composite anodes . . . . . 58
4.3.3 Comparison of anodes with different active material . . . . . 60
4.4 In-situ XRD . . . . . 63

**5 Discussion** **68**

5.1 Effect of magnesiothermic reduction on diatom silica . . . . . 68
5.1.1 Structure and microstructure after reduction . . . . . 68
5.1.2 Effect on specific surface area . . . . . 69
5.1.3 Effect of temperature at constant molar ratio . . . . . 70
5.1.4 Effect of molar ratio at constant temperature . . . . . 71
5.1.5 Effect of acid treatment on reduced diatoms . . . . . 71
5.1.6 Effect of heat scavenger agent . . . . . 71
5.2 Electrochemical performance . . . . . 72
5.2.1 $SiO_x$ anodes . . . . . 72
5.2.2 $SiO_x$/graphite composite anodes . . . . . 74
5.2.3 Comparison of cells with different active materials . . . . . 76
5.3 In-Situ XRD . . . . . 77

**6 Conclusion** **81**

**7 Further Work** **84**

**Bibliography** **85**

**Appendix** **96**

**A Mass loading of cells** **96**

**B Additional SEM micrographs** **96**

**C Additional EDS** **97**

# List of Figures


2.1 A simplified schematic of a conventional Li-ion battery, with the direction of Li-ions (green spheres) and electrons during discharge shown. 7

2.2 Illustration of a voltage profile/galvanostatic cycling curve with a higher cut-off potential of 2.00 V and a lower cut-off potential of 0.002 V 26

2.3 Differential capacity curve based on Figure 2.2. . . . . 27

2.4 XRD diffractograms . . . . . 30

2.5 Schematic of the *operando* cell. Reused with permission from [90]. . . 31

2.6 Electrode with free-standing electrode in the middle from a) top and b) bottom. . . . . 31

3.1 SEM micrographs of a frustule from diatom Species A. . . . . 34

3.2 As recieved diatom frustule powder of Species A . . . . . 34

3.3 Schematic step by step of the magnesiothermic reduction process. . . 35

3.4 Perforated Cu foil and electrode cast on the foil. . . . . 39

3.5 Schematic of the different parts and their order when assembling coin cells. . . . . 40

3.6 Setup for in-situ XRD. . . . . 42

3.7 Steps in data processing. . . . . 43

3.8 Several diffractograms obtained from data processing. . . . . 43

4.1 Diffractogram obtained of pristin $SiO_2$ frustules. . . . . 45

4.2 XRD diffractograms of $SiO_x$ samples at the different reduction temperatures at a constant molar ratio of a) 2.5:1 and b) 5.3:1 . . . . . 46

4.3 XRD diffractograms of $SiO_x$ samples at different molar ratios and a constant reduction temperature of 650°C, where a) depicts samples before acid treatment and b) acid treated samples. . . . . 47

4.4 Diffractograms of pristine $SiO_2$ and $SiO_x$ before and after acid treatment, where AT denotes the acid treated sample. . . . . 48

4.5 Barplot showing the BET surface area and t-plot external and micropore area of pristine $SiO_2$ frustules and acid treated $SiO_x$. . . . . 49

4.6 Isotherms of pristine $SiO_2$ frustules and $SiO_x$, obtained by BET analysis. . . . . 50

4.7 Pore volume and differential pore volume as a function of pore width for a) pristine $SiO_2$ frustules and b) $SiO_x$ . . . . . 50

4.8 SEM microgrpahs of pristine $SiO_2$ frustules. . . . . 51

4.9 SEM micrographs of diatom frustules post MgTR. . . . . 52

4.10 SEM micrographs of diatom frustules post MgTR and acid treatment. 52

4.11 SEM micrograph and EDS maps of $SiO_x$ particles post MgTR. EDS maps acquired from area marked with red. . . . . 53

4.12 SEM micrograph and EDS maps of $SiO_x$ particles post MgTR and acid treatment. EDS maps acquired from area marked with red. . . . 53

4.13 SEM micrographs of FIB cut conducted on uncycled $SiO_x$ anode. b) shows a higher magnification of the red square in a). . . . . 54

4.14 SEM micrographs of FIB cut conducted on uncycled $SiO_x$/graphite anode. b) shows a higher magnification of the red square in a) . . . . 54

4.15 Voltage profile of $SiO_x$-based cell showing a) activation cycle at 50 $mAg_{-1}$ and 2nd cycle at 100 $mAg^{-1}$, and b) subsequent cycles at 100 $mAg^{-1}$ . 55

4.16 DC curve of $SiO_x$-based cell showing a) activation cycle at 50 $mAg_{-1}$ and 2nd cycle at 100 $mAg^{-1}$, and b) subsequent cycles at 100 $mAg^{-1}$ . 55

4.17 Voltage profile of $SiO_x$-based cell without activation cycle, showing a) 1st and 2nd cycle at 100 $mAg^{-1}$, and b) subsequent cycles at 100 $mAg^{-1}$ 56

4.18 DC curve of $SiO_x$-based cell without activation cycles, showing a) 1st and 2nd cycle at 100 $mAg^{-1}$, and b) subsequent cycles at 100 $mAg^{-1}$ . 56

4.19 Voltage profile of $SiO_2$-based cell showing a) activation cycle at 50 $mAg_{-1}$ and 2nd cycle at 100 $mAg^{-1}$, and b) subsequent cycles at 100 $mAg^{-1}$ . 57

4.20 DC curve of $SiO_2$-based cell showing a) activation cycle at 50 $mAg_{-1}$ and 2nd cycle at 100 $mAg^{-1}$, and b) subsequent cycles at 100 $mAg^{-1}$ . 57

4.21 Voltage profile of $SiO_x$/graphite-based cell showing a) activation cycle at 50 $mAg_{-1}$ and 2nd cycle at 100 $mAg^{-1}$, and b) subsequent cycles at 100 $mAg^{-1}$ . . . . . 58

4.22 DC curve of $SiO_x$/graphite-based cell showing a) activation cycle at 50 $mAg_{-1}$ and 2nd cycle at 100 $mAg^{-1}$, and b) subsequent cycles at 100 $mAg^{-1}$ . . . . . 59

4.23 Voltage profile of $SiO_x$/graphite-based cell without activation cycle, showing a) 1st and 2nd cycle at 100 $mAg^{-1}$, and b) subsequent cycles at 100 $mAg^{-1}$ . . . . . 60

4.24 DC curve of $SiO_x$-based cell without activation cycles, showing a) 1st and 2nd cycle at 100 $mAg^{-1}$, and b) subsequent cycles at 100 $mAg^{-1}$ . 60

4.25 Discharge capacity as function of cycle number for the different cell compositions. Cells that underwent an activation cycle at 50 $mAg^{-1}$ is denoted with an A and cells that started cycling directly at 100 $mAg^{-1}$ is denoted NA. . . . . 62

4.26 Coulombic efficiency as function of cycle number for the different cell compositions. Cells that underwent an activation cycle at 50 $mAg^{-1}$ is denoted with an A and cells that started cycling directly at 100 $mAg^{-1}$ is denoted NA. . . . . 63

4.27 Results obtained by in-situ XRD of the first discharge/charge cycle, with a) a GC curve with time against potential, and diffractograms depicting the 2θ ranges of b) 10.8-13.5°, c) 18.5-20.0° and d) 20.0-22.0°. Peaks of interested are marked with a dotted red line. . . . . 64

4.28 Results obtained by in-situ XRD of the second discharge/charge cycle, with a) a GC curve with time against potential, and diffractograms depicting the 2θ ranges of b) 10.8-13.5°, c) 18.5-20.0° and d) 20.0-22.0°. Peaks of interested are marked with a dotted red line. . . . . 65

4.29 Results obtained by in-situ XRD of the first discharge/charge cycle, with a) a GC curve with time against potential, and diffractograms depicting the 2θ ranges of b) 24.5-25.5°, c) 30.0-30.5° and d) 32.5-34.0°. Peaks of interested are marked with a dotted red line. . . . . 66

4.30 Results obtained by in-situ XRD of the second discharge/charge cycle, with a) a GC curve with time against potential, and diffractograms depicting the 2θ ranges of b) 24.5-25.5°, c) 30.0-30.5° and d) 32.5-34.0°. Peaks of interested are marked with a dotted red line. . . . . 66

B.1 SEM micrographs of agglomerated diatom frustules post MgTR. . . . 96

B.2 SEM micrographs of agglomerated diatom frustules post MgTR and acid treatment. . . . . 97

C.1 Map sum spectra corresponding to the EDS maps of post MgTR $SiO_x$ given in Figure 4.11. The unmarked peak in between Si and Mg belongs to Al, originating from the sample holder. . . . . 97

C.2 Map sum spectra corresponding to the EDS maps of post MgTR and acid treated $SiO_x$ given in Figure 4.12. The unmarked peak in between Si and Mg belongs to Al, originating from the sample holder. 98

C.3 SEM micrograph and EDS maps of $SiO_x$ particles of the second synthesis with 1:1 molar ratio at 650°C post MgTR. EDS maps acquired from area marked with red. . . . . 98

C.4 Map sum spectra corresponding to the EDS maps of post MgTR $SiO_x$ given in Figure C.3. . . . . 99

C.5 SEM micrograph and EDS maps of $SiO_x$ particles of the second synthesis with 1:1 molar ratio at 650°C post MgTR and acid treatment. EDS maps acquired from area marked with red. . . . . 99

C.6 Map sum spectra corresponding to the EDS maps of post MgTR and acid treatment $SiO_x$ given in Figure C.5. . . . . 100

# List of Tables


2.1 Overview of reported capacities of anodes with modified Si as active material. . . . . 17

2.2 Overview of reported capacities of anodes with $SiO_2$ as active material. 19

2.3 Overview of reported capacities of anodes with $SiO_x$ as active material. 20

2.4 Overview of reported capacities of anodes with $Si/SiO_x$/graphite as active material. . . . . 21

3.1 Experimental conditions including sample identification, molar ratio of magnesium to silica, and temperature. The temperature ramp rate for all samples are 2°C/min . . . . . 36

4.1 Phases and amount present in the samples after MgTR, based on Rietveld refinement. N.O. denotes that the phase was not observed in the Rietveld refinement. . . . . 47

4.2 Phases and amount present in the samples after MgTR and acid treatment, based on Rietveld refinement. . . . . 48

4.3 BET surface area, t-plot external area and t-plot micropore area for pristine $SiO_2$ frustules and acid treated $SiO_x$. . . . . 49

4.4 Capacities during charge and discharge during the first and second cycle, initial capacity loss and coulombic efficiency for the different cell compositions. Cells that underwent an activation cycle at 50 $mAg^{-1}$ is denoted with an A and cells that started cycling directly at 100 $mAg^{-1}$ is denoted NA. . . . . 61

4.5 Capacities during charge and discharge during the 5th and 40th cycle and coulombic efficiency for the different cell compositions. Cells that underwent an activation cycle at 50 $mAg^{-1}$ is denoted with an A and cells that started cycling directly at 100 $mAg^{-1}$ is denoted NA. . . . . 61

A.1 Active material mass loading of different cell compositions. Cells that underwent an activation cycle at 50 $mAg^{-1}$ is denoted with an A and cells that started cycling directly at 100 $mAg^{-1}$ is denoted NA. The table also includes the mass loading for the anode used in the in-situ cell. . . . . 96

# List of Abbreviations

AM Active material

BET Brunauer-Emmet-Teller

CB Carbon black

CCL Cumulative capacity loss

CE Coulombic efficiency

DE Diatomaceous earth

DI-water Distilled water

EDS Energy dispersive x-ray spectroscopy

EV Electric vehicle

FIB Focused ion beam

ICL Initial capacity loss

LIB Lithium ion battery

MgTR Magnesiothermic reduction

PSD Particle size distribution

Redox Reduction-oxidation

SEI Solid electrolyte interface

SEM Scanning electron microscopy

SSA Specific surface area

$V_{OC}$ Open circuit voltage

XRD X-ray diffraction

# 1 Introduction

The escalating necessity for sustainable energy solutions, amplified by the shift from oil and coal towards renewable alternatives, has become a significant point of focus in the last decades. In this context, the implementation of large scale solar power plants and wind farms, together with a transition to electrically powered vehicles (EVs), are key to make use of renewable and sustainable energy sources, and are therefore regarded as crucial for the transition towards greener energy. However, this also creates the necessity for high energy density storage systems [1].

Since the first commercialization in 1991 by Sony, the Lithium-ion batteries (LIBs) have been the energy storage technology of choice [2]. The anode of choice for LIBs have been graphite, due to its balance of low cost, stable cycle life and abundance. However, graphite has a theoretical capacity of only $372\,\mathrm{mAhg^{-1}}$, which has been deemed insufficient for the next generation of LIBs. By 2030 it is estimated that the entire LIB value chain will grow to over 400 billion USD and have a market size of 4.7 TWh [3]. It is therefore imperative to find suitable alternatives to graphite.

Amongst promising alternatives, Silicon has emerged as a potential candidate, owing to its staggering theoreticel capacity of $4200\,\mathrm{mAhg^{-1}}$ [4]. Although it appears attractive, Si-based anodes suffer from short cycling life and rapid deterioration, due to structural changes and significant volume expansion during lithiation/delithiation [5]. In order to address these challenges, research has gravitated towards $SiO_2$. Having multiple of the same benefits as Si, but without the drawbacks. $SiO_2$ in contrast with Si, is shown to have a greater cycling stability, due to the formation of lithium oxides and silicates, which buffers the volume expansion [6]. It also presents with a relatively high theoretical capacity of $1961\,\mathrm{mAhg^{-1}}$ and previous work has reported a reversible specific capacity of $1055\,\mathrm{mAhg^{-1}}$ after 150 cycles at $500\,\mathrm{mAg^{-1}}$[7]. However, $SiO_2$-based anodes needs to tailored with micro and nano structures, as the bulk material shows low reactivity against Li-ions. Synthetic processes for producing nanostructured $SiO_2$ frameworks often require toxic and expensive precursors [8], leading the focus to finding natural and sustainable sources of nano structured $SiO_2$.

Recent research have found promise in diatoms, or microalgaes, as sustainable feedstock for nano- to microstructured $SiO_2$ architectures, and experimental reports on the implementation of such $SiO_2$ structures as active material of LIB's anodes have shown promising results [9]–[12]. Diatoms are a type of hard-shelled photosynthetic

organism found in both marine and fresh water, which build exoskeletons (frustules) of $SiO_2$. These diatoms demonstrate a diverse array of shapes, dimensions, and nano structures, thereby presenting a wide range of morphological options to choose from [13]. In 2019 Norberg *et al.* reported a specific capacity of 723 $mAhg^{-1}$ at 200 $mAg^{-1}$ using $SiO_2$ from sea water diatom frustules [10]. In the project work conducted by the author during the fall semester 2022, it was found that $SiO_2$ from industrially cultivated diatoms can reach specific capacities of about 790 $mAhg^{-1}$ at 100 $mAg^{-1}$ [14]. However, $SiO_2$ still suffers from high irreversible capacity loss and low conductivity [15].

To further enhance the nano structure of the diatom frustules, attempts at reducing the $SiO_2$ to Si and $SiO_x$ have been conducted. $SiO_x$ have shown to display the promising attributes of $SiO_2$, but also avoid its drawbacks, such as high irreversible capacity loss and less volume expansion [15]. For commercialization, the drawbacks associated with Si/$SiO_x$-based anodes are still too significant. Therefore, the implementation of these materials into graphite anodes have become a point of research. Combining the higher capacities of $SiO_x$ with the high stability and conductivity of graphite [16].

The need for a fine nanostructure is still important in the $SiO_x$ material. So to avoid collapse of the intricate nano structures, magnesiothermic reduction (MgTR) has been found as feasable method, due to relatively low reduction temperatures. Luo *et al.* demonstrated that diatom frustules can successfully be reduced to porous Si through the MgTR process [17] and has thus shown by tailoring the reduction parameters, synthesis of $SiO_x$ is within reach.

## Aim of this work

$SiO_x$/graphite blends have become a promising option for benefiting from the large electrical conductivity and high structural stability of graphite, together with the high specific capacity of $SiO_x$, therefore enabling the production of high energy density and durable anodes for next-generation LIBs. However, expected increase in demand for LIBs along with need for a climate neutral economy, makes the supply of battery raw materials a strategic challenge at a global level and evidences the need to incorporate suistainably sourced battery components.

Previous findings have demonstrated that nanostructured $SiO_2$ extracted from diatoms, are a viable option for producing sustainable anodes for LIBs, and to benefit

from such natural structures in schemes of battery technology it is imperative to fabricate understoichiometric $SiO_x$ compounds from them. Also, the structural and electrochemical impact of $SiO_x$ compounds in $SiO_x$/graphite blends is still not fully understood, and this hinders a rational design of high capacity and stable anode materials.

The goal of this work is to produce high performance $SiO_x$/graphite composite anodes for LIBs using a sustainable $SiO_2$ precursor. To achieve this, the first goal is to produce $SiO_x$ compounds from $SiO_2$ diatom frustules. The selection of $SiO_2$ frustules was made based on the results obtained from the specialization project conducted by the author [14], in which a comparative analysis of the structural, microstructural and electrochemical properties of frustules from two individual diatom species was performed for the first time. Then, the effect of different reaction parameters, such as temperature and molar ratio of reactants, on the magnesiothermic reduction of amorphous $SiO_2$ frustules for the production of $SiO_x$ compounds will be investigated using X-ray diffraction and SEM/EDS analysis. Finally, the electrochemical properties of $SiO_x$ as active material will be analyzed and compared with the electrochemical performance of the starting $SiO_2$ compound. The second goal of this work is to integrate synthesized $SiO_x$ into $SiO_x$/graphite blends and to investigate its electrochemical performance using electrochemical characterization techniques, in-situ synchrotron X-ray diffraction and FIB/SEM cross-sectional analysis. Such analysis allow to gain valuable insights into structural changes occurring on the graphite matrix as a consequence of lithiation and delithiation of the $SiO_x$/graphite composite, and structural changes occurring on the crystalline Si domains upon electrochemical cycling.

# 2 Theory

## 2.1 Galvanic cells and secondary batteries

At a fundamental level, a battery is an electrochemical cell that can store energy and convert chemical energy to electrical energy. The spontaneous conversion from chemical energy to electrical energy happens due to the reduction-oxidation (redox) reaction happening at each of the two electrodes in the cell. The cell itself consists of the two electrically isolated electrodes, the anode and cathode, separated by an electrolyte. By convention, the anode is the site of the oxidation reaction and the cathode is the site of the reduction reaction [2].

Due to the reversibility of some redox reactions, electrical energy can be used to reverse the electrochemical reactions in a cell and charge it to its initial state. Therefore battery technology has been divided into two main categories; primary and secondary batteries. A primary battery is an electrochemical cell that will only deliver electrical energy once, since the redox reactions in this type of cell are irreversible. For a secondary battery, the redox reactions are partially reversible and allows for it to be charged up again by applying electrical energy to the cell [2], [18].

During charging and discharging of a secondary battery, the electrodes will alternate between hosting the reduction and the oxidation reaction. Meaning that the cathode and anode will switch between during discharge and charge [2], [18]. In this thesis for consistency and ease of reading, the anode will refer to the electrode hosting the oxidation reaction during discharge and cathode the electrode hosting the reduction reaction during discharge.

Battery technology is an area of active research and the use of secondary battery technology in various application has been going on for several decades [19]. With the growing market of small and portable consumer electronics and the shift to an EV-based transport industry [20], LIB technology has become a point of interest and grown to be one of the most dominant secondary battery technologies.

### 2.1.1 Fundamentals of Li-ion batteries

As LIBs are one of the most dominant secondary battery technologies on the market and also the major focus of this thesis, this section will go into the fundamental principles of the LIB. LIBs utilizes the $Li^+$ ion as the charge carrier, flowing between

the electrodes, giving it the name "rocking chair battery" or "swing battery". In LIBs, the major components are; an anode, a cathode, an electrolyte and a separator [2], [21].

For a general Li-ion battery consisting of a graphite anode and a $LiCoO_2$ (LCO) cathode (two of the most commonly used anode and cathode materials), the reactions during charge and discharge are as follows [2], [22]:

$$\text{Anode: } 6C + xLi^+ + xe^- \rightleftharpoons Li_xC_6 \tag{2.1a}$$

$$\text{Cathode: } LiCoO_2 \rightleftharpoons Li_{1-x}CoO_2 + xLi^+ + xe^- \tag{2.1b}$$

$$\text{Total cell reaction: } LiCoO_2 + 6C \rightleftharpoons Li_{1-x}CoO_2 + Li_xC \tag{2.1c}$$

Figure 2.1 shows a simplified schematic of the above described battery during discharge. The direction of Li-ions (green spheres) and electrons in the external circuit is shown with arrows. During the discharge, Li-ions flow from the anode through the electrolyte and separator to the cathode, and in reverse when the battery is charged. In order to guarantee ionic mobility the electrolyte has to be an ionic conductor, while simultaneously exhibiting a low electric conductivity. The separator also has to have proper ionic conductivity as well as being electrically insulating. This is to ensure that the electrons from the redox reactions travel through the external circuit and to prevent physical contact between the electrodes, which would cause a short-circuit of the cell. The electrodes of the cell are connected to the external circuit via current collectors. These establish good contact between the electrodes and the external, while not interfering with chemistry of the cell [21]. Cu foil at the anode and Al foil at the cathode are the most common materials currently used as current collectors commercially [23].

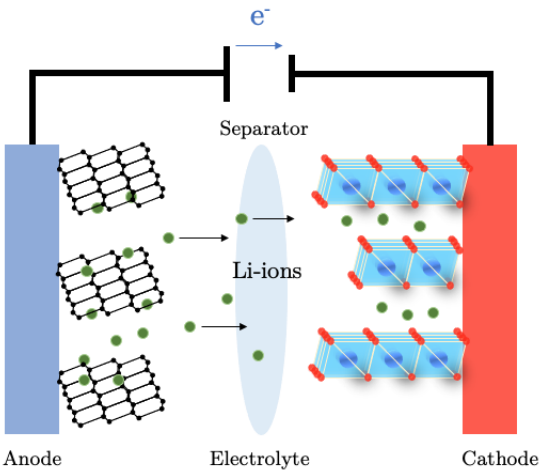


**Figure 2.1:** A simplified schematic of a conventional Li-ion battery, with the direction of Li-ions (green spheres) and electrons during discharge shown.

### 2.1.2 Terminology in battery literature

Several parameters describing batteries and their performance have been standardized by the scientific community regarding battery technology. The parameters are divided into mainly three categories; the amount of power a battery can deliver, the amount of energy a battery is able to store and the life time of a battery.

#### Energy

The available amount of energy in a battery is equal to the charge transferred during the redox reactions described in eq. 2.1 and the potential for the individual charge transfer. The total amount of energy and the charging process is given by [21];

$$\text{Energy} = \int_0^Q V(q)dq \tag{2.2}$$

where V(q) is the potential when a charge q is transferred form one electrode to the other, and Q is the total charge in the process.

### Capacity

The capacity (Q) of a battery is described by the total amount of charge that a battery can stored and is given by [21];

$$Q(I) = \int_0^{\Delta t} I dt = \int_0^{Q} dq \tag{2.3}$$

where I is given by the applied current in Ampere (A) and t is time, in seconds, as the current is applied. The capacity is described by Coulombs (C), but more commonly used is Ampere-hours (Ah), which is equal to 3600 C.

The theoretical capacity ($Q_{th}$) of an electrode with a known material and mass can be calculated by;

$$Q_{th} = \frac{nF}{M_w} \tag{2.4}$$

where n is the number of transferred electrons, F is the Faraday constant, given by 96485 As/mol, and $M_w$ is the molecular weight of active mass on the electrode in g/mol [24].

### Cell voltage

The voltage of a full cell, the open circuit voltage ($V_{OC}$), is described by the difference in the electrochemical potential of the anode and cathode, and is given by [21];

$$V_{OC} = \frac{\mu_a - \mu_c}{e} \tag{2.5}$$

where $\mu_a$ and $\mu_c$ are the electrochemical potentials at the anode and cathode respectively, and $e$ is the electron charge.

### Energy density of batteries

The total amount of energy stored in a battery is given by Equation 2.2, but for more practical purposes it is often more beneficial to use parameters describing the amount stored per unit weight or volume. Therefore the energy density is often given as either the gravimetric or volumetric energy density, which is expressed by [21];

$$\text{Gravimetric energy density} = \frac{\int_0^Q V(q)dq}{wt} \tag{2.6}$$

$$\text{Volumetric energy density} = \frac{\int_0^Q V(q)dq}{vol} \tag{2.7}$$

### Power density of batteries

The power density of a battery is a useful parameter in regards to consumer electronics, electric vehicles and power tools. The power density is calculated by multiplying the potential, V(q), with the discharge current, $I_{dis}$, shown in [2];

$$P(q) = V(q) \cdot I_{dis} \tag{2.8}$$

By then taking P(q) and dividing it on the volume of a given battery, the volumetric power density of the given battery can be found, shown in;

$$\text{Volumetric power density} = \frac{P(q)}{vol} \tag{2.9}$$

### Internal resistance

During operation, a battery will experience an internal resistance ($R_b$) in the ionic current during discharge, lowering the output voltage $V_{dis}$ from the open circuit volatage $V_{OC}$ by a polarization given by $\theta = I_{dis}R_b$. While, when charging, the opposite occurs and the resistance will increase the voltage to $V_{ch}$ by an overvoltage given by $\eta = I_{ch}R_b$. The equations can be written as [21];

$$V_{dis} = V_{OC} - I_{dis}R_b \tag{2.10a}$$

$$V_{ch} = V_{OC} + I_{ch}R_b \tag{2.10b}$$

### Battery efficiency and life time

The life time of a battery cell is by convention established as the total amount of cycles the battery can handle before the capacity is reduced to below 80% of the initial reversible value. The loss of capacity in a battery can be described by the coulombic efficiency (CE) or by the irreversible capacity loss (ICL), which are given by [21];

$$\text{CE} = 100 \cdot \frac{Q_{dis}}{Q_{ch}} \tag{2.11}$$

$$\text{ICL} = Q_{ch} - Q_{dis} \tag{2.12}$$

where $Q_{dis}$ and $Q_{ch}$ are the capacities of the battery during discharge and charge, respectively in the same cycle. Over multiple cycles, the cumulative capacity loss (CCL) can be described by;

$$\text{CCL} = \sum_k Q_{ch} - Q_{dis} \tag{2.13}$$

where k is the number of cycles for the battery.

### C-rate

The C-rate is a useful term used to describe the charge or discharge current in order to normalize data against the capacity given by a battery. With given C-rate, denoted by nC, it indicates that the battery will be fully charged/discharged in 1/n hours. Thus, a battery charging/discharging at 1C will be fully charged/discharged in 1 hour. A battery with a capacity of e.g. 100 Ah will have a charge current of 100 A [2].

## 2.2 Components of a cell

The most basic components of a battery cell are the two electrodes, the anode and cathode, and an electrolyte. This section will provide an introduction to the different components in a Li-ion battery relevant to this thesis.

### 2.2.1 Anode materials

The different materials used for anodes in Li-ion batteries are categorized primarily based on the lithiation/delithiation mechanisms. There are three main types of anodes; intercalation anodes, alloying anodes and conversion anodes. This section serves to provide fundamental theory on how the three different mechanisms work with related materials.

#### Intercalation anodes

Intercalation anodes are materials that operate on the reversible reaction of inserting a guest ion or molecule into its lattice structure, without alteration of the basic lattice structure [2]. The material often has a stable layered or tunnel crystal structure, which presents pathways for the guest ions to diffuse [25]. For commercial use, graphite is one of the most utilized materials, and the reversible lithiation reaction of graphite is given by;

$$C_6 + Li^+ + e^- \rightleftharpoons LiC_6 \tag{2.14}$$

Graphite has been the material of choice for LIBs due to its incomparable balance of abundance, low cost and a long and stable cycle life. The specific capacity available in graphite anodes is also very close to the reversible theoretic capacity of $372\,mAhg^{-1}$ [25]. Graphite also presents with good electrical and Li-ion conductivity, and a low insertion voltage of $\approx 0.2\text{-}0.05\,V$ vs $Li/Li^+$. Another carbon based intercalation anode is amorphous carbon. The theoretical capacity is over $900\,mAhg^{-1}$, much higher than graphite, but the material suffers from a low density and extensive formation of a solid electrolyte interface (SEI) layer [26].

In addition to graphite, titanium oxide-based anodes , such as $Li_4Ti_5O_{12}$ (LTO) and $TiO_2$ [22], are considered to be viable intercalation anode alternatives. LTO has a spinel structure, meaning it can store Li-ions without any associated volume

expansion, and is therefore seen as a "zero strain" material [27]. LTO also presents with a high operating voltage of $\approx 1.5\,\mathrm{V}$ vs $\mathrm{Li/Li^+}$, which prevents the growth of Li dendrites, and hence improves the safety during operation. The drawbacks of using LTO instead of graphite, are the lower theoretical capacity of $175\,\mathrm{mAhg^{-1}}$ and low conductivity.

### Alloying anodes

The second type of anode, the alloying anode, is based on Li forming alloys with several different metals and metalloids. The alloying mechanism, in contrast to the intercalation mechanism, is based on the breaking and reforming of atom bonds in the host material. The general reaction of an alloying anode can be written as [2];

$$\mathrm{M + xLi^+ + xe^- \rightleftharpoons Li^+M} \tag{2.15}$$

where the element M is a metal or metalloid, often Sn, Si, P or Ge [28]. The mechanism of breaking and reforming of bonds in alloying anodes leads to a greater Li-ion storage capacity than the previously mentioned intercalation anode. In the Li-Si system, the $\mathrm{Li_{4.4}Si}$ phase has been reported to have a theoretical capacity of $4200\,\mathrm{mAhg^{-1}}$ [2], [29]. Silicon has been studied intensely as an anode replacement for graphite and will be discussed further in section 2.3. The alloying mechanism also comes with its drawbacks. The breaking and reforming of atom bonds cause significant structural changes in the host material, often leading to pulverization of the host material and poor cycling stability [29].

### Conversion anodes

The third category of anode, the conversion anode, relies on conversion reactions between lithium binary transition metal compounds and are looked upon as a suitable replacement for the more common intercalation anode. Conversion anodes display good cycling capabilities, high theoretical capacities and are commonly low in cost. The general conversion reaction mechanism can be expressed as [2], [22];

$$\mathrm{M_xX_y + ynLi^+ + yne^- \rightleftharpoons xM + yLi_nX} \tag{2.16}$$

where $M_xX_y$ is the binary transition metal compound (where often M = Fe, Si, Co, Cu, Ni and Mn and X = O, P and S [30]) and n is the oxidation state of the anion X. In similarity with alloying anodes, conversion anodes struggles with internal structural changes that could lead to pulverization of the material at particle level. In addition, conversion anodes often suffers from large voltage hysteresis. The hysteresis is likely due to a interconversion of multiple solid phases ($Li_2O$, M and $MO_x$) breaking strong chemical bonds and Li, M and O ions having long diffusion pathways to be able to form single particle domains [22]. $SiO_2$, which is a major focus of this thesis, is an example of a conversion anode [15] and will be discussed further in Section 2.4.

### Prerequisites of anode materials

In order to ensure safe operation, expected longevity, and sustainability of anodes, it is imperative that the materials meet certain criteria. These criteria, as outlined by Julien [2], encompass six key requirements that materials under consideration for anode use must satisfy:

1. The material should be light and be able to accommodate as much Li as possible to enhance the gravimetric capacity of the anode.
2. The redox potential against $Li/Li^+$ should be as small as possible at any given concentration of Li. Since given eq. 2.5, this potential is subtracted to the redox potential of the cathode to give the overall cell voltage, meaning a lower voltage gives a higher energy density in the cell.
3. The ionic and electronic conductivity of the material should be good to allow faster motion of Li-ions, giving a higher power density.
4. The material should be inert and not react with the electrolyte salts or solvents in the electrolyte.
5. The material must tolerate heat and mechanichal abuse, i.e. thermal runaway. Especially important with batteries used for transportation, such as EV's, planes and electric boats.
6. The material should meet the criteria of sustainability, including societal, environmental and economic aspects.

Graphite, the most commercially used anode today, meets some of the aforementioned criteria. Despite that, graphite only has a theoretical capacity of 372 $mAh\,g^{-1}$, meaning it only satisfies requirement 1 to a certain degree [25]. Along with the challenges of dendrite growth and Li deposition in graphite anodes, efforts have been made to find new materials that better meets these criteria.

### 2.2.2 Electrode binder

An electrode binder is used in the fabrication of electrodes to maintain good adhesion and contact between particles in the active material, and as well with the current collector. Today the most conventionally used binder in Li-ion batteries is poly(vinyleden fluoride) (PVDF), however it have been found to be unsuitable in anodes made with Si and $SiO_2$ [31]. When used with Si based anodes, PVDF forms weak van der Waals bonds to the Si particles, which easily breaks during cycling due to the drastic volume expansion of Si. To solve this issue, research on alternative binders has led to polymeric binders containing hydroxyl and carboxylic groups, such as alginate (Alg), carboxymethyl cellulose (CMC) and polyacrylic acid [32]. Si anodes prepared with these polymeric binders show greater cycling stability, due to the binders being less rigid than PVDF and binding more strongly towards Si particles [31]. These polymeric binders are also soluble in water, compared to PVDF, which is dissolved in NMP, making them less toxic to the environment and more sustainable [33]. In recent a study by Primo *et al.* it was found that the pH of aqueous binder solutions greatly effect the stability and performance of Si anodes [31]. Therefor in this thesis, Na-Alg dissolved in KCA, a buffer solution with $pH = 3$, is used as a binder in the electrode production.

### 2.2.3 Electrolyte and solid electrolyte interface

The electrolyte in a battery serves as the conduit for ion transport between the electrodes [34]. It is crucial that the electrolyte remains stable in relation to the electrode surfaces, as it is considered to be an inert component within the battery system [25]. Kang Xu outlined a set of key properties that an electrolyte should ideally possess to ensure stability [25]:

1. It should be an effective ionic conductor yet simultaneously function as an electrical insulator to facilitate ion mobility while preventing electron migration that could cause self-discharge.

2. The electrolyte should exhibit a broad electrochemical window, i.e. a wide voltage range within which it resists oxidation and reduction.

3. It must remain inert and refrain from interacting with the cell packaging material, the electrode constituents, and the separator.

4. It should endure electrical, thermal, mechanical, and chemical abuse.

5. Ideally, it should be environmentally friendly and non-toxic to humans and other life forms.

Ionic conductivity, which characterizes the ability of the electrolyte to facilitate ion transport, can be expressed as:

$$\sigma = \sum_i n_i u_i Z_i e \tag{2.17}$$

Where $n_i$ denotes the number of moles of free ions, $u_i$ signifies ion mobility, $Z_i$ refers to the valence number of the ionic species $i$, and $e$ is the elementary charge. The ionic conductivity has been found to reach a saturation point with around a concentration of 1 M of salt. Any further increment in concentration affects the parameter $n_i$ in Equation 2.17, increasing viscosity, and thereby decreasing ionic mobility within the electrolyte. Consequently, most electrolytes have a critical salt concentration that optimizes the ionic conductivity [35].

The electrochemical window, which defines the thermodynamic stability of the electrolyte, is determined by the energy gap ($E_g$) between the lowest unoccupied molecular orbital (LUMO) and the highest occupied molecular orbital (HOMO). To ensure electrochemical stability, the battery's electrochemical potentials must reside within this window. However, this condition is rarely met in high-voltage batteries, as their open-circuit voltages often lie outside the window of commonly used electrolytes. This leads to the formation of the passivating SEI layer, thereby substituting thermodynamic stability with kinetic stability [36]. The SEI, composed of both insoluble and partially soluble components, arises from the reduction reactions of Li with the electrolyte solution. It functions similar to a solid-state electrolyte with high electronic resistivity, permitting ion current while impeding electronic current to the electrode. As the SEI directly influences the battery's power capability, cycle life, safety, and morphology of Li deposits, while simultaneously deterring electrolyte decomposition, a thorough understanding and effective control of the SEI formation is crucial. [25].

**Electrolyte salts and solvents**

The composition of the electrolyte, involving a variety of salts, additives, and solvents, is carefully tailored to meet the criteria in the aformentioned section. The selection of specific components depends on the material system in question. Lithium hexafluorophosphate ($LiPF_6$) is among the most widely used salts in contemporary research and industry, attributed to its balanced properties. Despite its popularity, $LiPF_6$ presents a number of challenges. Specifically, when exposed to moisture, a situation indicative of cell contamination, this salt can undergo a reaction to yield hydrofluoric acid (HF), as shown in the equation below [36]:

$$LiPF_6 \rightleftharpoons LiF + PF_5 \tag{2.18}$$

$$PF_5 + H_2O \rightharpoonup 2HF + PF_3O \tag{2.19}$$

HF acid is a potent reactant with the potential to compromise the stability of the electrolyte, through the ring-opening polymerization of ethylene carbonate (EC), and initiate corrosive processes within the cell.

Employing a blend of solvents enables the fulfillment of the primary requisites of an electrolyte. Commonly usec solvents include linear carbonates, such as dimethyl carbonate (DMC) and diethyl carbonate (DEC), and cyclic carbonates, like ethylene carbonate (EC) and propylene carbonate (PC). Within the electrolyte, the linear carbonates contribute to lowering the viscosity and the melting point, while the cyclic carbonates facilitate the dissolution of the electrolyte salt [25].

## 2.3 Silicon anodes

Anodes based on silicon (Si) have been widely studied in the last decades for the partial or total replacement of graphite in negative electrodes for next generation LIBs. This surge in interest is fueled by several advantageous properties that Si displays, in accordance with the criteria listed in Section 2.2.1. Among the most relevant properties Si displays as anode active material we can list [4], [37]:

1. An impressively high gravimetric capacity of $4200\,mAhg^{-1}$ for the $Li_{4.4}Si$ compound, which exceeds that of conventional graphite anodes by an order of magnitude.

2. A redox potential relative to $Li/Li^+$ of approximately 0.4 V.

3. Si is the second most abundant element in Earth's crust, thus ensuring plentiful supply. Additionally, it is environmentally benign and non-toxic, which increases the sustainability of batteries that incorporate it.

Although Si appears as an attractive material to improve the energy density in negative electrodes for LIBs, it suffers from several issues that are related to the alloying-dealloying reaction with Li-ions. During the lithiation of Si, the material undergoes significant structural changes, which can induce a volume expansion of up to 400% [5]. This excessive volume change can contribute to several detrimental phenomena in the anode [4]:

1. The mechanical integrity of the anode could be compromised due to pulverization caused by repeated charge/discharge cycles.

2. The physical contact between the anode and the current collector may be disrupted due to the interfacial stress generated by the volumetric changes.

3. Li-ions may be continuously depleted due to the formation, destruction, and reformation cycle of the SEI layer on the anode.

Moreover, Si may suffer from inherently low electronic conductivity and sluggish kinetics, which can compromise its overall electrochemical performance [38]. To mitigate the issues associated with Si anodes, researchers have begun investigating several strategies including decreasing particle size, nano-structuring and developing comoposite electrodes [37]. An overview of different strategies with reported capacities can be viewed in Table 2.1

**Table 2.1:** Overview of reported capacities of anodes with modified Si as active material.

| Material | Current density [$mAg^{-1}$] | Reversible capacity [$mAhg^{-1}$] | Cycles |
|---|---|---|---|
| Chitosan covered nano-Si [39] | 1000 | 1500 | 400 |
| Diatom-derived nano-Si [40] | 700 | 1102 | 50 |
| Carbon coated Si nanofiber [41] | 4000 | 802 | 659 |
| Si@SiOx@C nanoparticles [42] | 1000 | 1030 | 500 |

## 2.4 $SiO_2$ Anodes

As a response to resolve the issues faced by Si-based anodes, $SiO_2$ has emerged as a promising anode candidate for LIBs. Si and $SiO_2$ share many similarities, attributed to them being products of each other's reduction and oxidation process [43]. It was long thought that $SiO_2$ was electrochemically inactive in batteries, however a study by Gao *et al.*in 2001 found that nanoparticles of $SiO_2$ were reactive towards $Li^+$ between potentials of 0.0 V and 1.0 V [44]. Further studies have estimated that $SiO_2$ has a theoretical reversible capacity of up to 1961 $mAhg^{-1}$ depending on the lithiation mechanism [8]. Anodes manufactured with $SiO_2$ also display great cycling stability [45]. Coupled with being low in cost, generally non-toxic and being abundant, $SiO_2$ anodes have become important as potential anode material for next-generation LIBs [46]. However, $SiO_2$ still faces challenges related to low conductivity, high irreversible capacity loss during initial cycling and a volume expansion, due to Si still being present [8], [45].

### 2.4.1 Lithiation of $SiO_2$

The lithitation mechanism of $SiO_2$ was first proposed in 2008 by Sun *et al.* and further expanded by Chang and Guo *et al.* resulting in the following reactions [8], [43], [47]:

$$5SiO_2 + 4Li^+ + 4e^- \rightleftharpoons 2Li_2Si_2O_5 + Si \tag{2.20a}$$

$$3SiO_2 + 4Li^+ + 4e^- \rightleftharpoons 2Li_2SiO_3 + Si \tag{2.20b}$$

$$2SiO_2 + 4Li^+ + 4e^- \rightleftharpoons 2Li_4SiO_4 + Si \tag{2.20c}$$

$$SiO_2 + 4Li^+ + 4e^- \rightleftharpoons 2Li_2O + Si \tag{2.20d}$$

$$Si + xLi^+ + xe^- \rightleftharpoons Li_xSi \tag{2.20e}$$

In the proposed lithiation/delithiation, the reaction of $SiO_2$ leads to the formation of electroactive Si domains, together with reversible and irreversible conversions to lithium oxide and lithium silicates. These reaction products would act as a physical barrier against the huge volume expansions of Si during lithiation, hence serving as a buffer for volume changes and as structural support to the anode, and therefore resulting in a larger cycling stability of the electrode. The discussion of whether

$SiO_2$ is a sufficient ion conductor or not is still undergoing. $Li^+$ diffusion in $SiO_2$ is reported to be prevented, due to $SiO_2$ generally being considered as an ionic insulator [15]. However it has been found that when certain conversion products, such as $Li_4SiO_4$ and $Li_2Si_2O_5$, are present, $Li^+$ diffusion increases [46].

To address the challenges related to conductivity in $SiO_2$ anodes, research has focused on conductive coatings and additives. Among silicon-oxide based materials, $SiO_2$ possesses the lowest conductivity [15]. Due to their low cost, carbon coating approaches are widely utilized to increase the electronic conductivity of $SiO_2$ particles, while also preserving the their surface from direct contact with the electrolyte [48]. As well as coating, carbon can be used as an conductive additive to the electrode matrix, often in the form of carbon black (CB) or graphene. When using additives, they should be homogeneously dispersed within the electrode matrix, to ensure contact between the particles of active material.

### 2.4.2 $SiO_2$ anodes in literature

As described in the aforementioned section, $SiO_2$ reduces to electroactive domains of Si during lithiation, meaning the challenges related to Si based anodes, also apply to $SiO_2$ based anodes. Several different approaches have been explored to mitigate these challenges, such as synthesis of porous structures and particle size control. An overview of reported capacities from different literature can be found in Table 2.2. In the literature, research on $SiO_2$ and under-stoichiometric silicon oxides ($SiO_x$, where $0 < x < 2$) are discussed partly interchangeably. This section will focus on stoichiometric $SiO_2$ as an anode material and the latter will be further explored in Section 2.5.

**Table 2.2:** Overview of reported capacities of anodes with $SiO_2$ as active material.

| Material | Current density [$mAg^{-1}$] | Reversible capacity [$mAhg^{-1}$] | Cycles |
|---|---|---|---|
| $SiO_2$-graphene aerogel [49] | 500 | 300 | 300 |
| Hollow porous $SiO_2$ nanocubes [50] | 100 | 919 | 30 |
| $SiO_2$ nano spheres [51] | - | 877 | 500 |
| Submicron $SiO_2$ [52] | 100 | 602 | 150 |
| Porous $SiO_2$/C composite [53] | 100 | 560 | 30 |

## 2.5 $SiO_x$ anodes

Silicon suboxides, $SiO_x$ where $0 < x < 2$, have gained traction the last decade as a promising anode material for the next generation of LIBs [54]. However, in literature, the reports on anodes made with $SiO_x$ vary from core-shell structures of Si and $SiO_2$, simple mixing of Si and $SiO_2$ and homogeneous $SiO_x$ particles [55]. Early on, research on pure $SiO_x$ anodes has been focused on how varying amounts of oxygen affects the anodes electrochemical performance [15]. In 2002, Yang *et al.* were one of the first to study the properties of amorphous $SiO_x$ with varying oxygen content. With the use of X-ray photoelectron spectroscopy (XPS) measurements, they determined the presence of crystalline Si, amorphous $SiO_2$ and SiO [56]. It was found that lower amounts of oxygen enhanced the reversible capacity and they reported a capacity of 1600 $mAhg^{-1}$ at a current density of 0.2 $mAcm^{-2}$. Since then different manufacturing strategies have been conducted to enhance the performance of $SiO_x$-based anodes. An overview of reported capacities is presented in Table 2.3.

**Table 2.3:** Overview of reported capacities of anodes with $SiO_x$ as active material.

| Material | Current density [$mAg^{-1}$] | Reversible capacity [$mAhg^{-1}$] | Cycles |
|---|---|---|---|
| $SiO_x$ [57] | 750 | 1862 | 200 |
| $Si/SiO_x$ composite [58] | 100 | 980 | 100 |
| Hollow $Si/SiO_x$ nanospheres [59] | 0.1C | 1290 | 100 |
| Porous $SiO_x$ [60] | 0.2C | 1240 | 100 |

### 2.5.1 Lithiation mechanism of $SiO_x$

Similar to $SiO_2$, the lithiation/delithiation mechanism of $SiO_x$ has been intensely researched [60]–[62]. Using high resolution transmission electron microscopy (HRTEM), Yu *et al.* studied the reaction mechanisms of an SiO anode [60]. Based on these findings, Zhang *et al.* has proposed a lithitation/delithiation mechanism for the first cycle [63]:

$$SiO_x + 2xLi^+ + 2xe^- \rightarrow xLi_2O + Si \tag{2.21a}$$

$$SiO_x + (x/z)Li^+ + (x/z)e^- \rightarrow (x/z)LiSi_yO_z + (1\text{-}xy/z)Si \tag{2.21b}$$

$$Si + xLi^{x} + xe^{-} \rightleftharpoons Li_xSi \ (x \leq 4.4) \tag{2.21c}$$

As with $SiO_2$, the reactions lead to the formation of $Li_xSi$, $Li_2O$ and lithium silicates. These compounds would act similarly as they do in $SiO_2$ anodes and work as a buffering layer for the volume expansion of Si during cycling, as well as suppressing the continuous SEI formation [63]. By varying the oxygen amount in the $SiO_x$, the formation of these compunds could be easier to control, to gain favorable electrochemical perfomance in $SiO_x$ anodes.

## 2.6 $SiO_x$/graphite composite anodes

Even though research on Si and $SiO_x$ based anodes has come far, these compounds still have a way to go for being implemented in commercial use. So to exploit the favorable traits these materials present, resaerchers have tried to implement Si and $SiO_x$ into graphite based anodes, to enhance them for next generation of LIBs [64]. It is reported that introducing Si or $SiO_x$ in graphite anodes, will increase the specific capacity [65]–[67], and the graphite could help alleviating some of the volume expansion in the electroactive Si [68]. In the literature there are mainly two types of Si/$SiO_x$/graphite anodes reported; 1) Blended anodes and 2) synthesized Si/$SiO_x$/graphite composite materials. An overview of reported capacities and method of fabrication is given in Table 2.4.

**Table 2.4:** Overview of reported capacities of anodes with Si/$SiO_x$/graphite as active material.

| Material | Fabrication method | Current density [$mAg^{-1}$] | Reversible capacity [$mAhg^{-1}$] | Cycles |
|---|---|---|---|---|
| Carbon-coated Si/graphite [65] | Blended | 130 | 712 | 100 |
| Watermelon Si/C-Microspheres [67] | Spray drying | 0.5C | 620 | 500 |
| SEAG [69] | CVD | - | 525 | 50 |
| Porous Si/C-graphite [70] | CVD | 0.4 $mAcm^{-2}$ | 650 | 450 |
| $SiO_x$-graphite [16] | Blended | 0.05C | ≈ 630 | 30 |

### 2.6.1 Electrochemical behavior of composite anodes

When combining $Si/SiO_x$ with graphite, it is crucial to consider the capacity contributions of each component due to their different potential ranges [63]. The process of lithiation occurs in stages, with Si being lithiated before graphite at approximately 0.21 V [71]. Graphite undergoes lithiation at 0.12 V and 0.083 V, while Si lithiation takes place in between at 0.1 V during the stage transitions of graphite, and further lithiation of Si occurs at 0.053 V. Hence, a significant portion of the capacity from Si is accessed prior to reaching 0.2 V during lithiation [71].

## 2.7 $SiO_x$ from sustainable sources

As noted in Section 2.3, Si is the second most abundant element in the crust of the Earth, which hence means $SiO_2$ is readily available. However, as a bulk material, $SiO_2$ has been shown to exhibit low reactability towards Li [43]. Amorphous forms, such as thin films, have demonstrated to display some reactivity towards Li, but the manufacturing process often suffers from complex procedures, requiring high cost precursors [8], and therefore hampering the process of manufacturing viable and sustainable Si and $SiO_x$ for LIBs. In the search for more sustainable sources for $SiO_2$ with the necessary attributes, several options have been reported. In 2012 Liu *et al.* reported the use of rice husks as $SiO_2$ source and precursor for Si nano particles (SiNPs) for use in anodes for LIBs. The anodes displayed a high reversible capacity of 2790 $mAhg^{-1}$ at C/50 rate and 1750 $mAhg^{-1}$ at C/2 rate, and a capacity retention of 95% after 200 cycles [72]. In 2015 Liu *et al.* explored the use of reed leaves as a $SiO_2$ precursor and fabricated anodes that displayed a specific capacity of 420 $mAhg^{-1}$ at a 10C rate for 4000 cycles [73]. Another $SiO_2$ source that has gained traction in recent years are diatoms, or microalgae.

### 2.7.1 Diatoms as a sustainable $SiO_2$ source and $SiO_x$ precursor

Diatoms, a type of microalgae, are unicellular organisms who use biomineralization to create frustules, made of $SiO_2$. Worldwide, there is estimated to be over 100 000 different species in both fresh and sea water, displaying an array of different shapes, sizes and structures. The diatoms have a naturally occurring structure at both the micro and nano scale, which are desired traits for $SiO_2$ based materials in anodes [13], [74]. General for all diatoms, is the basic structure consisting of two halves

made from hydrated $SiO_2$ [74] and a connecting girdle [75].

Diatomite, also referred to as diatomaceous earth (DE), has been studied as a suitable anode material for LIBs, as it displays an ordered nano porous structure, high $SiO_2$ content and high availability [76]. DE is found in the soil, and is essentially fossilized algae which has been there for a over millions of years [40]. In tandem with being used as a raw material for $SiO_2$ anodes, it has been used as a precursors and templates for Si/C composite anodes, which have displayed capacities up to $\approx 820\,mAhg^{-1}$ after 30 cycles at $50\,mAg^{-1}$ [40], [77]. DE has been used as a source material for making low cost nanostructure $SiO_2$ anodes, achieving capacities of $575\,mAhg^{-1}$ at $100\,mAg^{-1}$ after 100 cycles [11]. However, this $SiO_2$ source suffers from to main drawbacks, its low surface area [75] and a lower porosity [78], which are attributed to damage of the sieve plate of the diatom after an extended period of time in the earth.

Nanostructured frustules can also be gathered from living diatoms, which have either been industrially cultured or harvested from nature. The diatom frustules display ordered micro and nano structures which are far beyond what is possible by lab synthesis [74]. The naturally occurring porous structure is advantageous in several ways, providing rapid diffusion paths for $Li^+$ ions and having sufficient space for the volume expansion of Si during lithiation [15]. Also, these diatoms rely on photosynthesis to grow [13], and interestingly, due to their single-cell nature, diatoms are highly efficient solar converters [79], exhibiting a higher $CO_2$ uptake rate than forests [80] and generating about 25% of the planetary oxygen. Hence, the use of diatom $SiO_2$ feedstock for producing sustainable anodes for LIBs will actively contribute to capture $CO_2$.

In the recent years, research on frustules from living diatoms has been conducted. In 2019, Norberg *et al.* demonstrated the use sea water diatom frustules as active material in composite anodes reaching capacities of $723\,mAhg^{-1}$ at $200\,mAg^{-1}$ [10]. Nowak *et al.* found in 2020 that $SiO_2$@C anodes made from laboratory cultivated diatom frustules could be prepared. They achieved a capacity of $460\,mAhg^{-1}$ at $40\,mAg^{-1}$. In 2021, another study by Wang *et al.* used a mixture of frustules from different diatom species achieving a discharge capacity of $\approx 1000\,mAhg^{-1}$ at $200\,mAg^{-1}$. However, each specie would present a distinctive morphology, which would lead to differences in surface area, porosity and nanostructure, and therefore it is not possible to evaluate the effect of frustules of each specie on the electrochemical performance on the anodes. In the specialization project conducted by

the author during the fall of 2022, frustules from two different diatom species that were individually cultured, were implemented as active material of $SiO_2$ anodes [14]. This enabled to understand the effect of the frustule's properties on electrochemical performance, which was found to be species-dependent. Based on the results, frustules from one of the species was chosen to used as $SiO_2$ precursor for manufacturing $SiO_x$ through magnesiothermic reduction.

## 2.8 Magnesiothermic reduction of $SiO_2$

As mentioned the aformentioned sections, $SiO_x$ can be manufactured by magnesiothermic reduction (MgTR) of $SiO_2$. MgTR is an efficient, cheap and scalable method for fabrication of micro- and nano structured Si for LIB applications [81] [57]. Traditional methods of manufacturing Si, such as carbothermic reduction (CTR), often requires temperatures as high as 2000°C during the reduction process. For applications in LIB, the nano-/microstructure is of utmost importance to the electrical properties of the material and the high temperatures of CTR can lead to degradation and collapse of these structures. Due to the MgTR being highly exothermic, it can operate at low temperatures at around 650°C, just above the melting point of Mg [81]. At these relatively low temperatures, control of nano-/microstructures from precursors is easier to maintain. Several researchers have focused their attention to nanostructured Si manufactured from the MgTR process from different $SiO_2$ precursors. In 2012 Liu *et al.*[72] prepared Si nanoparticles (SiNPs) from rice husks as the $SiO_2$ precursor maintaining the intricate nano structures of the original material. In 2013, Luo *et al.* demonstrated that it is possible to prepare nano porous Si from diatom $SiO_2$ frustules [17].

The reaction at equilibrium can be described by Equation 2.22, where one mole of $SiO_2$ reacts with two moles of Mg to form one mole of Si and two moles of MgO. If excess Mg is available during the reaction $Mg_2Si$ is formed according to Equation 2.23 or if there is a Mg deficiency, $Mg_2SiO_4$ is formed according to Equation 2.24 [82].

$$SiO_2 + 2Mg = 2MgO + Si \quad \Delta G^0_{1373} = \text{-}243.4 \text{ kJ} \tag{2.22}$$

$$SiO_2 + 4Mg = 2MgO + Mg_2Si \quad \Delta G^0_{1373} = \text{-}272.1 \text{ kJ} \tag{2.23}$$

$$SiO_2 + Mg = 0.5Mg_2SiO_4 + 0.5Si \quad \Delta G^0_{1373} = \text{-}146.4 \text{ kJ} \tag{2.24}$$

The magnesium by-products from the reduction process can be removed with acid treatment. The most dominant byproduct MgO can be removed relatively easy with HCl acid treatment, leaving behind a porous Si structure. $Mg_2Si$ and $Mg_2SiO_4$ can be removed by a mixture of HCl and HF acid, but this may lead to formation of $SiF_4$, which is toxic [81]. In this thesis only HCl is utilized for the removal of magnesium byproducts to avoid formation of toxic compounds and to improve sustainability aspects in the MgTR process.

As mentioned, the MgTR reaction is highly exothermic and substantial amounts of heat is released. Therefor the temperature inside the reactor vessel could reach up to a few hundred degrees more than the initial set reaction temperature [57] [17]. These heightened temperatures could lead to collapsing of desired nanostructures, found in the precursor materials used, as well as formation of unwanted magnesium byproducts as mentioned earlier. To avoid issues, different inorganic salts, such as KCl, NaCl and CaCl, can be used to effectively absorb the excess heat from the exothermic reaction. Generally NaCl and KCl are thought to be the best heat scavengers for mass use, due to their high specific heat capacity, ease of handling and low cost. The salts absorb heat by self-fusion during the reduction process and allows the nano-/microstructure in the $SiO_2$ and Si to be preserved. After the reaction, the salts are easily removed by HCl acid treatment. In this thesis NaCl as a heat scavenger is utilized in some of the samples in an attempt to tailor the MgTR process.

To obtain $SiO_x$ from the MgTR process, careful control of all reaction parameters in the MgTR process is needed [58] [57]. Tailoring the process to produce SiOx with desired traits, such as nanostructures, specific surface area and oxygen content, is necessary in the search for high-performing anodes for LIBs. Tailoring of temperature, molar ratio between $SiO_2$ and Mg is one of the main parts of this thesis.

## 2.9 Characterization techniques

### 2.9.1 Electrochemical characterization techniques

#### Galvanostatic cycling

The electrochemical performance of a battery can be be characterized by the means of galvanostatic cycling (GC). This technique allows for characterization of a battery's capacity and reversibility, and cycling can be conducted under practical conditions, i.e. room-temperature. Cycling consists of subjecting the cell to a constant current until an upper voltage limit, $V_2$, is reached, the current is the reversed and applied until a lower potential, $V_1$ is reached. The resulting potential is measured against time [83]. The potential is given as potential vs $Li/Li^+$, which also also applies for other potentials mentioned in this thesis, unless otherwise is stated. Figure 2.2 illustrates a voltage profile plot obtained by GC.

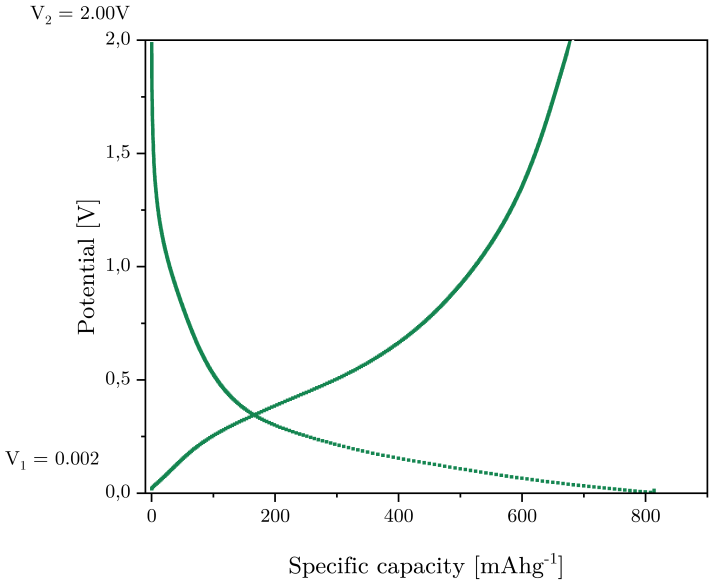


**Figure 2.2:** Illustration of a voltage profile/galvanostatic cycling curve with a higher cut-off potential of 2.00 V and a lower cut-off potential of 0.002 V

#### Differential capacity analysis

Differential capacity (DC) analysis employs the first derivative of the galvanostatic curve, dQ/dV. The differential capacity curve, illustrated in Figure 2.3, can be used to gain insight of the reactions happening in a cell during cycling. The peaks

visible in the curves can be associated to different phase transitions in the electrode material. Hence, the voltages at which electrochemical reactions occur during lithiation/delithitiation processes can be identified by observing peak positions on differential capacity plots. However, this technique can be limited by the occurrence of convoluted peaks, due to multiple reactions taking place at the same voltages, making the peaks difficult to distinguish [84].

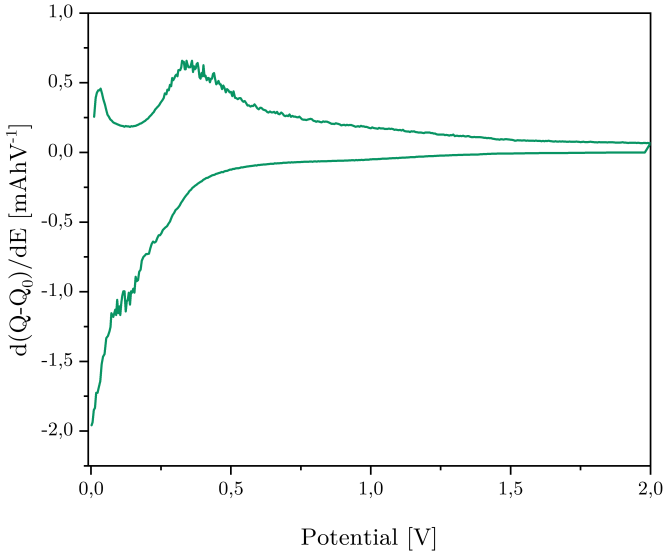


**Figure 2.3:** Differential capacity curve based on Figure 2.2.

### 2.9.2 Structural characterization techniques

#### Scanning electron microscopy

Scanning Electron Microscopy (SEM) is a powerful microscopy technique that employs an electron beam as an imaging medium, as opposed to employing light (photons), used in traditional microscopy methods [85]. The distinct advantage of SEM is its ability to render intricate, high-resolution images, which enables the detailed examination of surface morphology, structure, particle size, and compositional attributes of a material in the nano scale.

In a SEM, a highly focused electron beam systematically scans the sample surface, interacting with the sample's surface. The interactions between the sample and the electron beam produce distinguishable signals, which are then processed to generate an image. The principal signals gathered for image generation are secondary electrons (SE), backscattered electrons (BSE), and characteristic X-rays [85].

The generation of SE signals is a consequence of the ionization of atoms on the sample's surface by the incident primary electron beam. This ionization process induces the emission of loosely bound electrons from the surface atoms. With their relatively lower energy, in the range of 3-5 eV, these SEs are only capable of escaping from the surface of the sample, typically within a few nanometers into the material. This distinctive attribute makes the SE signals exceptionally useful for topographical investigations of the samples [85].

Conversely, BSE are electrons that have been scattered back towards the incident beam direction following their interaction with atoms in the sample. These BSEs possess considerably higher energy than SE, generally around 50 eV. Importantly, the intensity of the BSE signal tends to increase with the increase in atomic number of the sample. This correlation results in atomic number contrast, with different regions of varying atomic numbers within a sample exhibiting different intensities. This feature of BSE signals enables the exploration of the compositional variations within a sample [85]

### Energy dispersive X-ray spectroscopy

In SEM, the generation of characteristic X-rays serves as a crucial technique for elemental analysis within a sample. As the incident electron beam interacts with the sample, it causes ionization of inner-shell electrons. This ionization creates vacancies in the atomic energy levels, which are subsequently filled by electrons transitioning from higher orbitals. This downward transition is accompanied by the emission of photons within the X-ray range. As each element possesses a unique atomic structure, the emitted X-rays are distinctive and can be correlated with a specific element, thereby providing a unique "fingerprint" for each elemental component in the sample. This information is critical for gaining the elemental composition and their spatial distribution within the sample. The aforementioned process is central to the analytical technique known as Energy dispersive X-ray Spectroscopy (EDX or EDS) [86].

### Focused ion beam

Focused ion beam (FIB) is a powerful technique that can be used for material deposition and removal at the nano-scale, such as cross sections in samples for internal characterization. Most FIB systems today are incorporated with SEMs in

dual beam configurations, allowing for detailed characterization and manipulation at the same time. The FIB works by heating a reservoir of ions, usually gallium (Ga) ions, to near evaporation over a tip of tungsten. An electric field is then applied to the tungsten tip causing ions to accelerate down the column [87]. Due to the high energy of the ions, the interaction between the sample and ion beam may cause substantial change on the morphology. Therefore interpretation of surfaces modified by an ion beam should be interpreted with caution.

### X-ray powder diffraction

X-ray powder diffraction (XRD) is a powerful analytical technique that enables investigation of a material's crystallographic structure and composition. The underlying principle involves irradiating a sample with X-rays and subsequently observing the diffraction pattern. In essence, the X-rays interact with the atomic planes of the material and are scattered at an angle $\theta$. The relationship between the angle of diffraction and the interplanar spacing in the crystal lattice is given by Bragg's law [88]:

$$\sin\theta = \frac{n\lambda}{2d} \tag{2.25}$$

Given the angle of diffraction and the wavelength ($\lambda$) of the incident X-rays, the distance between atomic planes (interplanar spacing) can be determined. The ability to calculate the interplanar spacing enables the identification of distinct crystal structures. XRD measurements yield diffractograms, with the intensity of diffracted X-rays plotted as a function of the scattering angle, as illustrated in Figure 2.4. The positions of the peaks in the diffractogram are characteristic of specific atomic planes and crystal structures, thus facilitating the identification of diverse materials based on their unique crystallography. Investigating amorphous materials via XRD is inherently challenging due to the absence of long-range order, which results in less coherent diffraction patterns. Nonetheless, XRD can be effectively used to ascertain the amorphous nature of a material [88]. An example diffractogram of an amorphous material is depicted in Figure 2.4b.

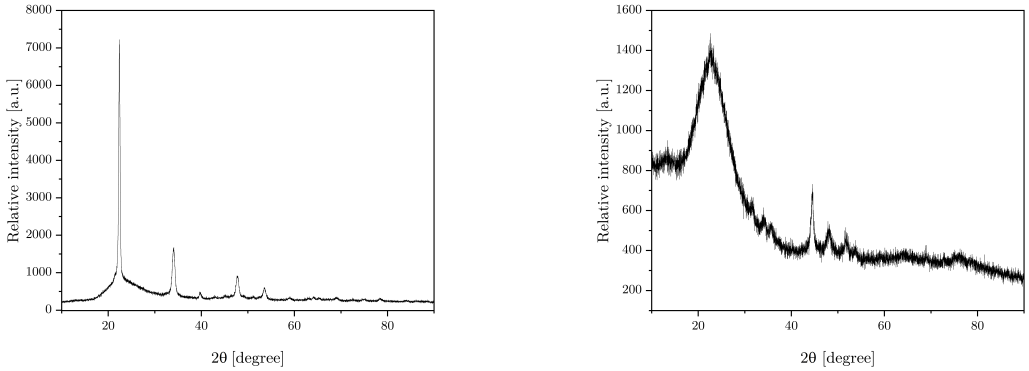


**(a)** Crystalline **(b)** Amorphous

**Figure 2.4:** XRD diffractograms

### In-Situ XRD using synchrotron radiation

In-situ XRD of LIBs employing synchrotron radiation has emerged as a potent method for studying real-time structural changes during battery operation. Synchrotron radiation offers several advantages over conventional X-ray sources, including high brilliance, tunable energy, and polarization, which are instrumental in obtaining high-resolution data. In-situ measurements provide a direct insight into the phase transformations, volume expansion, and other dynamic processes occurring in the battery electrodes during charging and discharging cycles. Moreover, the quick data acquisition times that synchrotron-based XRD allows are ideal for capturing fast, transient processes in battery materials [89].

To perform this technique, a specially designed cell has to be used, so to let the synchrotron x-rays pass through the cell. A multipurpose *operando* electrochemical cell has been developed by Drozhzhin *et al.* at the Swiss-Norwegian Beamlines (SNBL) at the European Synchrotron Radiation Facility (ESRF) in Grenoble, France [90]. An illustration of the cell is presented in Figure 2.5. The cell has a single crystal sapphire x-ray window, which provides great signal-to-noise ratio, good electrochemical contact, due to constant pressure between electrodes and electrochemical stability at higher potentials, due to the non-conductive and inert attributes of sapphire. As well as the specially designed cell, the electrodes under investigations benefit from some modification. To avoid strong reflections from the Cu current collector, this work uses a "free-standing" electrode, illustrated in Figure 2.6. The electrode is manufactured similarly to regular electrodes, but the Cu current collector which the electrode slurry is cast is perforated. This allows for x-rays to pass through

the electrode without the interference of Cu. When manufacturing such electrodes, the slurry has to be viscous enough, so to cover the holes without collapsing. It is also crucial that there is enough of the electrode material, so that the diffraction is strong enough.

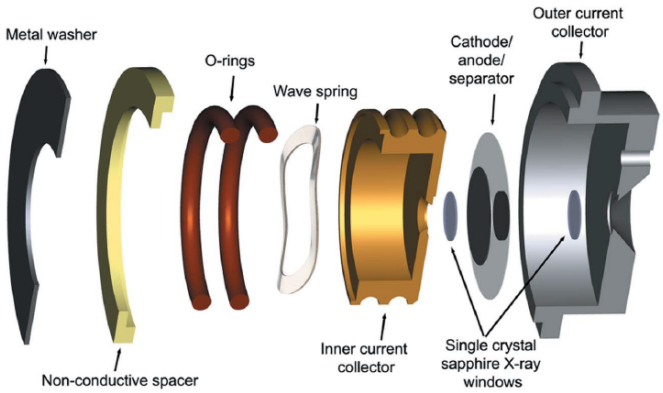


**Figure 2.5:** Schematic of the *operando* cell. Reused with permission from [90].

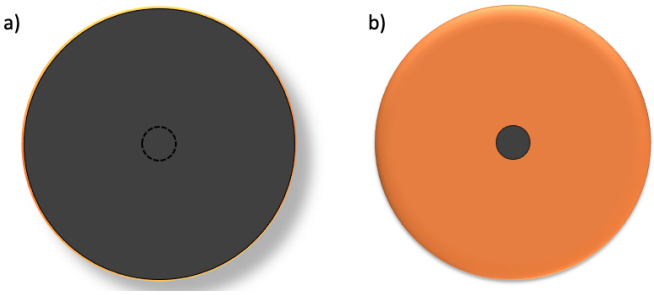


**Figure 2.6:** Electrode with free-standing electrode in the middle from a) top and b) bottom.

### Surface area and porosity analysis

To analyze the surface area and porosity of a material, BET analysis can be utilized. The principle behind this technique is to determine how many molecules of an inert gas that adsorbs to the surface and then calculate the surface area based on the area of the molecules adsorbed. A commonly used gas is $N_2$. This technique relies on that the gas molecules form a monolayer on the sample, but in reality most gases form a multiylayer. In the Brunauer-Emmet-Teller (BET) theory and t-plot theory this is accounted for and an estimation of surface area, pore distribution and pore type can be made. The BET surface area can be calculated when knowing the amount of inert gas adsorbed on the surface as a function of pressure. The t-plot theory is used to determine the distribution of micropores ($<2\,\mathrm{nm}$) in a structure relative

to the amount of mesopores (2-50 nm) and micropores (>50 nm). The meso- and macropores are often referred to as the external area [91].

## 2.10 Half-cell configuration for lab scale experiments

When working at laboratory scale it is more conventional and convenient to work with so-called half-cell configuration, rather than a full cell configuration.This configuration consists of either an anode or cathode and Li foil as a counter and reference electrode. There are several reasons why using a half-cell configuration is more beneficial for research purposes. Firstly, the ease of comparison with literature, due to the use of the same counter electrode and secondly, because Li foil provide almost limitless amount of $Li^+$ ions to the system. There are however some consequences that should be considered. When an anode is assembled into a half-cell with Li foil, the anode will act as a cathode, due to Li metals low standard reduction potential, which is the case for $SiO_x$ anodes described in this thesis. For ease and consistency of reading, materials considered anodes in full cell configuration will be referred to as anodes in this work. It is also necessary to redefine some of the parameters from Section 2.1.2 for half-cell configuration.

$$CE = 100 \cdot \frac{Q_{ch}}{Q_{dis}} \tag{2.26}$$

$$ICL = Q_{dis} - Q_{ch} \tag{2.27}$$

$$CCL = \sum_{k} Q_{dis} - Q_{ch} \tag{2.28}$$

# 3 Experimental

## 3.1 Diatom species

From the specialization project conducted by the author during the fall semester of 2022, it was found that the difference in morphology, porosity and nanostructure between diatom species do affect their performance when used as active material in anodes for LIBs [14]. Due to overall better electrochemical performance, Species A has been chosen as the $SiO_2$ source and precursor for this thesis work. SEM micrographs, displaying the morphology and size of the frustules, are presented in Figure 3.1 and the received diatom frustules can be viewed in Figure 3.2

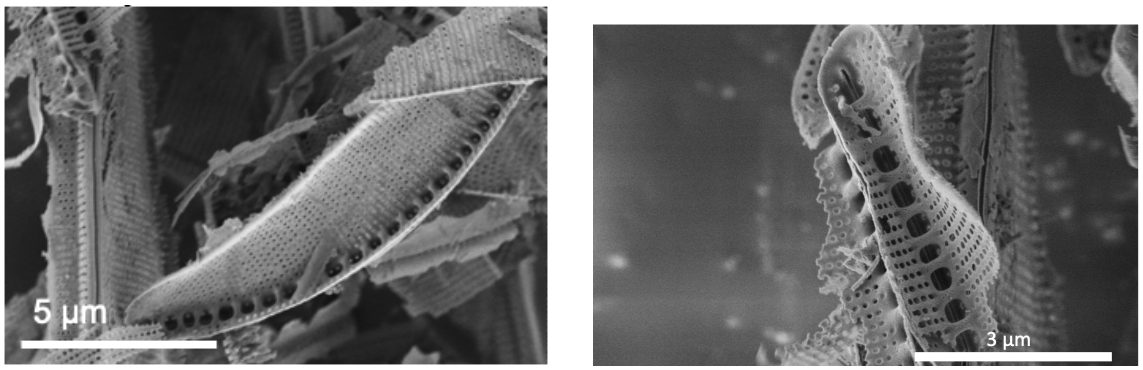


**(a)** Whole frustule. **(b)** Part of a frustule.

**Figure 3.1:** SEM micrographs of a frustule from diatom Species A.

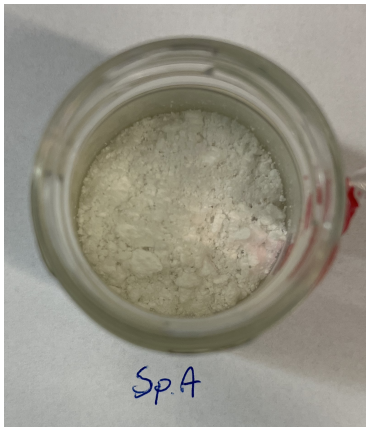


**Figure 3.2:** As recieved diatom frustule powder of Species A

## 3.2 Magnesiothermic reduction of $SiO_2$

Magnesiothermic reduction was conducted on the $SiO_2$ diatom frustules to obtain $SiO_x$. A schematic flowchart of the process is shown in Figure 3.3. Different molar ratios of $SiO_2$ frustules and Mg were weighted and mixed well using a mortar and pestle, the mixed powder was then transferred into an alumina crucible. The sample was then transferred into an Ar-filled glove box together with the stainless-steel (SS) reactor and graphite gasket. The sample is then transferred into the SS reactor and sealed tight using wrenches. Finally, the SS reactor is placed in the tubular furnace and annealed for 2 h in an argon atmosphere at a specified temperature with a ramping rate of 2°C/min. The reduction was conducted with different molar ratios and temperatures, given in Table 3.1. For one sample, NaCl was added to investigate the effect of using a heat scavenger, as described in Section 2.8. A second batch was made of the 1:1 molar ratio at 650°C to ensure enough material for anode manufacturing.

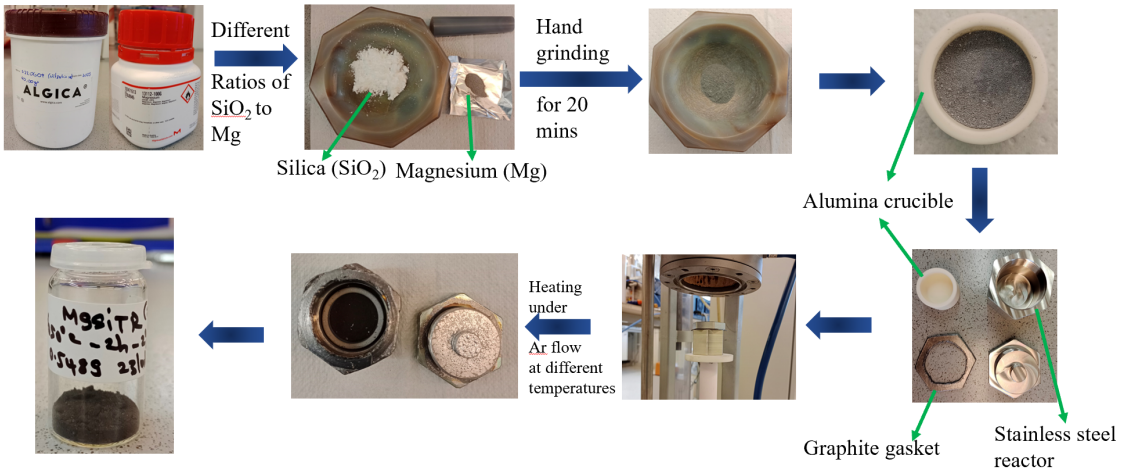


**Figure 3.3:** Schematic step by step of the magnesiothermic reduction process.

**Table 3.1:** Experimental conditions including sample identification, molar ratio of magnesium to silica, and temperature. The temperature ramp rate for all samples are 2°C/min

| Sample ID | Molar ratio [Mg:$SiO_2$] | Temperature [°C] |
|---|---|---|
| MS1 | 5.3:1 | 650 |
| MS2 | 2.5:1 | 650 |
| MS3 | 5.3:1 | 700 |
| MS4 | 5.3:1 | 750 |
| MS5 | 5.3:1 | 800 |
| MS6 | 1.2:1 | 650 |
| MS7 | 2.5:1 | 700 |
| MS8 | 2.5:1 | 750 |
| MS9 | 2.5:1 | 800 |
| MS10 | 2:1 | 650 |
| MS12 | 2:1 | 700 |
| MS15 | 1:1 | 650 |
| MS16 | 2.4:1:5.35 (:NaCl) | 650 |

#### Acid treatment of reduced samples

After reduction, the obtained powder was mixed well with 2 M HCl, the mixture was then stirred with a magnetic stirrer for 12 h to remove impurities such as MgO, $Mg_2Si$, etc. as described in Section 2.8. This was followed by a thorough washing with distilled water and ethanol. The samples were then dried at 60°C in an oven for 12 h to obtain $SiO_x$ for further characterization.

### 3.2.1 Characterization of $SiO_x$

#### X-ray diffraction

X-ray powder diffraction (XRD) (D8 A25 DaVinci, $CuK_\alpha$, Bruker) analysis of reduced samples was conducted to identify present phases in the $SiO_x$ samples, both before and after acid treatment. The scan was conducted using Bragg-brentano geometry between 10°-80°for 30 minutes. Rietveld refinement analysis was conducted on obtained diffractograms to quantify the amounts of present phases. The Rietveld analysis was performed by Pedro Alonso Sanchez in the framework of an

international collaboration with University of Zaragoza.

#### Scanning electron microscopy

A field emission SEM (Apreo, FEI) was used to investigate the morphology, nanostructure of the $SiO_x$ samples, both untreated and acid-treated and perform energy dispersive x-ray spectroscopy (EDS). The micrographs were obtained at a working distance between 1.5 mm and 10 mm, a acceleration voltage of 1 kV to 3 kV and a current between 6.3 pA and 13 pA using the T1 (BSE) and T2 (SE) detectors. The EDS was acquired using an Oxford X-Max 80 SDD EDX detector at a working distance of 10 mm and an acceleration voltage of 10 kV. Samples were put in isopropanol and sonicated for 10 minutes to break agglomerates during samples preparation. A few drops were then applied on top of carbon tape on top of the sample holder.

#### Surface area and porosity analysis

The surface area and pore structure of acid-treated $SiO_x$ samples were analyzed using $N_2$ gas adsorption at 77 K (3Flex, Micromeritics). Samples were degassed for at least 12 h at 250°C prior to measurements. Surface area and porosity was calculated by the instrument using Brunauer-Emmet-Teller (BET) and t-plot theory.

## 3.3 Anode manufacturing, cell assembly and characterisation

### 3.3.1 Slurry and binder preparation

#### Alginic binder

The alginate binder was prepared by the following protocol and was kept for not more than one week, before a new one had to be made.

1. Sodium alginate (Na-Alg, Sigma-Aldrich) was mixed in a beaker with a KCA buffer solution (pH = 3) at a mass ratio of 1:60 for coin cell anodes and 1:30 for In-situ cell anodes.

2. The beaker was then placed on a hot plate with a stirring magnet at 60°C at 500 RPM for 3 h.

### Electrode slurry for coin cells

Slurries for the electrodes were prepared by mixing different compositions of active material, alginic binder and conductive additives. First, the powders (active material and conductive additive) were weighed and mixed together with an oscillating mixer (MM400, Retsch) for 5 minutes at 25 Hz. The pre-prepared alginic binder (1:60 dilution) was then added and the slurry was mixed for 45 additional minutes at 25 Hz. The slurries were then put in a ultra sonic bath for 5 minutes to ensure no agglomerates before being cast.

Two different types of slurries were made. One with $SiO_x$ as the main active material, which had a composition of 50% active material, 35% carbon black (CB), and 15% binder. The other was a composite of $SiO_x$/graphite, which had a composition of 10% binder and 90% active material, where the active material was 70% graphite and 30% $SiO_x$.

The prepared electrode slurries were then cast onto the copper foil current collector (Plainstainproof, 18 µm, circuit foil) using a tape caster (K Control Coater 101, RK) and a wire wound rod to spread the slurry. After casting, the slurry was dried in an oven at 60°C for approximately 3 h. After drying 16 mm electrodes were punched out of the cast, weighed and stored before cell assembly. The mass loading of the cells can be found in Table A.1 in Appendix A.

### Electrode slurry for in-situ cell

The slurries for the in-situ electrodes were made by the same protocol as the $SiO_x$/graphite slurries in the aformentioned section, but with a 1:30 diluted alginic binder instead. The slurries were then casted onto a perforated Cu foil, with hole diameter being 1 mm, shown in Figure 3.4, using a cylindrical casting bar with a height of 200 µm, to ensure "free-standing" electrodes with sufficient thickness, as described in Section 2.9.2. The casts were then dried for approximately 3 h in an oven at 60°C. 12 mm electrodes were then punched out, weighed and stored before assembly.

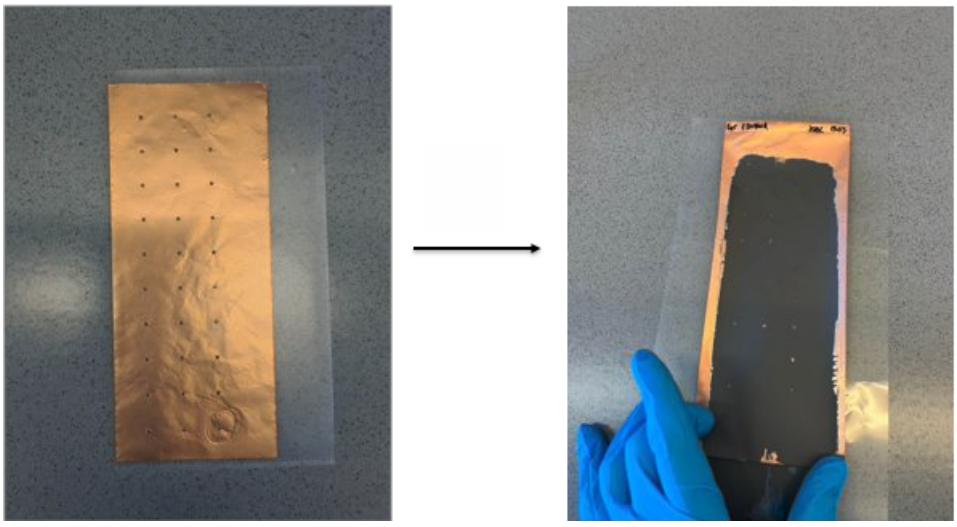

**Figure 3.4:** Perforated Cu foil and electrode cast on the foil.

### 3.3.2 Assembly of cells

#### Coin cells - CR2032

The electrodes were heated to 120°C in a vacuum oven overnight before being introduced into the Ar-filled glove box to ensure no humidity inside the electrodes. Coin cell parts were supplied by Hohsen and were of the 2032 type. A schematic of the different parts and order is shown in Figure 3.5. The coin cell base was fitted with a plastic gasket before the anode was placed inside with the Cu foil facing down and anode facing up. 25 µl of electrolyte ($LiPF_6$ EC:DEC 1:1, Sigma Aldrich) were applied on top of the electrode. Then a separator (Celgard 2400) was placed on the wet electrode and another 25 µl of electrolyte were added. A circular cutout of Li foil was pressed onto a stainless steel spacer and placed on top of the separator with the Li foil facing down. A spring was placed on top and the coin cell lid was put in place. The whole cell was pushed together and excess electrolyte was wiped of before using a crimper to seal the cell.

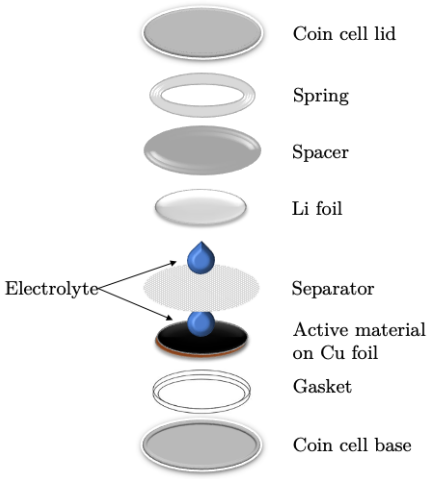


**Figure 3.5:** Schematic of the different parts and their order when assembling coin cells.

### 3.3.3 Anode characterization

#### Cross-section analysis

Cross-sections were made in pristine $SiO_x$ and $SiO_x$/graphite with a focused ion beam (FIB) (Helios NanoLab Dual-Beam FIB, FEI). The cross-sections were made by a gallium ion source. First, a square was cut with a high beam current of 21 nA, then a lower current of 2.7 nA was used to "polish" the surface, to more clearly see the morphology.

#### Galvanostatic cycling

Galvanostatic cycling was conducted on cells made with $SiO_x$ anodes and $SiO_x$/graphite using a BioLogic potentiostat. Based on previous results obtained in the research group [11], [12], a sequence of 5 activation cycles is required for $SiO_2$ sourced from diatoms to fully react. The "activation cycles" consists of galvanostatic cycling at 50 $mAg^{-1}$ between 2 mV and 2 V, followed by potentiostatic holding steps after each half cycle for 48 h and 24 h, respectively. However, it was found in the specialization project done by the author, that for some diatom frustules, this procedure is not necessary [14]. Therefore, in this work, cells were activated for the first cycle at 50 $mAg^{-1}$ and were then continued cycling at 100 $mAg^{-1}$. To further investigate the necessity of an activation cycle, cells were also cycled directly at 100 $mAg^{-1}$ without an activation at lower currents.

The electrochemical data gathered was then processed and differential capacity analysis was conducted using the EC-lab Demo software provided by BioLogic.

## 3.4 In situ XRD analysis

In-situ X-ray diffraction measurements were carried out at the European synchrotron radiation facility (ESRF) in Grenoble, France using the BM-01 at the Swiss-Norwegian beamline (SN-BL).

### 3.4.1 Assembly of in-situ cells

The design of the in-situ cell used is based on a design by Drozhzhin et al. as described in Section 2.9.2 [90]. The cells were assembled in an Ar-filled glove box at ESRF. The procedure was similar to the coin cells described in Section 3.3.2. First, the anode was carefully placed on top of the inner current collector, making sure that the "free-standing" electrode was aligned with the sapphire window. 25 µl of electrolyte ($LiPF_6$ EC:DC 1:1, Sigma Aldrich) was then applied on top of the electrode. A separator (Celgard 2400) was placed on the wet electrode followed by another 25 µl of electrolyte. A circular cutout of Li foil was then pressed in place and the outer current collector was carefully placed on top. The whole cell was pushed together to seal it tight. Final inspection to make sure the "free-standing" electrode was visible through the sapphire window was conducted. The screw, used to connect the outer current collector to the potentiostat, was screwed in carefully, so not to go to far inside the cell, to avoid causing a short circuit.

### 3.4.2 Experimental setup

The experimental setup for the in-situ XRD can be viewed in Figure 3.6. The assembled cells were mounted in the holder, which was placed in transmission mode, and then connected to a BioLogic potentiostat. The holder was then placed at a fixed distance, of about 30 cm, between the incoming X-ray beam and 2D-detector (Pilatus 2M).

The cells were cycled at a C-rate of C/10 for two cycles, where the capacity of the cell was calculated based on 30% Si and 70% graphite, and the capacities of Si and graphite being 4200 $mAhg^{-1}$ and 372 $mAhg^{-1}$, respectively.

Time-resolved in situ synchrotron X-ray diffraction measurements were performed during lithiation and delithiation of the electrode. The voltage window was 2 V-2 mV. Data collection time was 10 seconds, and the time resolution was approximately 3.6 minutes, which was suitable to track structural changes on the $SiO_x$/graphite composite anode upon electrochemical cycling. Data was acquired using Pilatus Dectris CdTe detector, at a wavelength of 0.7100 Å, and with a beam size of 0.3 mm x 0.3 mm (V X H).

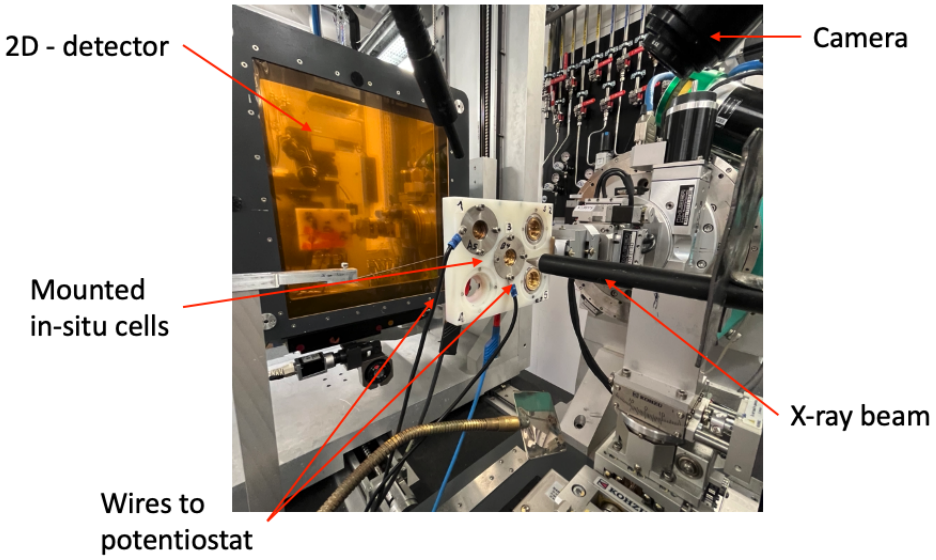


**Figure 3.6:** Setup for in-situ XRD.

### 3.4.3 Data processing

Data processing was conducted using Dioptas, a python based program for data processing of 2-dimensional diffraction data [92]. First, the software was calibrated against a standard calibration material ($LaB_6$ in this thesis). An image of the calibration material was loaded in the software, Figure 3.7a, and the reflections (rings) were marked as best as possible. Experimental values for energy, wavelength, approximate distance to detector were then entered and calibration could proceed. If the calibration was sufficient, peaks would clearly be visible in the image (cake), shown in Figure 3.7b, a diffraction pattern with intensity against 2θ could be viewed, shown in Figure 3.7c. If the calibration was not sufficient, the image and diffraction pattern would be distorted. After calibration, an obtained diffraction image was uploaded and the beamstop, lines and detector gaps were masked, shown in Figure 3.7d, so to not interfere with the diffraction pattern. This was then done to all obtained diffraction images to obtain diffractograms for analysis, shown in Figure

3.8.

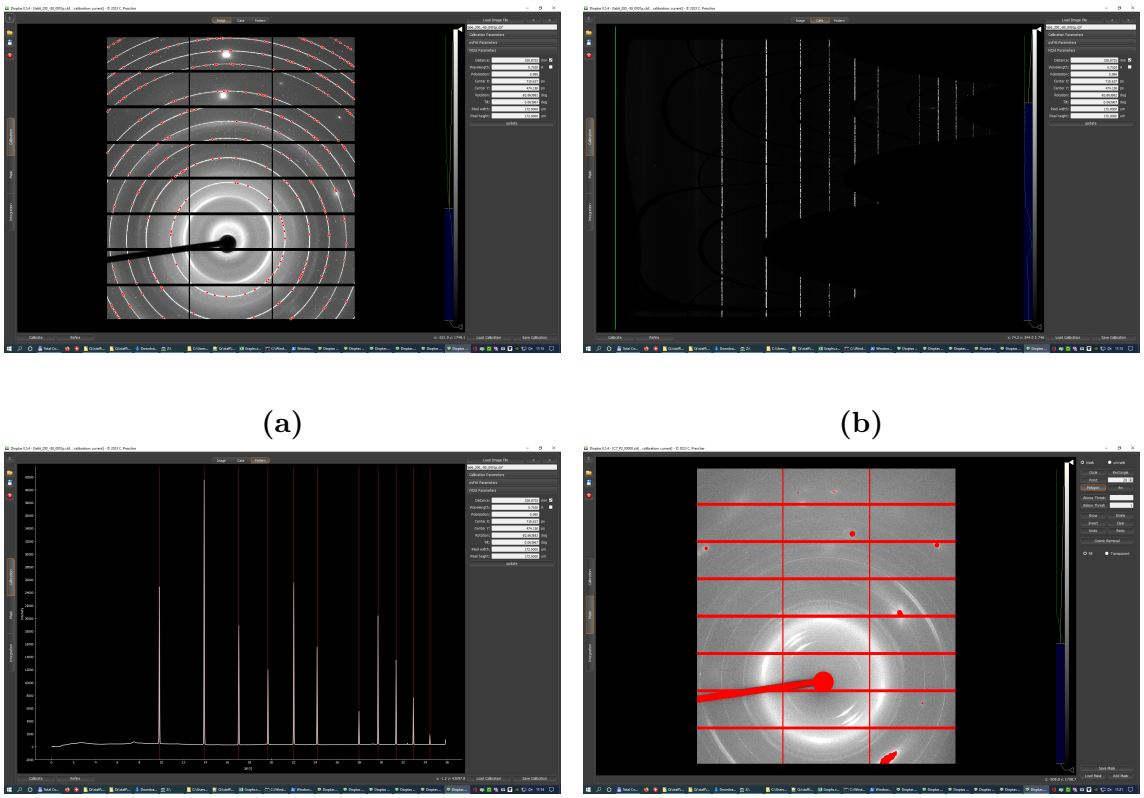

(a) (b)

(c) (d)

**Figure 3.7:** Steps in data processing.

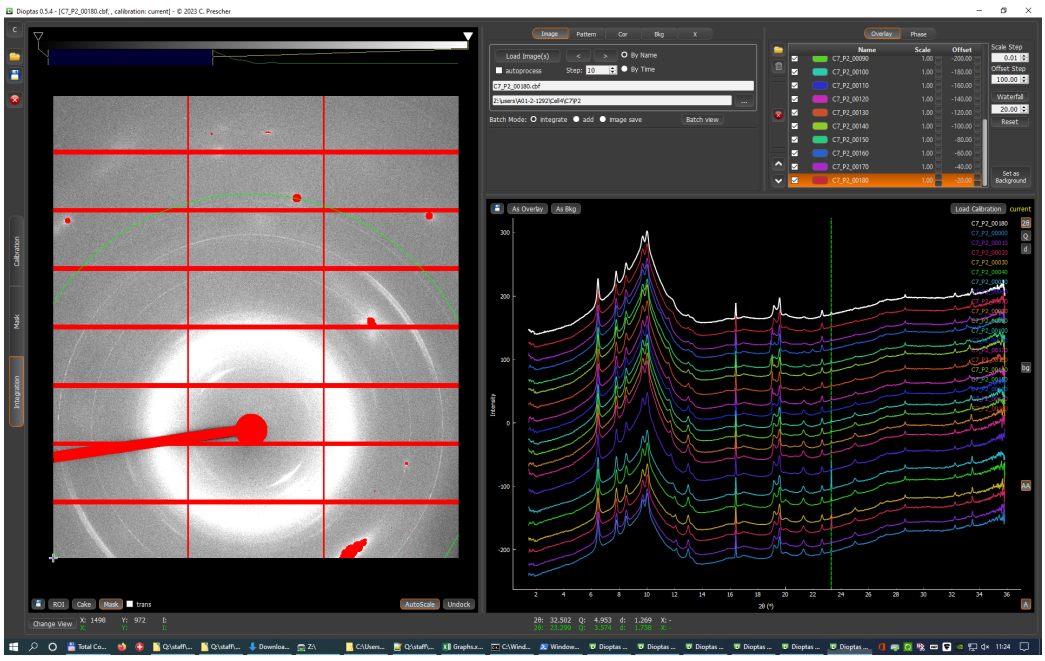

**Figure 3.8:** Several diffractograms obtained from data processing.

# 4 Results

## 4.1 Overview

The results are divided in three main parts. First, the magnesiothermic reduction of $SiO_2$ and the characterization of obtained $SiO_x$. Then the electrochemical characterization of $SiO_x$ and $SiO_x$/graphite anodes. Finally, the results from the in-situ XRD on $SiO_x$/graphite anodes. Results from $SiO_x$ structural and electrochemical characterization are compared with previous data obtained with $SiO_2$ frustules, which were studied in the framework of the specialization project [14]. Based on the XRD results that will be presented, sample MS15 (synthesized at 650°C with 1:1 molar ratio) was chosen for further experiments and will be referred to as $SiO_x$ in subsequent results. All molar ratios referred to are Mg:$SiO_2$ unless otherwise is stated.

## 4.2 Magnesiothermic reduction

### 4.2.1 XRD

The XRD diffractogram of pristine $SiO_2$ frustules is presented in Figure 4.1, to compare the effects of the MgTR. The pristine frustules presents as amorphous, as seen from the broad peaks situated around 20°-30° and 40°-50°.

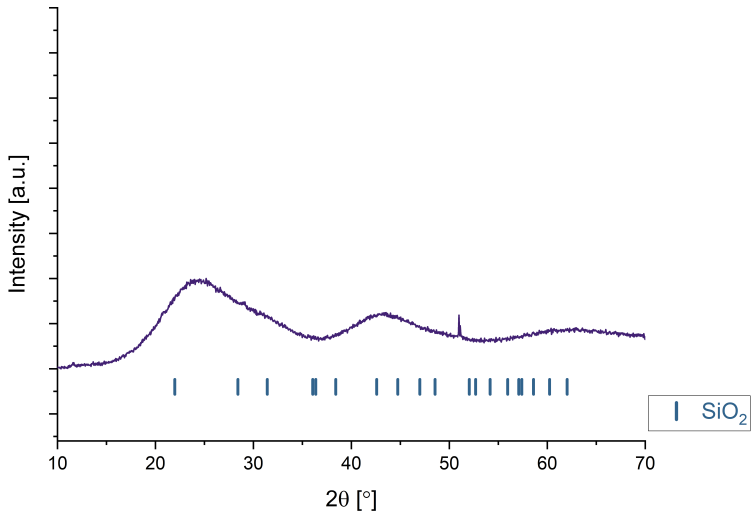


**Figure 4.1:** Diffractogram obtained of pristin $SiO_2$ frustules.

The results from X-ray powder diffraction on samples obtained after the MgTR, and before acid treatment is given in Figure 4.2 and Figure 4.3a and quantitative results from Rietveld refinement is presented in Table 4.1. All diffractograms depict the presence of Si, Mg, MgO, $Mg_2Si$ phases. As the temperature is increased, an increase in the amount of $Mg_2Si$ for higher molar ratios is observed, lowering the observed amount of Si. As the molar ratio is decreased an increase in MgO is observed together with an increase in Si. The presence of unreacted Mg can be observed for a molar ratio of 5.3:1. For sample MS15 (molar ratio 1:1, 650°C), the presence of unreacted $SiO_2$ is observed through the broad reflection at 22° and the presence of Si can be identified at the reflection at 28°, confirming the presence of $SiO_x$. Based on these results, MS10 (molar ratio 2:1, 650°C), MS15 (molar ratio 1:1, 650°C) and MS16 (molar ratio 2.4:1(:5.35 NaCl), 650°C) were chosen for acid treatment. The XRD diffractograms of acid treated samples are presented in Figure 4.3b and quantitative results from Rietveld refinement are presented in Table 4.2. From the diffractograms and table, it is confirmed that acidic treatment has been successful in the removal of Mg, MgO and $Mg_2Si$ during post reduction treatment.

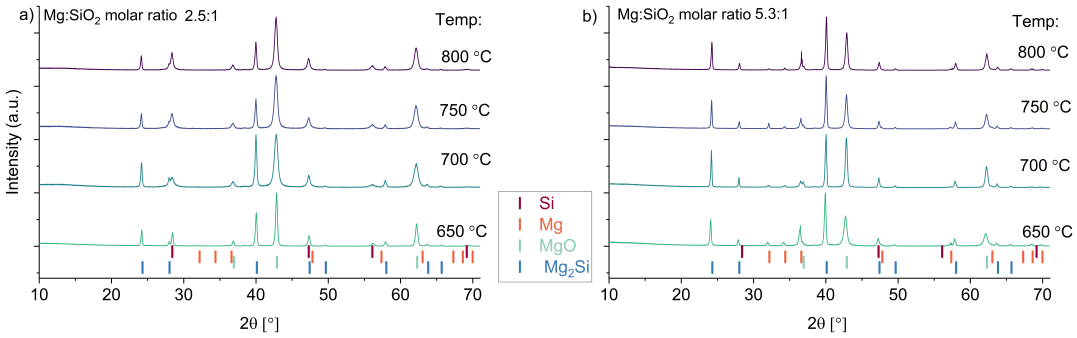


**Figure 4.2:** XRD diffractograms of $SiO_x$ samples at the different reduction temperatures at a constant molar ratio of a) 2.5:1 and b) 5.3:1

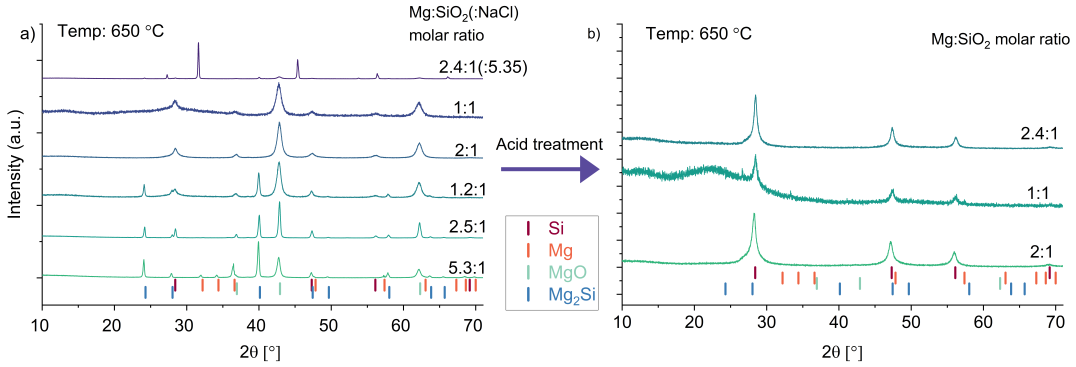


**Figure 4.3:** XRD diffractograms of $SiO_x$ samples at different molar ratios and a constant reduction temperature of 650°C, where a) depicts samples before acid treatment and b) acid treated samples.

**Table 4.1:** Phases and amount present in the samples after MgTR, based on Rietveld refinement. N.O. denotes that the phase was not observed in the Rietveld refinement.

| Sample ID | Si (%) | Mg (%) | MgO (%) | $Mg_2SiO_4$ (%) | $Mg_2Si$ (%) | $SiO_2$ (%) | NaCl (%) | Molar ratio [Mg:$SiO_2$] | Temp. [°C] |
|---|---|---|---|---|---|---|---|---|---|
| MS1 | 0 | 10.45 | 52.44 | 0 | 37.11 | N.O. | - | 5.3:1 | 650 |
| MS2 | 9.22 | 0.2 | 62.46 | 0 | 28.13 | N.O. | - | 2.5:1 | 650 |
| MS3 | 0.04 | 4.9 | 57.57 | 0 | 37.48 | N.O. | - | 5.3:1 | 700 |
| MS4 | 0.04 | 8.26 | 52.09 | 0 | 39.6 | N.O. | - | 5.3:1 | 750 |
| MS5 | 0.04 | 4.8 | 53.6 | 0 | 41.56 | N.O. | - | 5.3:1 | 800 |
| MS6 | 17.06 | 0 | 67.99 | 0 | 14.94 | N.O. | - | 1.2:1 | 650 |
| MS7 | 9.86 | 0 | 65.61 | 0 | 24.54 | N.O. | - | 2.5:1 | 700 |
| MS8 | 14.55 | 0 | 70.06 | 0 | 15.39 | N.O. | - | 2.5:1 | 750 |
| MS9 | 14.76 | 0 | 68.78 | 0 | 16.46 | N.O. | - | 2.5:1 | 800 |
| MS10 | 20.59 | 0 | 79.1 | 0 | 0 | N.O. | - | 2:1 | 650 |
| MS12 | 18.24 | 0 | 70.24 | 2.98 | 8.54 | N.O. | - | 2:1 | 700 |
| MS15 | 17.62 | 0 | 64.2 | 0 | 0 | 18.18 | - | 1:1 | 650 |
| MS16 | 5.44 | 0 | 23.78 | 0 | 23.78 | N.O. | 65.76 | 2.4:1:5.35 (:NaCl) | 650 |

**Table 4.2:** Phases and amount present in the samples after MgTR and acid treatment, based on Rietveld refinement.

| Sample ID | Si (%) | Mg (%) | MgO (%) | $Mg_2SiO_4$ (%) | $Mg_2Si$ (%) | $SiO_2$ (%) | NaCl (%) | Molar ratio [Mg:$SiO_2$] | Temp. [°C] |
|---|---|---|---|---|---|---|---|---|---|
| MS10-AT | 99.9 | 0 | 0.01 | 0 | 0 | N.O. | - | 2:1 | 650 |
| MS15-AT | 15.07 | 0 | 0 | 0 | 0 | 84.93 | - | 1:1 | 650 |
| MS16-AT | 73.99 | 0 | 0 | 0 | 0 | 26.0 | 0 | 2.4:1:5.35 (:NaCl) | 650 |

The diffractograms of $SiO_x$ before and after acid treatment compared with $SiO_2$ from pristine frustules is presented Figure 4.4. The diffractograms show that after reduction, the $SiO_x$ have gained some crystalline phases, opposed to the pristine $SiO_2$ frustules which presents as almost fully amorphous.

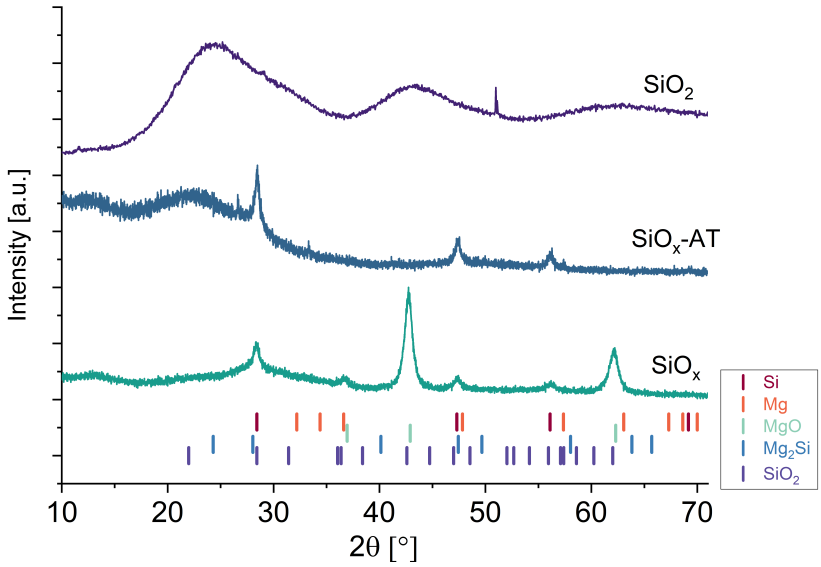


**Figure 4.4:** Diffractograms of pristine $SiO_2$ and $SiO_x$ before and after acid treatment, where AT denotes the acid treated sample.

### 4.2.2 Surface area

The specific surface area results from BET measurements on acid treated $SiO_x$ are presented together with results of pristine $SiO_x$ in Figure 4.5 and summarized in Table 4.3. The $SiO_x$ presents with a drastic increase in BET surface area, at $\approx 5.4$ times larger compared to pristine $SiO_2$ frustules. Interestingly, this increase is

almost entirely attributed to the change in external surface area, as the micropore area increased by only 2.3 $m^2g^{-1}$.

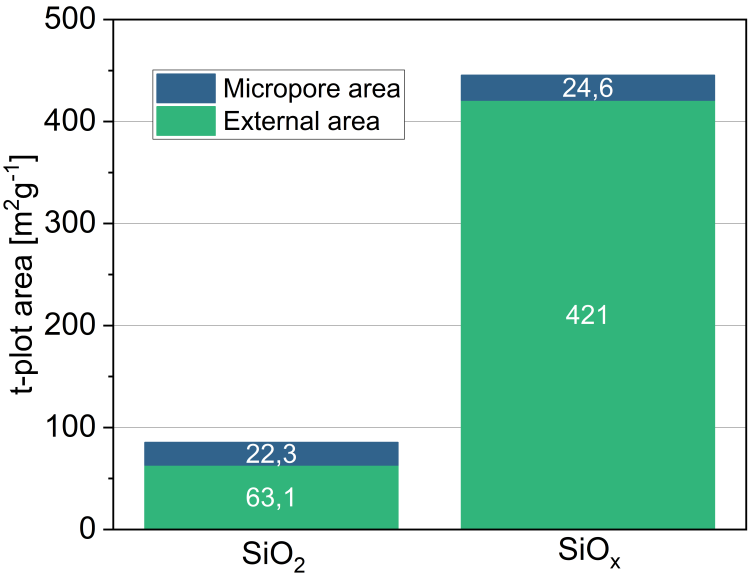


**Figure 4.5:** Barplot showing the BET surface area and t-plot external and micropore area of pristine $SiO_2$ frustules and acid treated $SiO_x$.

**Table 4.3:** BET surface area, t-plot external area and t-plot micropore area for pristine $SiO_2$ frustules and acid treated $SiO_x$.

| Sample | BET surface area [$m^2g^{-1}$] | t-plot external area [$m^2g^{-1}$] | t-plot micropore area [$m^2g^{-1}$] |
|---|---|---|---|
| $SiO_2$ | 85.4 | 63.1 | 22.3 |
| $SiO_x$ | 465.6 | 421.0 | 24.6 |

Isotherms of $SiO_x$ and pristine $SiO_2$ frustules obtained from BET analysis are presented in Figure 4.6. Both samples present with a type II physisorption isotherm [91]. This indicates that both samples presents as mostly macroporous.

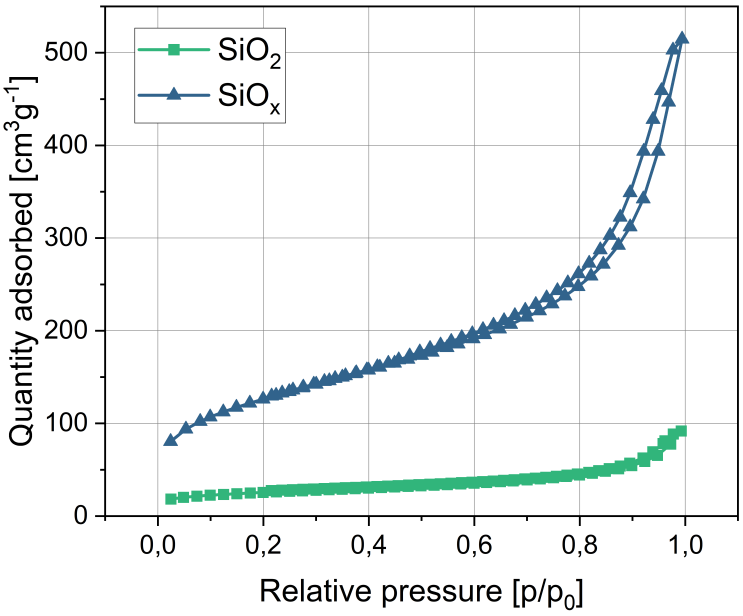


**Figure 4.6:** Isotherms of pristine $SiO_2$ frustules and $SiO_x$, obtained by BET analysis.

The pore volume and differential pore volume as a function of pore width for pristine $SiO_2$ frustules and $SiO_x$ are presented in Figure 4.7.

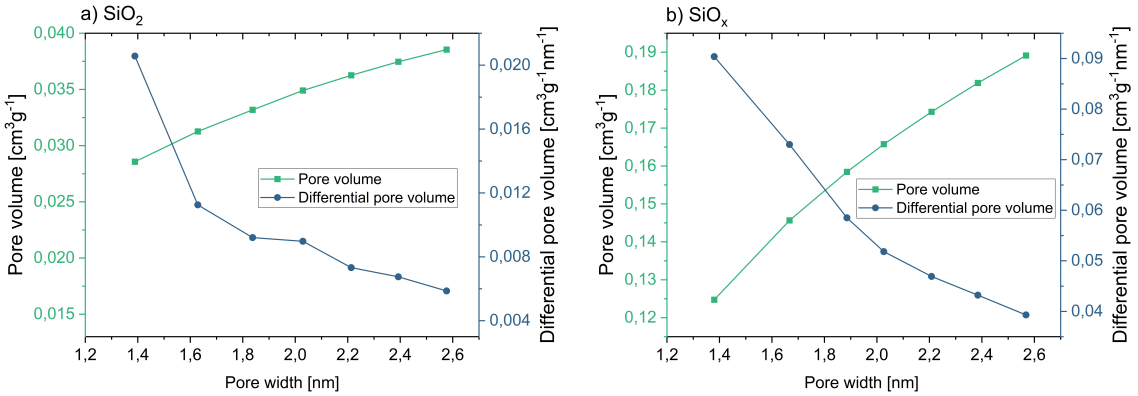


**Figure 4.7:** Pore volume and differential pore volume as a function of pore width for a) pristine $SiO_2$ frustules and b) $SiO_x$

### 4.2.3 SEM & EDS

Micrographs of pristine $SiO_2$ is presented in Figure 4.8, frustules post MgTR in Figure 4.9 and frustules post MgTR and acid treatment in Figure 4.10. The micrographs of pristine frustule, shows the intricate micro structure, with pores in

different size ranges. After the MgTR the micro structure is observed to be preserved, and is showing additional porosity not present in pristine frustules. This is especially visible in Figure 4.9a, where the surface presents a substantial amount of pores. The surface, post reduction, presents as rougher compared to pristine frustules, which is visible especially on the edges of the larger pores. The micro structure after the acidic treatment is still preserved, and on a surface level does not seem to be negatively effected by the acid treatment. The micrographs presented display parts of the frustules found during SEM, but bigger agglomerated particles were also found. Additional micrographs displaying agglomerates can be found in Appendix B.

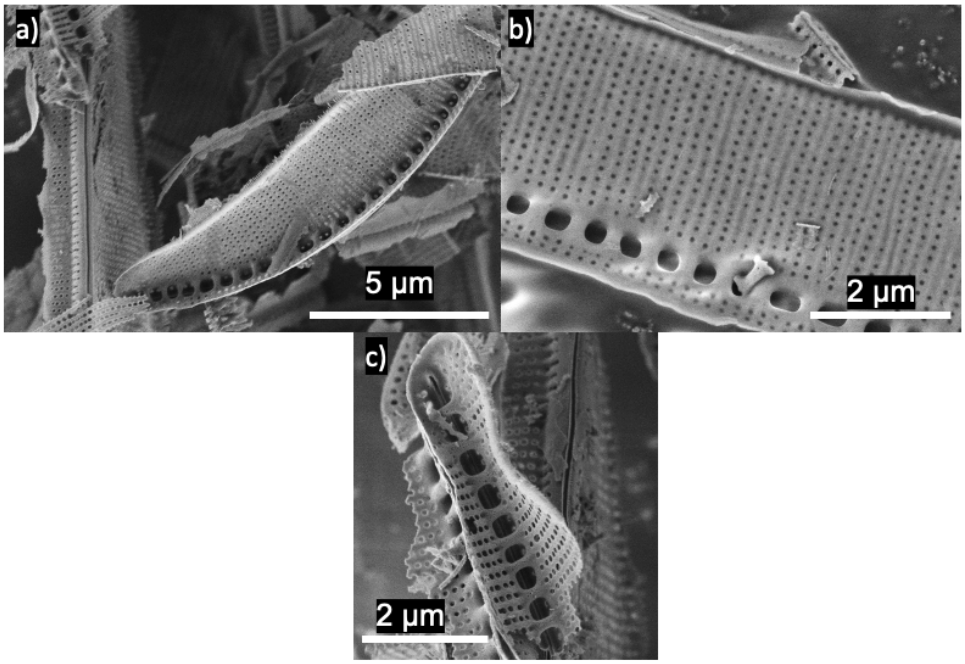


**Figure 4.8:** SEM micrograpahs of pristine $SiO_2$ frustules.

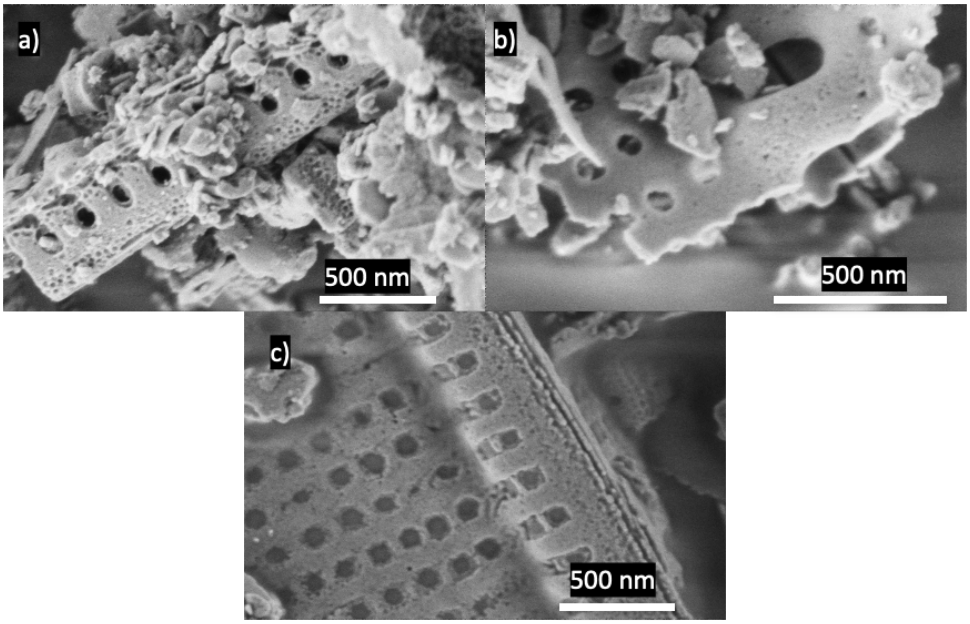


**Figure 4.9:** SEM micrographs of diatom frustules post MgTR.

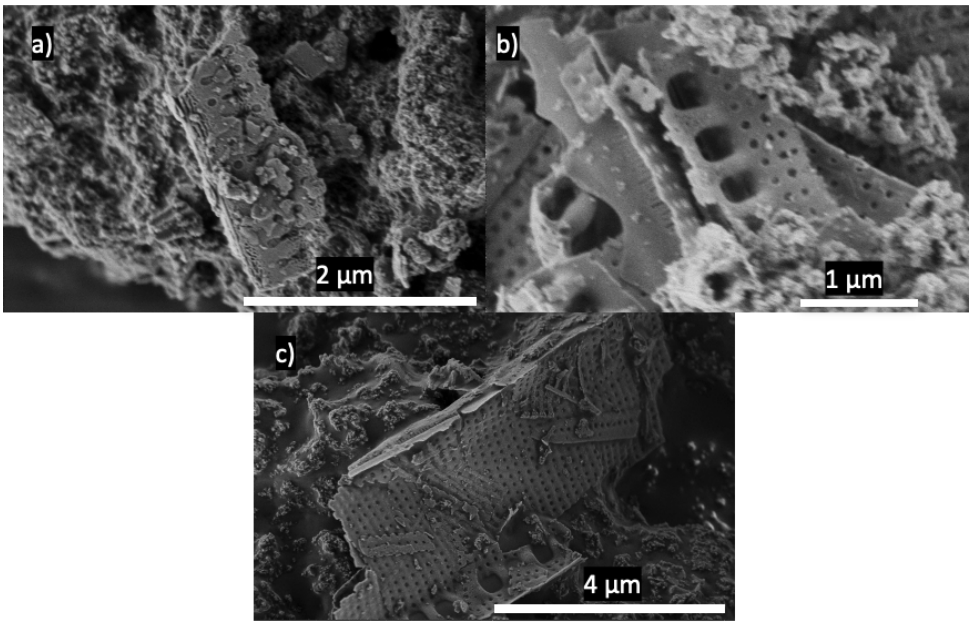


**Figure 4.10:** SEM micrographs of diatom frustules post MgTR and acid treatment.

EDS maps and corresponding SEM micrograph of post MgTR $SiO_x$ particles is presented in Figure 4.11 and of post MgTR and acid treatment $SiO_x$ particles in Figure 4.12. The presence of Si and O is clearly visible in both figures, and Mg is present before the acidic treatment, but reduced to just trace amounts after acid treatment. Together with XRD results, this confirms the effectiveness of acid treatment to remove unwanted phases. C is also present, but the signals are attributed to the carbon tape used in sample preparation. Trace amounts of Na, Ni, Co, S, Fe

and Mn is also visible. As mentioned, a second batch of $SiO_x$ with 1:1 molar ratio at 650°C were made and EDS maps with corresponding SEM micrographs can be found in Appendix C. Map sum spectra corresponding to the presented EDS maps are also given in Appendix C

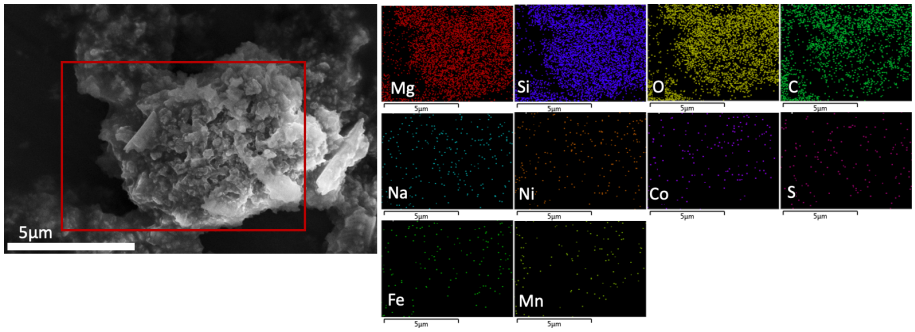


**Figure 4.11:** SEM micrograph and EDS maps of $SiO_x$ particles post MgTR. EDS maps acquired from area marked with red.

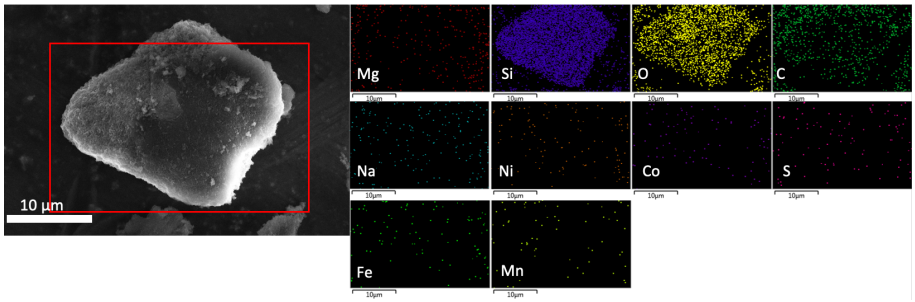


**Figure 4.12:** SEM micrograph and EDS maps of $SiO_x$ particles post MgTR and acid treatment. EDS maps acquired from area marked with red.

## 4.3 Anode & Electrochemical characterization

SEM micrographs of FIB cuts on uncycled anodes with $SiO_x$ as active material and $SiO_x$/graphite as acitve material is presented in Figure 4.13 and Figure 4.14, respectively. There is a clear different in the morphology between the two anodes. The $SiO_x$/graphite anode presents as more porous than the pure $SiO_x$ anode.

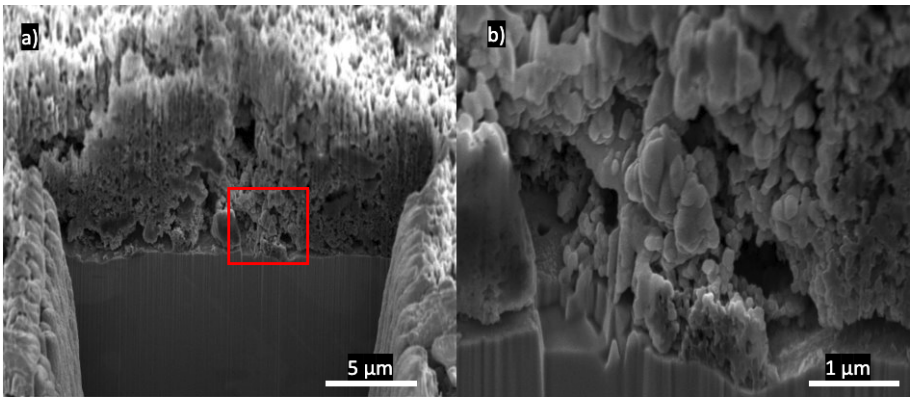


**Figure 4.13:** SEM micrographs of FIB cut conducted on uncycled $SiO_x$ anode. b) shows a higher magnification of the red square in a).

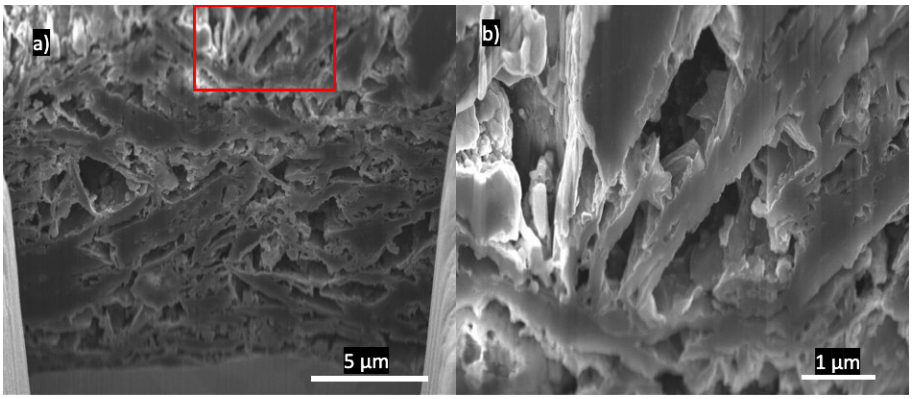


**Figure 4.14:** SEM micrographs of FIB cut conducted on uncycled $SiO_x$/graphite anode. b) shows a higher magnification of the red square in a)

### 4.3.1 $SiO_x$-based anodes

The voltage profile of the $SiO_x$-based cell with an activation cycle is presented in Figure 4.15 and the corresponding DC curve is shown in Figure 4.16. The cell presents with an initial discharge and charge capacity of 2352.0 $mAhg^{-1}$ and 1277.0 $mAhg^{-1}$, respectively, leading to an initial CE of only 54,3% for the activation cycle. In the subsequent cycle the discharge and charge capacities are 1089,8 $mAhg^{-1}$ and 947,4 $mAhg^{-1}$, leading to a higher CE of 86,9 %. From Figure 4.15b, it is evident that the capacity continues to decrease as cycling goes on.

In the DC curve of the activation cycle, in Figure 4.16a there are cathodic peaks observed at 0.7 V, 0.2 V and around 0.1 V, and anodic peaks are observed at 0.44 V, 0.3 V and 0.03 V. In the second, cycle the sharp peaks observed during activation, is now almost entirely gone, the peaks have broadened, but a small sharp cathodic peak observed at 0.44 V reappears in subsequent cycles, in Figure 4.16b.

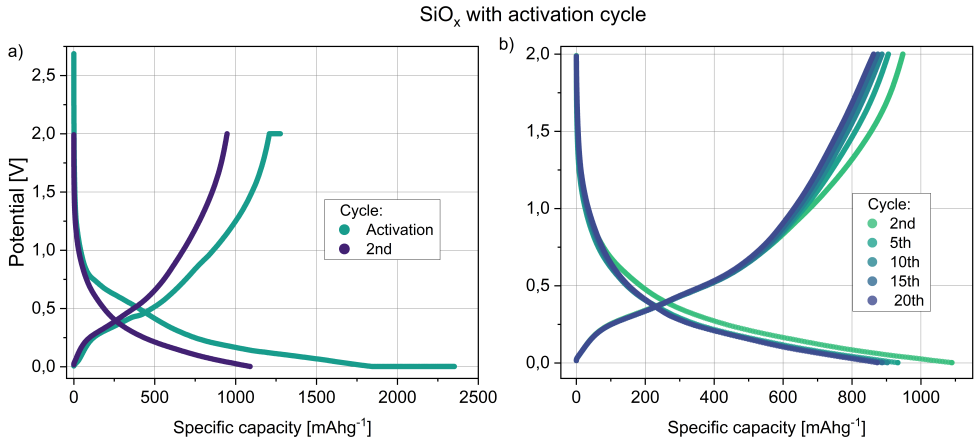


**Figure 4.15:** Voltage profile of $SiO_x$-based cell showing a) activation cycle at 50 $mAg_{-1}$ and 2nd cycle at 100 $mAg^{-1}$, and b) subsequent cycles at 100 $mAg^{-1}$

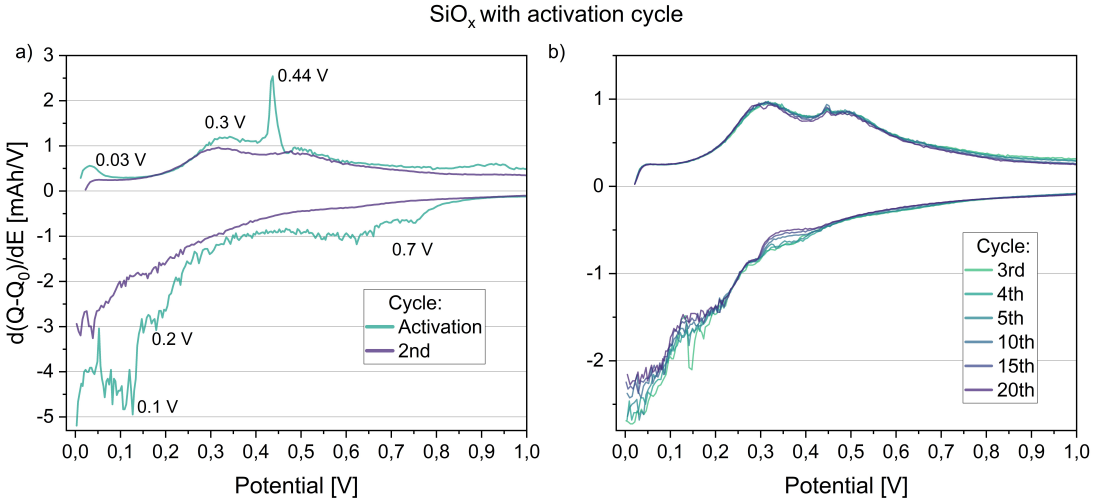


**Figure 4.16:** DC curve of $SiO_x$-based cell showing a) activation cycle at 50 $mAg_{-1}$ and 2nd cycle at 100 $mAg^{-1}$, and b) subsequent cycles at 100 $mAg^{-1}$

The voltage profile of the $SiO_x$-based cell without an activation cycle is presented in Figure 4.17 and the corresponding DC curve is shown in Figure 4.18. The initial discharge and charge capacities are 2002.0 $mAhg^{-1}$ and 1027.4 $mAgh^{-1}$ respectively, giving an initial CE of 51.3%. Which is slightly lower than the $SiO_x$ cell with an activation cycle. The subsequent cycle has a discharge and charge capacity of 1111.6 $mAhg^{-1}$ and 991.8 $mAhg^{-1}$, giving a CE of 89.2%. From Figure 4.17b, as cycling goes on, the capacity decrease is not as prominent as the cell with an activation cycle.

The DC curve of the activation cycles, in Figure 4.18a), shows cathodic peaks 0.7 V, 0.2 V and around 0.1 V. Anodic peaks are observed at 0.44 V, 0.3 V and 0.029 V.

In the second cycle, cathodic peaks are no longer prominent, but the anodic peaks appear at the same positions as for the first cycle. In the subsequent cycles, in Figure 4.18b, the cathodic peaks remain less prominent, but the anodic peaks seem to increase in intensity.

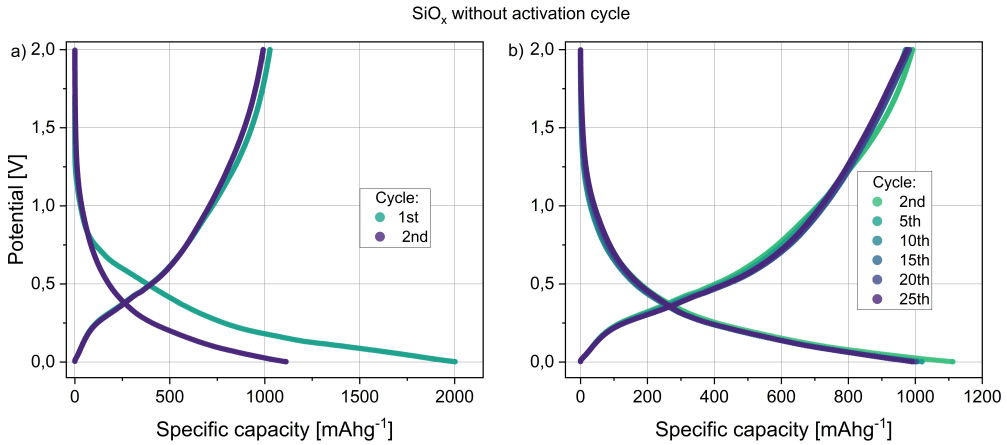


**Figure 4.17:** Voltage profile of $SiO_x$-based cell without activation cycle, showing a) 1st and 2nd cycle at 100 $mAg^{-1}$, and b) subsequent cycles at 100 $mAg^{-1}$

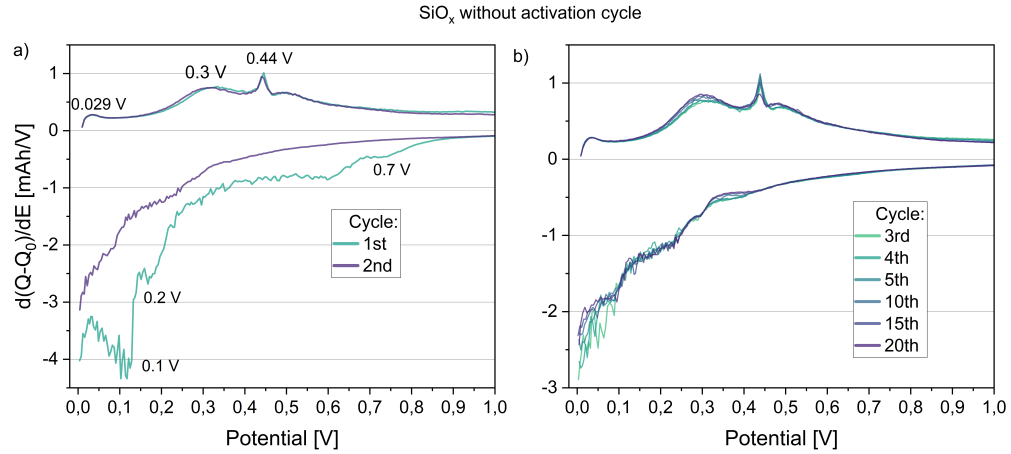


**Figure 4.18:** DC curve of $SiO_x$-based cell without activation cycles, showing a) 1st and 2nd cycle at 100 $mAg^{-1}$, and b) subsequent cycles at 100 $mAg^{-1}$

To gain insight into how $SiO_x$-based anodes differ from $SiO_2$-based anodes, electrochemical data obtained using $SiO_2$ frustules as active material from specialization project conducted by the author is included. The $SiO_2$ anode was made following the same procedure as the $SiO_x$ anodes described in Section 3.3, and with the same type of diatom frustules. The cycling of the $SiO_2$-based cell was conducted with an activation cycle. The voltage profile is presented in Figure 4.19 and the corresponding DC curve is presented in Figure 4.20. The cell presents with an initial

discharge and charge capacity of 2361.1 $mAhg^{-1}$ and 834.5 $mAhg^{-1}$, giving a low initial CE of 34.3%. The subsequent cycle showed an discharge and charge capacity of 682.2 $mAhg^{-1}$ and 569.1 $mAhg^{-1}$ respectively, giving a CE of 83.4%. The cycling behavior is observed to differ from that of the $SiO_x$-based anodes, as the capacity increases with cycling, in Figure 4.19b.

In the DC curve of the activation cycle anodic peaks are observed at 0.3 V and 0.03 V and cathodic peaks at 1.48 V and 0.8 V. During the second cycle the neither anodic or cathodic peaks are prevalent, but a cathodic peak has appeared at 0.15 V. In the subsequent cycles, in Figure 4.20b anodic peaks at 0.5 V, 0.35 V and 0.03 V and increases as the cell cycles. The cathodic peak observed at 0.15 V becomes more prevalent and another peak emerges at 0.35 V between the $20^{th}$ and $30^{th}$ cycle, and seems to shift towards higher potentials as cycling continues.

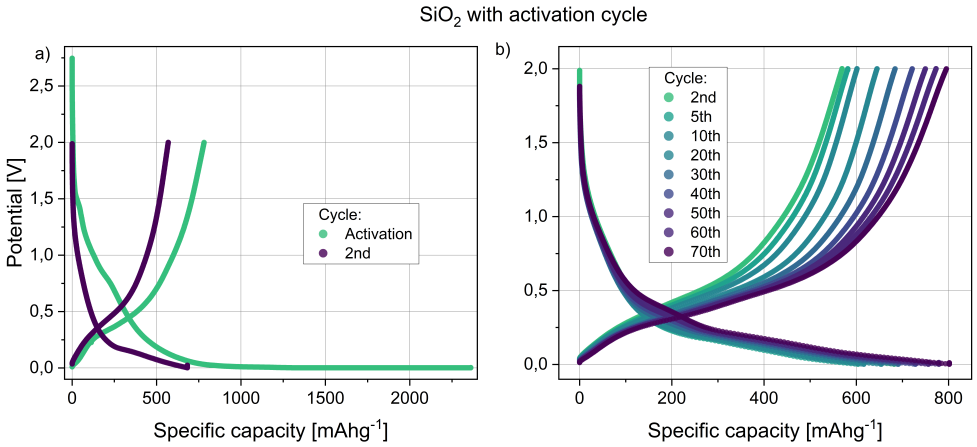


**Figure 4.19:** Voltage profile of $SiO_2$-based cell showing a) activation cycle at 50 $mAg_{-1}$ and 2nd cycle at 100 $mAg^{-1}$, and b) subsequent cycles at 100 $mAg^{-1}$

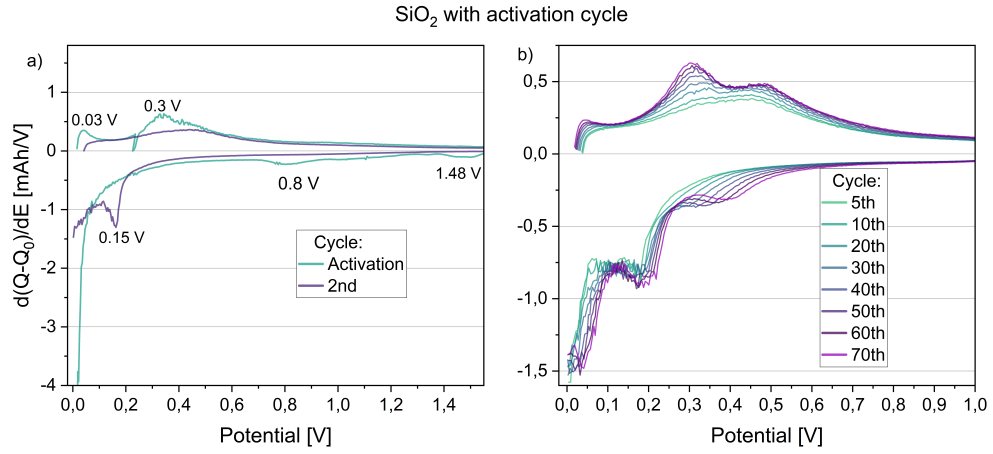


**Figure 4.20:** DC curve of $SiO_2$-based cell showing a) activation cycle at 50 $mAg_{-1}$ and 2nd cycle at 100 $mAg^{-1}$, and b) subsequent cycles at 100 $mAg^{-1}$

### 4.3.2 $SiO_x$/graphite composite anodes

The voltage profile of the $SiO_x$/graphite composite anode with activation cycle is presented in Figure 4.21 and the corresponding DC curve is presented in Figure 4.22. The initial discharge and charge capacities for the activation cycle is 985.2 $mAhg^{-1}$ and 538.5 $mAhg_{-1}$ respectively, giving an initial CE of 52.3. The decrease in capacity from pure $SiO_x$-based anodes is expected, as graphite comprises 70% of the active material. The subsequent cycles presents discharge and charge capacities at 462.3 $mAhg^{-1}$ and 405.2 $mAhg^{-1}$, which is a significant decrease, but gives a CE of 87.7%. As the cell is cycling, the capacity is not seen to diminish by much, seen in Figure 4.21b.

The DC curve of the activation cycle, in Figure 4.22a, a quite different curve than for the $SiO_x$-based anodes. Here, cathodic peaks are observed at 0.2 V, 0.15 V (broad peak), 0.1 V, and 0.08 V, and anodic peaks are observed at 0.44 V, 0.22 V, 0.18 V, 0.14 V and 0.1 V. For the second cycle the cathodic peak observed at 0.18 V disappears and a more defined cathodic peak is observed at 0.05 V, the intensity of all remaining peaks seem to dimish. The anodic peak observed at 0.44 V in the activation cycle, has disappeared for the second cycle, but the other peaks remain, albeit with a slightly lower intensity.

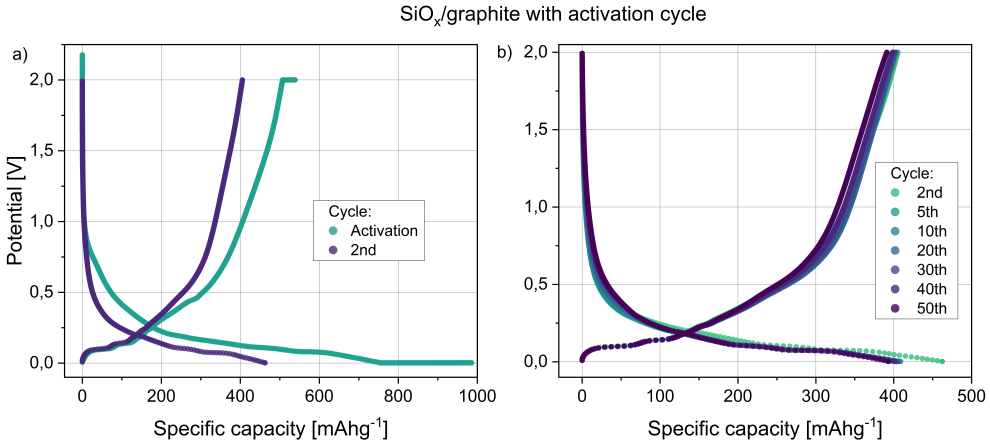


**Figure 4.21:** Voltage profile of $SiO_x$/graphite-based cell showing a) activation cycle at 50 $mAg_{-1}$ and 2nd cycle at 100 $mAg^{-1}$, and b) subsequent cycles at 100 $mAg^{-1}$

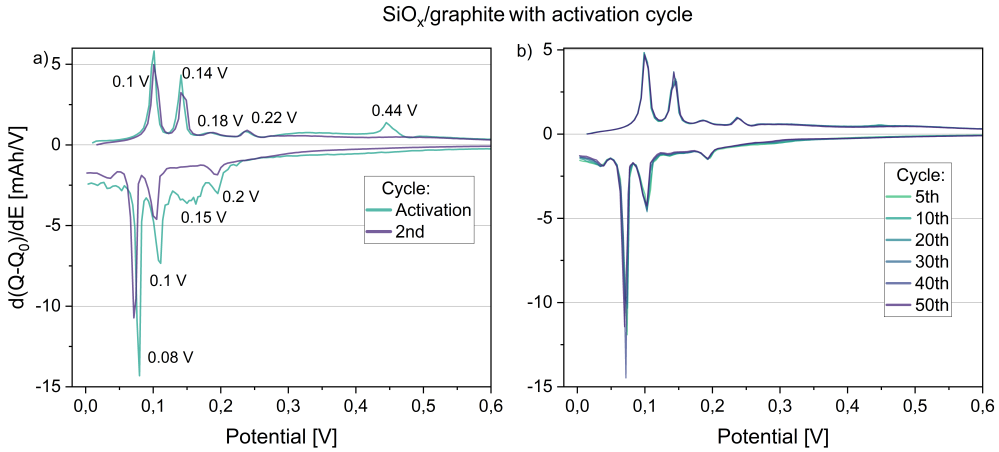


**Figure 4.22:** DC curve of $SiO_x$/graphite-based cell showing a) activation cycle at 50 $mAg_{-1}$ and 2nd cycle at 100 $mAg^{-1}$, and b) subsequent cycles at 100 $mAg^{-1}$

The voltage profile of the $SiO_x$/graphite composite anode without an activation cycle is presented in Figure 4.23 and the corresponding DC curve is presented in Figure 4.24. The initial discharge and charge capacities of the cell are 716.7 $mAhg^{-1}$ and 374.6 $mAhg^{-1}$, entailing an initial CE of 52.3%. The second cycle gives discharge and charge capacities of 408.1 $mAhg^{-1}$ and 371.1 $mAhg^{-1}$, giving the highest second cycle CE so far of 91.0%. In the subsequent cycling, in Figure 4.23b, the capacity actually increases slightly up to around cycle 40, before it starts to decrease slightly.

The DC curve of the first cycle, in Figure 4.24a, presents with cathodic peaks, similar to the cell with an activation cycle, at 0.2 V, 0.14 V, 0.1 V and 0.08 V, and anodic peaks at 0.22 V, 0.18 V, 0.14 V and 0.1 V. Interestingly, the anodic peak at 0.44 V and the cathodic peak at 0.05 V observed in the cell with an activation cycle is not present at all in the 2 first cycles of the cell without an activation cycle. In the second cycle, the cathodic and anodic peaks remain the same, except for the cathodic peak at 0.15 V, which disappears, and the peak intensity decreases slightly. In the subsequent cycling, the cathodic and anodic peaks remain, but a small cathodic peak at 0.05 V starts to emerge. A very small anodic peak can be seen at 0.44 V in the $5^{th}$ cycles, but disappears, quickly in the next cycles.

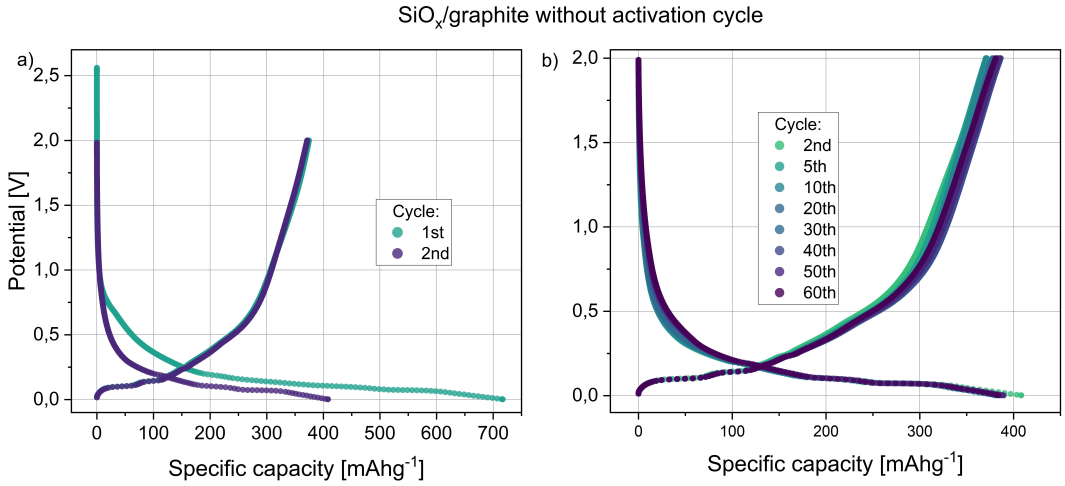


**Figure 4.23:** Voltage profile of $SiO_x$/graphite-based cell without activation cycle, showing a) 1st and 2nd cycle at 100 $mAg^{-1}$, and b) subsequent cycles at 100 $mAg^{-1}$

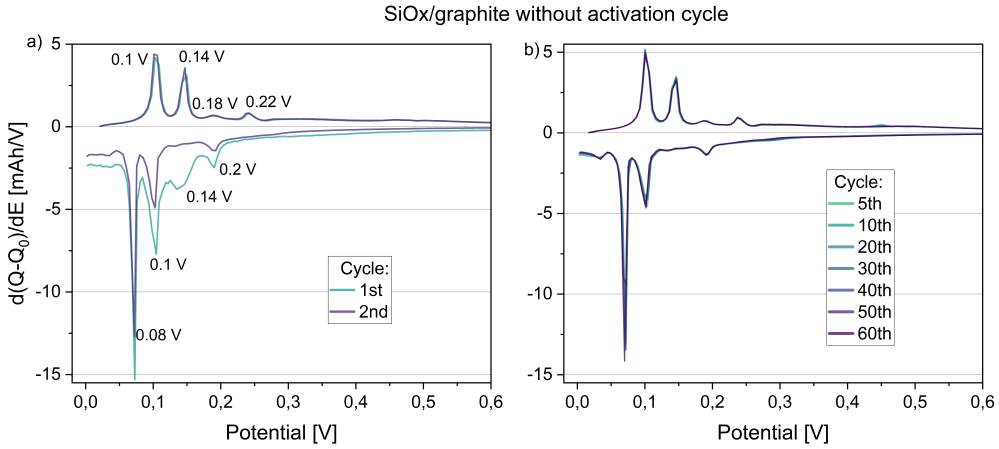


**Figure 4.24:** DC curve of $SiO_x$-based cell without activation cycles, showing a) 1st and 2nd cycle at 100 $mAg^{-1}$, and b) subsequent cycles at 100 $mAg^{-1}$

### 4.3.3 Comparison of anodes with different active material

In an attempt to compare the behavior of cells with different active material compositions, the discharge and charge capacities and CE for the two initial cycles, as well as ICL for the first cycle has been summarized in Table 4.4.

**Table 4.4:** Capacities during charge and discharge during the first and second cycle, initial capacity loss and coulombic efficiency for the different cell compositions. Cells that underwent an activation cycle at 50 $mAg^{-1}$ is denoted with an A and cells that started cycling directly at 100 $mAg^{-1}$ is denoted NA.

| Anode | Capacity $1^{st}$ [$mAhg^{-1}$] | | Capacity $2^{nd}$ [$mAhg^{-1}$] | | CE $1^{st}$ [%] | CE $2^{nd}$ [%] | ICL $1^{st}$ [%] |
|---|---|---|---|---|---|---|---|
| | Discharge | Charge | Discharge | Charge | | | |
| $SiO_x$-A | 2352.0 | 1277.0 | 1089.8 | 947.4 | 54.3 | 86.9 | 45.7 |
| $SiO_x$-NA | 2002.0 | 1027.4 | 1111.6 | 991.8 | 51.3 | 89.2 | 48.7 |
| $SiO_x$/Gr-A | 985.2 | 538.5 | 462.3 | 405.2 | 54.7 | 87.7 | 45.3 |
| $SiO_x$/Gr-NA | 716.7 | 374.6 | 408.1 | 371.4 | 52.3 | 91.0 | 47.7 |
| $SiO_2$-A | 2361.1 | 834.5 | 682.2 | 569.1 | 34.3 | 83.4 | 65.0 |

The discharge and charge capacities, as well as CE, for cycle 5 and 40 are presented in Table 4.5. The $5^{th}$ and $40^{th}$ cycles were chosen to compare the difference from the initial cycles and the performance after continued cycling. As the pristine $SiO_x$ based anodes only reached cycle 40 at the time of writing, this was chosen as a basis for comparison of the cells.

**Table 4.5:** Capacities during charge and discharge during the 5th and 40th cycle and coulombic efficiency for the different cell compositions. Cells that underwent an activation cycle at 50 $mAg^{-1}$ is denoted with an A and cells that started cycling directly at 100 $mAg^{-1}$ is denoted NA.

| Anode | Capacity 5th cycle [$mAhg^{-1}$] | | Capacity 40th cycle [$mAhg^{-1}$] | | CE [%] | |
|---|---|---|---|---|---|---|
| | Discharge | Charge | Discharge | Charge | 5th | 40th |
| $SiO_x$-A | 932.8 | 905.3 | 805.1 | 796.4 | 97.1 | 98.9 |
| $SiO_x$-NA | 1019.9 | 971.0 | 938.2 | 925.4 | 95.2 | 98.6 |
| $SiO_x$/Gr-A | 409.0 | 399.0 | 401.0 | 399.0 | 97.6 | 99.4 |
| $SiO_x$/Gr-NA | 386.0 | 370.3 | 390.0 | 386.2 | 96.1 | 99.2 |
| $SiO_2$-A | 603.7 | 581.5 | 728.0 | 721.4 | 96.3 | 99.1 |

Figure 4.25 presents the discharge capacity of half-cells with different compositions against cycles number. As the activation cycle for the activated cells and first cycle of the non activated cells display vastly higher discharge capacities, they are not included in the figure, but they are found in the above presented tables.

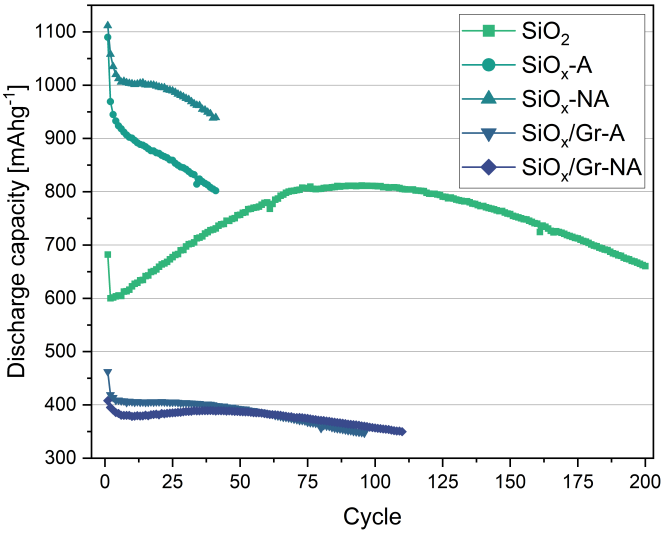


**Figure 4.25:** Discharge capacity as function of cycle number for the different cell compositions. Cells that underwent an activation cycle at 50 $mAg^{-1}$ is denoted with an A and cells that started cycling directly at 100 $mAg^{-1}$ is denoted NA.

Figure 4.26 presents CE values corresponding to the half-cells with different compositions against cycle number. As the activation cycle for the activated cells and first cycle of the non activated cells display relatively low CEs, they are not included in the figure, but they are found in the above presented tables.

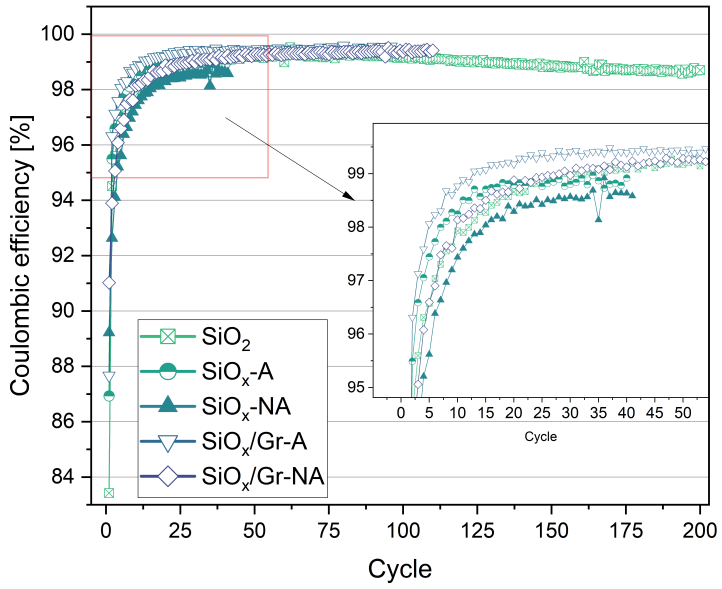


**Figure 4.26:** Coulombic efficiency as function of cycle number for the different cell compositions. Cells that underwent an activation cycle at 50 $mAg^{-1}$ is denoted with an A and cells that started cycling directly at 100 $mAg^{-1}$ is denoted NA.

## 4.4 In-situ XRD

The diffractograms for the first and second discharge/charge cycles with corresponding potential are presented in Figure 4.27 and Figure 4.28. For the first cycle, the potential starts at ≈ 0.7 V, due to the initial $V_{OC}$ of the cell being relatively low. The diffractograms depict the ranges of b) 10.8-12.5°, c) 18.5-20.0° and 20.0-22.0°. The first diffractogram in Figure 4.27b shows the graphite (002) peak at 12.13°, with the full lithiation/delithiaton cycle. The peak starts to shift to lower angles, as the potential lowers towards 0.21 V and a peak broadening is visible, before the phase transformation into $LiC_{12}$. The oppsosite can then be seen, as the (002) peak of $LiC_{12}$ shifts towards higher angles as the potential increases, with peak broadening and then the phase transition back to graphite (002).

In the same diffractogram, the (111) peak of Si is very prevalent at 13.0°, as the discharge/charge cycle goes on the intensity of the peak diminishes, but still remains visible. A shift can be observed at higher potentials at the end of the first cycle, which is then observed again at the start of the second cycle, Figure 4.28b. Here, the reduction in peak intensity is more prevalent. The behavior of the graphite (002) and $LiC_{12}$ remains the same as for the first cycle. In Figure 4.27c, the graphite

(100) peak at 19.2° and $LiC_{12}$ (110) peak at 19.1° are observed. During the first lithitation the graphite peak seems broader at first before it shifts towards lower angles. Lithiation at graphite (100) peak also occurs at lower potentials than the (002) peak. This is also observed in the second cycle, in Figure 4.28b.

In both cycles, the (111) Cu peak at 19.55° is visible. This peak is attributed to the current collector made of Cu. In Figure 4.27d, the (101) peak of graphite is observed, but is also quite broad, and another peak could be masked by it. During lithitation/delithiation, a small loss of intensity is observed, which is also visible in the second cycle, in Figure 4.28d). The (220) peak of Si is observed at 21.3° is observed to behave the same as the (111) peak of Si, experiencing a slight shift towards higher angles, becoming more prevalent at higher potentials, and is clearly observable at the beginning of the second lithiation, in Figure 4.28d.

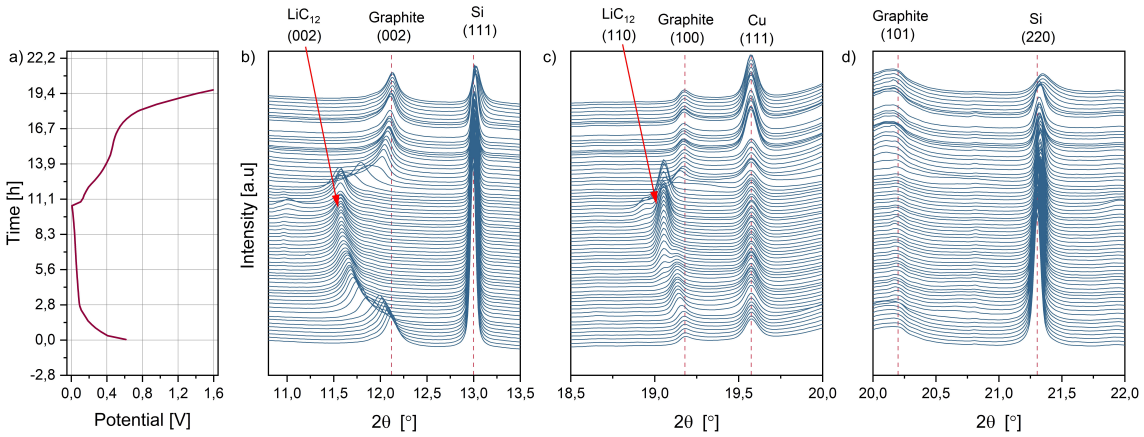


**Figure 4.27:** Results obtained by in-situ XRD of the first discharge/charge cycle, with a) a GC curve with time against potential, and diffractograms depicting the 2θ ranges of b) 10.8-13.5°, c) 18.5-20.0° and d) 20.0-22.0°. Peaks of interested are marked with a dotted red line.

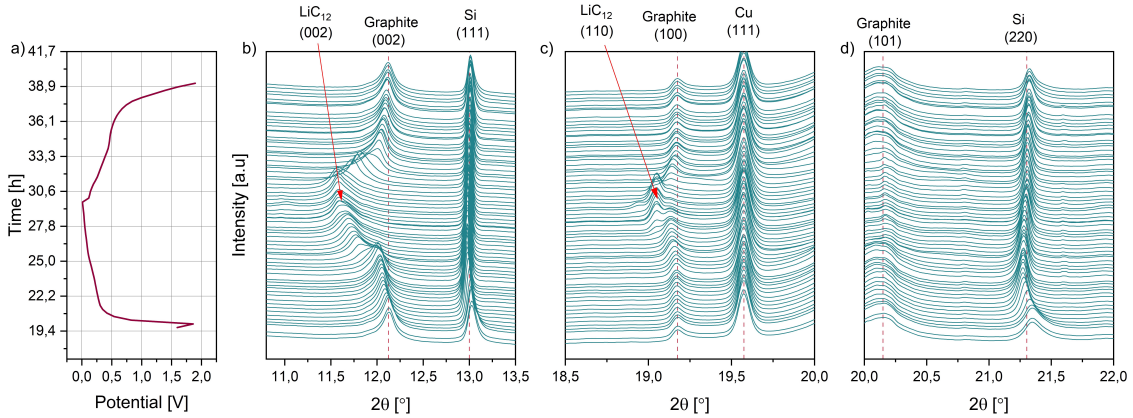


**Figure 4.28:** Results obtained by in-situ XRD of the second discharge/charge cycle, with a) a GC curve with time against potential, and diffractograms depicting the 2θ ranges of b) 10.8-13.5°, c) 18.5-20.0° and d) 20.0-22.0°. Peaks of interested are marked with a dotted red line.

In Figure 4.29 and Figure 4.30, diffractograms in the 2θ ranges of 24.5-25.5°, 30.0-30.5° and 32.5-34.0° for the first and second cycle, with corresponding potential, are presented. The (311) peak of Si is clearly observable at 25.05°, in Figure 4.29b. As the potential lowers, there is a clear shift towards higher angles, while the intensity simultaneously diminishes substantially, which could be an indication of a phase transition towards an amorphous phase. The peak remains in the second cycle, but sharpens up and shifts towards lower angles as lithitation proceeds, before again shifting back towards higher angles. The same is observed for the (400) peak of Si at 30.3°, in Figure 4.29c, but here the peak intensity is substantially lower. As lithiation proceeds, the peak shifts towards higher angles and flattens out. When delithitation starts, the peak is observed to shift back, but the peak flattens almost completely by the end of the first cycle.

In the second cycle, the peak is barely visible. The (331) peak of Si, at 33.1°, displays the same behavior, in Figure4.29d but the peak intensity is substantially lower than that of the Si (311) peak. The (110) peak of graphite at 33.55° display the same behavior as observed for the (002) and (100) peak of graphite, but lithiation is observed to start at quite low potentials.

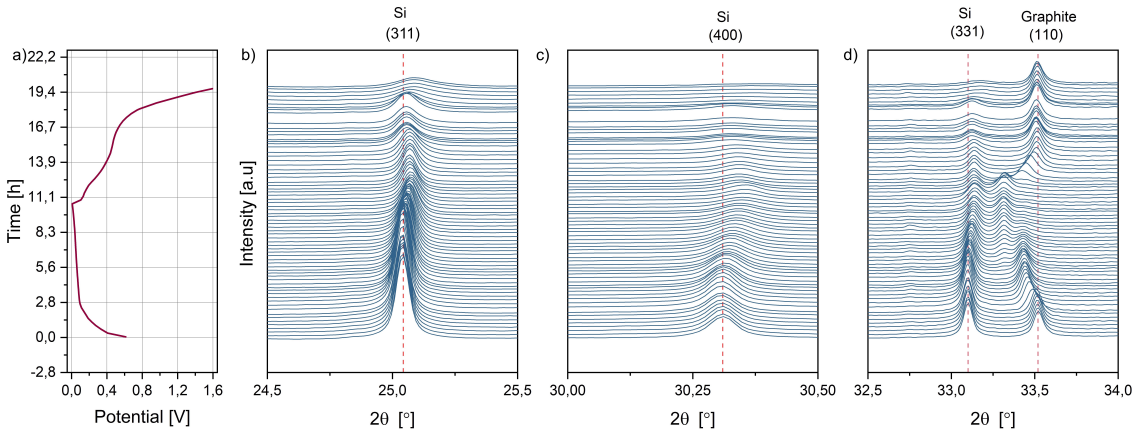


**Figure 4.29:** Results obtained by in-situ XRD of the first discharge/charge cycle, with a) a GC curve with time against potential, and diffractograms depicting the 2θ ranges of b) 24.5-25.5°, c) 30.0-30.5° and d) 32.5-34.0°. Peaks of interested are marked with a dotted red line.

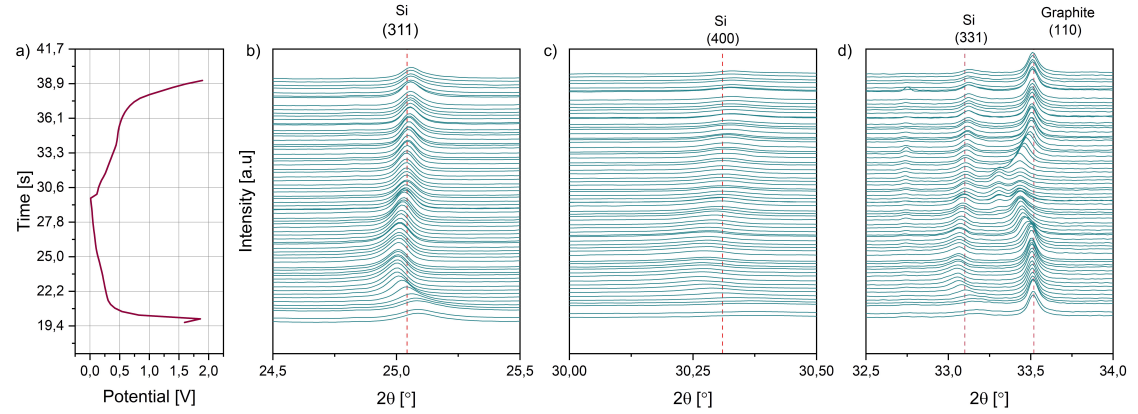


**Figure 4.30:** Results obtained by in-situ XRD of the second discharge/charge cycle, with a) a GC curve with time against potential, and diffractograms depicting the 2θ ranges of b) 24.5-25.5°, c) 30.0-30.5° and d) 32.5-34.0°. Peaks of interested are marked with a dotted red line.

# 5 Discussion

## 5.1 Effect of magnesiothermic reduction on diatom silica

From the Rietveld refinement data presented in Table 4.1, it is evident that the MgTR has been successful in yielding $SiO_x$, as both Si and $SiO_2$ are observed after MgTR. Sample MS15 is the only sample where $SiO_2$ was observed before acid treatment, but it is important to note that the $SiO_2$ was amorphous, as seen in Figure 4.1, and therefore the amount present given by Rietveld Refinement has to be interpreted with care. After the acidic treatment, $SiO_2$ is observed in both MS15 and MS16, but as previously stated, this has to be interpreted with care. Of the acid treated samples, MS10 was the only one where $SiO_2$ was not observed with Rietveld Refinement. All the aforementioned samples were reduced at 650°C, but molar ratios differed for each sample, and MS16 also had the inclusion of NaCl. This will be further discussed in Section 5.1.3 and 5.1.4. Nonetheless, MS15 was chosen for further structural characterization and as the active material for anodes.

### 5.1.1 Structure and microstructure after reduction

The SEM micrographs presented in Figure 4.9 show that the micro structure of the frustules are still intact after reduction, but display a rougher surface than originally observed in the pristine frustules. Previous works by Ruan *et al.* and Luo *et al.* have both reported similar results when using diatomacous earth, and described the surface as much more granular after reduction [17], [58]. However, the results from Luo *et al.* are based on a reduction process which includes the use of NaCl as a heat scavenger. Without using NaCl, they reported a total collapse of the original nanostructure present, which they attribute to a much higher local reaction temperature, than the original set reaction temperature. This was also observed in the frustules used in this thesis, shown in Figure B.1 and B.2 in Appendix B. Here, agglomerates are observed, consisting of very small particles. Some reminiscence of the original pore structure is observable, but it is difficult to ascertain if that is the case. However, the presence of preserved frustule structures gives an indication that it is possible to use MgTR to produce nanostructured Si and $SiO_x$. From the XRD difractograms presented in Figure 4.4 it can be observed that the amorphous $SiO_2$ structure observed on the as-received material can be partially converted into a mixture of crystalline Si and MgO after MgTR, and produced MgO can be success-

fully removed after the acidic treatment. Although the the coexistence of crystalline Si and amorphous $SiO_2$ can be confirmed by XRD results, a detailed study of the spatial distribution of such phases throughout the particles would be important to gain a better understanding about the MgTR. Such studies can be performed, for example by HRTEM.

### 5.1.2 Effect on specific surface area

From Figure 4.5 and Figure 4.6, it is very apparent that the MgTR has had a profound impact on the specific surface area (SSA) observed in the frustules. The pristine $SiO_2$ frustules already displayed a much higher SSA than DE frustules, $85.4\,m^2g^{-1}$ compared to $2.0\,m^2g^{-1}$ reported by Blanco *et al.* [11]. For the $SiO_x$, about a 5.4 increase to 465.6 $m^2g^{-1}$ is observed. This increase could be attributed to the creation of new mesopores, as unwanted reaction by-products (MgO, $Mg_2Si$, $Mg_2SiO_4$) are removed with acid treatment. By looking at the increase in external surface and micropore area in Figure 4.5, it is observed that near all of the increase is due to the increase in external area, which correlates with the creation of new macro- and mesopores, which is corresponds to the type II physisorption isotherm the $SiO_x$ presents with, Figure 4.6 [91]. The increase in SSA is also observed in the works of Luo *et al.* ($\approx$ 295.5 $m^2g^{-1}$) [17] and Ruan et al. ($\approx$ 110 $m^2g^{-1}$) [58]. However, in the work of Ruan 3 different acid treatment times were analyzed, and results showed first an increase in SSA with increase in acid treatment time and then a slight decrease when the treatment time was extended. They attributed the decrease in SSA to the acid etching the smaller mesopores, which created larger mesopores, effectively decreasing the SSA.

In this work, the obtained $SiO_x$ was acid treated for 12 h (compared to 0 h, 0.5 h and 1 h in the works of Ruan), using HCl acid in contrast to HF acid, which is used in most of the literature. The selection of HCl as acid agent allowed for the design of a more sustainable and environmentally friendly post reduction treatment. When comparing Figure 4.9 and Figure 4.10, showing the morphology of frustules before and after acid treatment, respectively, there is no discernible difference in the pore edges and structure. Thus, it is believed that the acid treatment did not effect the SSA in any crucial way. The effect of the increased SSA on the capacity and efficiency of the anodes is of high interest, since an increase in SSA is often desired in $SiO_x$-based anodes, to increase their reactivity towards Li-ions [8]. On one side, the increase in SSA could lead to shorter diffusion paths for $Li^+$, but on the other

side it could lead to extensive SEI formation, leading to detrimental effects on the cycling performance.

### 5.1.3 Effect of temperature at constant molar ratio

Based on what is presented in Table 4.1, it is observed that the Si, when using a molar ratio of 5.3:1, is almost absent at every reaction temperature, and the reacted samples primarily consist of MgO, $Mg_2Si$ and some residual Mg. Due to the excess amount of Mg in the sample, it is evident that reaction 2.23 is favored at all temperatures [82]. It is observed that the Mg content lowers as the temperature is increased, while the reaction products MgO and $Mg_2Si$ increases in amounts. The increase is slightly higher for $Mg_2Si$ than MgO, and this could be attributed to the fact that $Mg_2Si$ can also be formed in the presence of unreacted Mg vapor and Si according to the equation: $2Mg(g) + Si(s) = Mg_2Si(s)$ [93]. Residual Mg is only observed in samples with a high Mg:$SiO_2$ molar ratio.

At a different molar ratio of 2.5:1, it is observed that the amount of Si present gradually increases as the reaction temperature is increased, while the amount of $Mg_2Si$ gradually decreases. The same trend was observed by Larbi *et al.*, on the MgTR on rice husk ash to produce Si [93]. An increase of MgO is also observed with increasing temperatures, indicating that reaction 2.22 is favored at this molar ratio. The formation of MgO is seen as more favorable, than that of $Mg_2Si$, since MgO can easily be removed with HCl acid treatment [94], and it does not consume Si in its formation, i.e. it does not affect the Si yield directly [81].

Sample MS10, 2:1 molar ratio, has the highest Si yield of all samples, and only MgO is observed as a byproduct. Hence, it can be assumed that reaction 2.22 is favored. When increasing the temperature from 650°C to 700°C at the same molar ratio, a decline in both Si and MgO is observed, while $Mg_2Si$ and $Mg2SiO_4$ is now present. This could be attributed to Mg availability declining as MgO and $Mg_2Si$ is formed, and therefore insufficient amount of Mg at the $SiO_2$/MgO interface leads to reaction 2.24 to be favored [93].

For sample MS15, with a 1:1 molar ratio, it could be expected that reaction 2.24 should be favored, as there is insufficient Mg for reaction 2.22 to take place. However, only Si and MgO is observed from Rietveld refinement, and not $Mg_2SiO_4$ as expected from reaction 2.24 [81], [94]. This could be attributed to reaction 2.24 having a less negative $\Delta G$ value than reaction 2.22, leading the latter to be favored.

### 5.1.4 Effect of molar ratio at constant temperature

From the Rietveld refinement results presented in Table 4.1, a decrease in unreacted Mg is observed when decreasing the molar ratio, as expected, due to the lesser amount of $SiO_2$ available for the different reactions to take place. A decrease can also be seen in the amount of $Mg_2Si$ present, in tandem with an increase in MgO. Hence, showing that reaction 2.22 is preferred over reaction 2.23 [81], [82].

MgO is most prevalent in the sample made with 2:1 ratio at 650°C, where the only other product is Si before acid treatment. The 2:1 molar ratio used in this experiment, corresponds to the ratio in reaction 2.22. After the acid treatment, Table 4.2, the same sample present 99.9% Si, and yielding no $SiO_2$. Hence, the reaction has taken place fully and yielding no $SiO_x$. When the molar ratio is decreased to 1:1, there becomes a Mg deficiency and reaction 2.24 is expected to be favored. However, this reacted sample does not present any $Mg_2SiO_4$, Table 4.1. Only MgO, Si and unreacted $SiO_2$ is present, indicating that equation 2.22 has taken place partially.

### 5.1.5 Effect of acid treatment on reduced diatoms

The results from the Rietveld refinement of acid treated samples presented in Table 4.2, indicate the successful removal of unwanted byproducts. This can also be seen from the EDS maps in Figure 4.11 and 4.12, and the map sum spectra given in Appendix C, showing that the amount of Mg present is reduced to that of other trace elements. This is as expected for sample MS10 and MS15, where the only byproduct present according to Rietveld refinement analysis is MgO, Table 4.1. Such unwanted compound is expected to be easily removed with HCl [81], [94]. Interestingly, sample MS16 presented 23.78% of $Mg_2Si$, and this compound is no longer present in the acid treated counterpart. Thus, the approach of only using HCl and avoiding HF for the removal of unwanted byproducts is deemed successful.

### 5.1.6 Effect of heat scavenger agent

When looking at the diffractograms in Figure 4.3, it is clear that the addition of a heat scavenger has had an effect. Sample MS16 with the inclusion of NaCl at a Mg:$SiO_2$:NaCl molar ratio of 2.4:1:5.35 present sharper and narrower peaks than the samples without a heat scavenger, indicating a higher degree of crystallinity in the sample. Before acid treatment the sample present with 23.78% of MgO and 23.78%

$Mg_2Si$, Table 4.1, as well as 5.44% Si and NaCl. The sample contains a small excess of Mg, which corresponds equation 2.23 to be favored, however, the presence of MgO in equal amounts, suggest that equation 2.22 has taken place as well [17], [82]. Sample MS2, has the closest molar ratio, with 2.5:1, to MS16 and same reaction temperature, but without the inclusion of NaCl. When comparing the MgO content in both samples, it is observed to decrease drastically when NaCl is included, from 62.46% to 23.78%, indicating a limitation to equation 2.22. In Table 4.2 after the acidic treatment of the sample with NaCl, the unwanted Mg phases as well as NaCl has been succesfully removed [81], [94], resulting in a composition of about 74% Si and about 26% $SiO_2$. Thus, yielding $SiO_x$ with a lower oxygen content, which could be beneficial for using as active material in anode in terms of optimizing ICL and capacity [15]. To further optimize the addition of a heat scavenger, KCl could be used instead of NaCl. KCl has been found to easier control the crystallinity in Si, resulting in more stable cycling behavior when used as active material in anodes [57].

Based on the results presented it is evident that temperature, molar ratio and additives play a significant role in the MgTR of $SiO_2$ to produce $SiO_x$.

## 5.2 Electrochemical performance

### 5.2.1 $SiO_x$ anodes

The voltage profiles of $SiO_x$-based anodes are in Figure 4.15 and 4.23, both display impressive initial discharge capacities, but the subsequent charge capacities lead to low CE of 54.3% and 51.3% for the activated and non activated cell, respectively, in the first cycle, and a very high ICL of 45.7% and 48.7%, respectively. This drastic change is as expected, due to the irreversible formation of $Li_2O$, lithium silicates and the formation of the SEI [15].

In the corresponding DC curves in Figure 4.16 and Figure 4.18, a broad cathodic peak is observed at 0.7 V in the first cycle, indicating the reaction of $SiO_2$ into irreversible $Li_2O$ and electroactive Si [51], and the formation of the SEI layer [12]. The two subsequent peaks at 0.2 V and 0.1 V can be associated with the electrochemical allyoing reaction between Li and Si, together with the anodic peaks appearing in both anodes [95]. However, the anodic peak at 0.44 V, is much more prevalent in the activated anode, in Figure 4.16a, than in the non activated anode, in Figure

4.18a. The activation cycles performed on $SiO_2$ anodes based on diatom frustules, have been done to ensure a gradual and homogeneous formation of the SEI layer and to ensure that the Li-ions have sufficient time to react with the $SiO_2$ [12]. An added benefit of this procedure is to avoid a capacity increase in subsequent cycling, making it difficult to ascertain what the maximum capacity is [11]. When comparing the anodic 0.4 V peak in the activation cycle with subsequent cycle, in Figure 4.16a, it is observed that it almost completely disappear. However, in Figure 4.16b, it reappears during continued cycling of the cell. This could indicate that the jump in current from 50 $mAg^{-1}$ to 100 $mAg^{-1}$ leads to a halt for the delithiation of Si during the second cycle. For the non activated $SiO_x$ cell, in Figure 4.18a, the anodic 0.44 V peak is less prevalent during the first two cycles, but in contrast to the activated cell, it is prevalent in both cycles. In the subsequent cycles, in Figure 4.18b, the peak is still observed and seems to keep its intensity. This could be an indication of the system reaching more reversible lithiation/delithiation reactions.

The DC curve of the $SiO_2$ anode, in Figure 4.20 presents with a similar curve to that of the $SiO_x$ based cells, but with a clear distinction, which is the absence of the 0.44 V anodic peak. The cathodic and anodic peaks grow quite clearly over continued cycles, owing to the capacity increase this cell experiences, in contrast to the $SiO_x$ cells.

From Figure 4.15b, the specific capacity of the activated $SiO_x$ anode can be seen to diminish almost immediately, which is also seen in Table 4.4 and 4.5. From the second cycle to the fifth cycle, there is a 14.4% decline from 1089.8 $mAhg^{-1}$ to 932.8 $mAhg^{-1}$. For the non activated cell, in Figure 4.17b, there is a clear difference from the activated cell. This cell seems to have a more stable cycling performance, but it still experiences some losses in capacity, at about a 8.2% decrease from the second to fifth cycle. However, this is about half the amount experienced by the activated cell.

The CE is observed to generally higher for the activated cell, indicating that the activation have had some stabilizing effect. The loss in capacity during the initial cycles in $SiO_2$ anodes is usually attributed to the SEI formation and conversion into irreversible compounds, as mentioned earlier [11], [12], [15]. When comparing the ICL of the two $SiO_x$-anodes with the $SiO_2$ anode, it is immediately evident that using $SiO_x$, regardless of activation or not, has improved the ICL, from 65% for the $SiO_2$ anode, to 45.7% and 48.7% for the activated and non activated $SiO_x$ anodes. Thus, it can be claimed that the higher amount of Si present in the material, can

improve the initial loss of capacity [96].

The detrimental effect seen in Si based anodes, starts to appear quite quick in both $SiO_x$ cells. Both cells experience, as mentioned above, a significant loss in capacity during cycling. In Table 4.5, the capacities at the $40^{th}$ cycles for the different cells are presented. Here, it is observed that the capacities have diminished by about 26% for the activated cell and about 16% for the non activated cell compared to the $2^{nd}$ cycle.

In Figure 4.25, this is visually presented. This is in contrast to the $SiO_2$ cell, which in the first 100 cycles experiences an increase in capacity, before it starts to diminish. This could be attributed to the $SiO_2$ cells not having Si available from the initial cycle, compared to the $SiO_x$ cells. Hence, the volume expansion, and subsequent pulverization, is not experienced immediately in the $SiO_2$ cells, as opposed to the $SiO_x$ cells. Due to the limited timespan of this thesis work, it is not possible to observe the continued cycling behavior of the two $SiO_x$ cells, but some assumptions can be made. Based on the trend of diminishing capacity, seen in both the activated and non activated $SiO_x$ cells, it can be assumed that the capacity will continue to fade as the cycling is prolonged. Based on the steepness of the curves in Figure 4.25, it seems as the activated $SiO_x$ cells capacity will diminish slightly faster than that of the non activated $SiO_x$ cell. As of cycle 40, there is no indication that the cells will stabilize at any point.

### 5.2.2 $SiO_x$/graphite composite anodes

The voltage profile of the activated $SiO_x$/graphite cell, in Figure 4.21a, immediately displays the high initial discharge capacity of 985.2 $mAhg^{-1}$ associated with using $SiO_x$-based materials in anodes [97]. However, the subsequent cycle displays a significantly lower charge capacity of 538.5 $mAhg^{-1}$, entailing an initial capacity loss of about 45%, comparable to that of the pristine $SiO_x$ anodes. The overall capacity that the $SiO_x$/graphite anode displays, is significantly lower than that of the pristine $SiO_x$ anode. This is expected as graphite comprises 70% of the active material in the anode. With continued cycling from the $5^{th}$ to the $40^{th}$ cycle, from Table 4.5, the anode only experiences a slight decrease in the capacity, signifying the high structural and cycling stability of the graphite [25]. Although, the capacity is more or less stable, it does not display a high increase over the theoretical capacity of graphite, with $\approx$ 400 $mAhg^{-1}$ at the $40^{th}$ vs. 372 $mAhg^{-1}$ [25]. Furthermore, it can be seen in Figure 4.25, that the capacity fades more prominently after around

the $40^{th}$ cycle. To improve the electrochemical performance of the $SiO_x$/graphite composite anode, the use of electrode additives such as Styrene-Butadien Rubber (SBR) and CB could be employed [16].

During the initial cycle in the DC curve of the activated $SiO_x$/graphite anode, Figure 4.22a, the cathodic and anodic peaks corresponding to the lithiation and delithiation of graphite are observed [71]. Furthermore, there is a distinct anodic a peak at 0.44 V, only visible in the first cycle, associated with the delithiation of Si. The peak can also be associated with the transformation of crystalline $Li_{15}Si_4$ into amorphous Si [98]. This crystalline $Li_{15}Si_4$ phase has been reported to hamper the cycling stability of Si-based anodes [71], [99]. The formation of this crystalline phase is reported to occur at around 0.05 V during the lithiation of Si [99], and the absence of an anodic peak at 0.44 V, in the subsequent cycling of the cell, in Figure 4.22a and 4.22b, could be indicative of this phase remaining in the anode. Hence, the Si in the anode is not able to fully delithiate, causing the lowered capacity observed. However, multiple reactions can occur at the other potentials [84], leading to convoluted peaks. Thus, the contribution of graphite versus Si can be difficult to ascertain.

The $SiO_x$/graphite cell without an activation cycle displays a similar voltage profile, Figure 4.23a, to the activated one, albeit with lower discharge and charge capacities. The initial discharge capacity is still relatively high, at 716.7 $mAhg^{-1}$, but it still displays the characteristic of a cell with $SiO_x$ as active material [97]. The ICL is higher for the non activated cell versus the activated cell, 47.7% vs. 45.3%, respectively. Thus, the activation cycle seems to be beneficial for retaining the capacity and more fully taking advantage of the added $SiO_x$ in the graphite. As opposed to the activated cell, the non activated cell actually increases in capacity over prolonged cycling, from 386 $mAhg^{-1}$ at the $5^{th}$ cycle to 390 $mAhg^{-1}$ at the $40^{th}$ cycle. Which is similar behavior to what the $SiO_2$-based cell experience, and $SiO_2$ as active material in general [12]. The capacity however, is very close to theoretical value of graphite, which can indicate that the $SiO_x$ does not contribute very much to the overall capacity in the non activated cell [25]. Over continued cycling, Figure 4.25, it is evident that the capacity starts to fade again after the $40^{th}$ cycle, similarly to the activated cell.

From the DC curve of the non activated cell during the initial cycles, Figure 4.24a, the 0.44 V anodic peak associated with the delithiation/transformation of $Li_{15}Si_4$ into amorphous Si is not present at all. Which can be an indication of the Si

not being able to fully delithiate, and hence not being able to contribute to the overall capacity. In Figure 4.24b, a very small peak is visible for the $5^{th}$ cycle at 0.44 V, but it is barely present and does not appear in the other cycles. As stated previously, the occurence of convoluted peaks makes it difficult to discern some of the peaks from each other, but from the capacity displayed, it is clear that the $SiO_x$ only contributes a small part to the capacity. The cathodic peak 0.05 V is also more prevalent during subsequent cycling, Figure 4.24b, which could indicate the formation of the crystalline $Li_{15}Si_4$ phase, but without the following transformation to amorphous Si, this would only lead to consumption of Li. Therefore, leading to the capacity fade and eventual failure of the cell. In a half cell configuration, where the counter electrode is Li foil, this problem is not as crucial, but in a full cell configuration, where the Li-ions are limited, this will be detrimental to the electrochemical performance.

### 5.2.3 Comparison of cells with different active materials

When comparing the electrochemical results of the cells with different compositions of active material, in Table 4.4 and 4.5, it is clear that electrochemical performance is highly dependant on the composition. By decreasing the oxygen content in stoichiometric $SiO_2$ to under-stoichiometric $SiO_x$ the high ICL usually observed is lowered by over 15%, as also observed by Yang *et al.* [59]. By controlling the oxygen content more precisely, an even lower ICL could be obtainable [59]. However, more precise techniques are need to ascertain the amount of $SiO_2$ in relation to Si in the $SiO_x$, as in the Rietveld Refinement used in this work only gives an estimate of $SiO_2$ content, due to its amorphous nature. The initial CEs of the activated and non activated pristine $SiO_x$ cells are 54.3% and 51.3%, respectively. However, Yang *et al.* observed an initial CE of about 70%, but their material included a nitrogen doped carbon structure [59]. Further attempts to lower the ICL and increase the CE in the first cycles could be pre-lithitation of the anode prior to cycling [70].

Comparing the pristine $SiO_x$ cells to the $SiO_x$/graphite composite anode, the first major difference is the difference in capacity. The decrease in capacity observed, was expected as 70% of the active material is graphite, although it was not expected to be close to the theoretical capacity of graphite. Xiong et al. reported capacities above 600 $mAhg^{-1}$ when combining $SiO_x$ with graphite [16]. However, their findings are based on an anode consisting of only 15% $SiO_x$ and 85% graphite. Indicating that the ratio of $SiO_x$ to graphite is crucial for the electrochemical performance.

Therefore, different $SiO_x$ to graphite ratios should be carefully considered during manufacture, to find the optimal ratio to increase performance, instead of decreasing it. In addition, Xiong et al. used poly acrylic acid and SBR as a binder, in contrast to the Na-Alg binder used in this work. Signifying the importance of the binder as well. Also, the addition of low amounts of CB has shown to have a beneficial effect in combining Si-based particles with graphite.

Regarding the implementation of activation cycles, as has been used in anodes with $SiO_2$ diatom frustules before [11], [12], it is clear that it has had a small positive effect on the initial CE and ICL of the $SiO_x$ and $SiO_x$/graphite anodes. Both the activated cells display a higher initial capacity than its non activated counterpart, confirming that there still is a need for an activation cycle when using anodes containing $Si/SiO_x$. It would be interesting to see if the 5 activation cycle protocol proposed by Renman [12] and Blanco [11], would benefit the electrochemical performance of the $SiO_x$/graphite composite anode, so that a bigger proportion of the amorphous $SiO_2$ in the active material will convert to electroactive Si domains, which will then contribute to the overall anode capacity.

The cycling behavior of the different cells, Figure 4.25, show that the composite anode experiences less capacity decay, which is likely due to the presence of graphite. As the pristine $SiO_x$ cells barely had 40 cycles, it is difficult to conclude how the behavior would evolve over time, but it is likely to continue with a drastic decrease in capacity or a cell failure. Both $SiO_x$/graphite anodes managed to reach about 90 cycles, and this is likely due to the drastic difference in capacity compared to pristine $SiO_x$ cells. It is worth to note that all the cells described, except for the $SiO_2$-based cell, were put on cycling at the same time.

## 5.3 In-Situ XRD

When anodes are comprised of two or more different active materials, it is crucial to understand how the different materials lithiate/delithiate and how the structural changes in each active material affects one another. In Figure 4.27b, the evolution of graphite main Bragg reflection (002) during the first lithiation/delithiation cycle of the $SiO_x$/graphite anode is observed. As the potential decreases towards 0.21 V, there is a peak shift towards lower angles, which is accompanied with peak broading. This corresponds to the insertion of Li-ions in between the graphene sheets, increasing the lattice parameters before the phase transition into the $LiC_6$ phase

[100]. This is in agreement with the presence of a cathodic peak observed at 0.2 V in the DC curve of the $SiO_x$/graphite composite anodes, Figure 4.22 and 4.24. The full lithiation is achieved at ≈ 0.08 V, which is visible in both the diffractograms, since the peak has stabilized, and in the DC curve [71]. The delithiation of graphite occurs before that of Si, at ≈ 0.09 V, and it can be seen, from Figure 4.27b, as the peak starts to broaden and shift towards the original 2θ position. This is also observed in the second cycle, and for the (100) graphite peak in both cycles, shown in Figure 4.27c and 4.28c.

The immediate lithiation of the Si (111) peak is not as visible, Figure 4.27b, but occurs slightly before that of graphite, at 0.2 V, which is also seen as a broader peak in the DC curves, due to it overlapping with the lithiation of graphite [71]. During the first lithitation/delithation cycle, the peak intensity decreases for all the Si peaks observed, signifying the transition from crystalline Si phases to amorphous Si phases [63]. However, after the first cycle, and also the second cycle in Figure 4.28, both the Si (111) and Si (220) reflection presents sharp and defined peaks, indicating that reaction to form amorphous Si, has not taken place fully. Some form of reaction is present, as the Si (220) at 21.35° is observed to shift towards higher angles during the lithiation and back towards lower angles again during the delithiation, indicating the expansion and contraction of the Si lattice. This could presume that Si and Li could form a solid solution during the cycling, but not enough Li-ions inserts into the Si lattice for it to fully transform into an amorphous phase, which is by the author knowledge not something that has been previously reported.

In Figure 4.29b and 4.29c, the (311) and (400) peaks of Si is observable. They both present distinctively different than that of the (111) and (220) Si peaks. The intensity of the (400) peak quickly disappears during the first lithiation, but as observed in the other peaks, it also shifts towards higher angles. This is an indication that there is sufficient Li inserted into the Si lattice to complete the phase transformation to amorphous $Li_xSi$ [37]. In the second cycle, in Figure 4.30c, the peak has almost completely flattened out. The (311) peak of Si at ≈ 25°, behaves similarly, presenting with a decrease in peak intensity and a peak shift towards higher angles. but is seen to get a more defined peek during the second lithiation, which does not disappear during the second lithiation, indicating that there is still crystalline Si present in the anode after the two cycles.

The presented results will help to shed light on the reaction mechanism of crystalline Si and graphite with Li-ions in $SiO_x$/graphite anodes. From the experimental data

it was possible to visualize the structural changes in Si, which can be summarized as distortion of the original Si lattice and amorphization, whereas in the case of graphite, the material preserves it crystalline structure upon electrochemical cycling. The presented datasets will be further analyzed in order to quantify structural changes in both active materials, since a full understanding of the lithiation/delithiation mechanism in $SiO_x$/graphite blends is critical for the design of improved electrodes.

# 6 Conclusion

In this thesis, the primary goal was to investigate the structural changes in a composite anode of $SiO_x$/graphite upon cycling, using in-situ XRD. Nanostructured $SiO_x$ was successfully obtained by magnesiothermic reduction of amorphous $SiO_2$ diatom frustules. The effect of temperature and molar ratio of reactants was investigated using XRD and SEM/EDS analysis. The optimal parameters were found and by using a Mg:$SiO_2$ molar ratio of 1:1 at a reaction temperature of 650°C, resulted in $SiO_x$ comprised of about 15% Si and about 85% $SiO_2$ after the post reduction acid treatment. Confirming that MgTR is a feasable pathway to synthesize nanostructured $SiO_x$. The specific surface aree was determined by BET area and t-plot analysis, were it was found to drastically increase from 85.4 $m^2g^{-1}$ in pristine $SiO_2$ frustueles to 465.6 $m^2g^{-1}$ in the synthesized $SiO_x$.

The obtained $SiO_x$ was then implemented as active material in anodes, to evaluate the electrochemical performance against anodes made with pristine $SiO_2$ frustules. Both the ICL and CE of the $SiO_x$ anodes improved compared to $SiO_2$ anode, in addition to higher capacities in the initial cycles. However, it was found that the $SiO_x$ anode immediately decreased in capacity for each cycle up to the $40^{th}$ and last recorded cycle, with a specific capacity of 805.1 $mAhg^{-1}$, whereas the $SiO_2$ anode increased steadily up until the $100^{th}$ cycle before showing the same decline. A $SiO_x$ cell was also tested without an activation cycle, and even though it displayed better ICL, CE and capacity initially than $SiO_2$, it was found to perform less better than the $SiO_x$ cell with an activation cycle in terms of CE and ICL. Showing the need for an activation cycle to still be relevant. However, it displayed a higher capacity, with 938.2 $mAhg^{-1}$ at cycle 40.

$SiO_x$ was then integrated into a $SiO_x$/graphite composite anode. From electrochemical characterization it was found that the composite anode display a significantly lower specific capacity compared to the pristine $SiO_x$ anode, but in terms of cycling stability, it was found perform better, owing to the stabilizing properties of graphite. By adding the $SiO_x$ into the graphite matrix, it was expected to increase the capacity of the composite anode, but it was found that the expected increase was not prevalent, displaying a specific capacity of 401 $mAhg^{-1}$ after 40 cycles. A composite anode was also tested without an activation cycle, but its performance decreased slightly compared to the activated composite anode and had a specific capacity of 390 $mAhg^{-1}$ after 40 cycles. Hence, further optimization of the $SiO_x$/graphite blend, ratio between active materials and cycling parameters are needed.

Lastly, the $SiO_x$/graphite composite anode was analyzed using in-situ synchrotron X-ray diffraction. It was found that during the lithiation and delithiation of Si, the material experienced distortion of the original lattice structure and amorphization, while graphite preserved the original crystalline structure. The peaks of Si was found to shift towards higher and lower angles during electrochemical cycling, indicating that the Si and Li-ions form a solid solution prior to phase transformations and amorphization of Si.

# 7 Further Work

This section serves to give suggestions on what can be done further to enhance the MgTR of $SiO_2$ and the performance of $SiO_x$/graphite composite anodes.

Regarding the MgTR process, the main aspect that should be considered is the optimization in controlling the ratio of Si to $SiO_2$, since the oxygen content of $SiO_x$, will have profound impact on the cycling behavior of anodes containing $SiO_x$ as active material. By utilizing a NaCl heat scavenger it has been shown to yield $SiO_x$ with a high Si to $SiO_2$ ratio as discussed in Section 5.1.6, which could be beneficial for the electrochemical performance. Further optimization with varying the amounts added and type of heat scavenger, i.e. KCl instead of NaCl, could be explored. Also characterizing the spatial distribution of phases in the material could be of interest, to investigate the effect this could have on the electrochemical performance.

$SiO_x$-based anodes displayed higher initial capacities, lower ICLs and higher CEs than anodes made with pristine $SiO_2$ frustules. However, they experienced decreasing capacities as cycling continued, as opposed to the $SiO_2$-based anode. It is therefore imperative to investigate the failure mechanism present in the $SiO_x$-based anodes, to try and ascertain the reason for this decline. This could be investigated by FIB/SEM to investigate the difference in anode morphology, during different cycles, to see how it evolves. Also the inclusion of different additives and binders should be considered.

The $SiO_x$/graphite composite anodes displayed with a more stable cycling behavior than the pristine $SiO_x$-based anodes, as well as comparable ICls and CEs. However, the capacity was vastly lower, concluding that the $SiO_x$ did not contribute to the overall capacity as expected. In earlier studies, a series of 5 activation cycles has been used in anodes made with $SiO_2$ frustules to ensure that the $SiO_2$ converts to electroactive Si domains. So to further enhance the composite anode, implementation of more activation cycles can be explored, so that a bigger proportion of the amorphous $SiO_2$ in composite anode will convert to electroactive Si domains. Here, the inclusion of additives, such as CB, and utilizing different binders, such as SBR, should also be considered.

# Bibliography


[1] M. S. Whittingham, 'History, evolution, and future status of energy storage', *Proceedings of the IEEE*, vol. 100, no. Special Centennial Issue, pp. 1518–1534, May 2012. DOI: 10.1109/jproc.2012.2190170.

[2] C. Julien, A. Mauger, A. Vijh and K. Zaghib, *Lithium Batteries*. Springer International Publishing, 2016. DOI: 10.1007/978-3-319-19108-9.

[3] J. Fleischmann, M. Hanicke, E. Horetsky *et al.*, 'Battery 2030: Resilient, sustainable, and circular', McKinsey & Company, Tech. Rep., 2022.

[4] X. Zuo, J. Zhu, P. Müller-Buschbaum and Y.-J. Cheng, 'Silicon based lithium-ion battery anodes: A chronicle perspective review', *Nano Energy*, vol. 31, pp. 113–143, Jan. 2017. DOI: 10.1016/j.nanoen.2016.11.013.

[5] L. Y. Beaulieu, K. W. Eberman, R. L. Turner, L. J. Krause and J. R. Dahn, 'Colossal reversible volume changes in lithium alloys', *Electrochemical and Solid-State Letters*, vol. 4, no. 9, A137, 2001. DOI: 10.1149/1.1388178.

[6] S. Xun, X. Song, L. Wang *et al.*, 'The effects of native oxide surface layer on the electrochemical performance of si nanoparticle-based electrodes', *Journal of The Electrochemical Society*, vol. 158, no. 12, A1260, 2011. DOI: 10.1149/2.007112jes.

[7] X. Cao, X. Chuan, R. C. Massé, D. Huang, S. Li and G. Cao, 'A three layer design with mesoporous silica encapsulated by a carbon core and shell for high energy lithium ion battery anodes', *Journal of Materials Chemistry A*, vol. 3, no. 45, pp. 22 739–22 749, 2015. DOI: 10.1039/c5ta05879a.

[8] B. Guo, J. Shu, Z. Wang *et al.*, 'Electrochemical reduction of nano-SiO2 in hard carbon as anode material for lithium ion batteries', *Electrochemistry Communications*, vol. 10, no. 12, pp. 1876–1878, Dec. 2008. DOI: 10.1016/j.elecom.2008.09.032.

[9] Z. Wang, J. Zhao, S. Liu *et al.*, 'Cultured diatoms suitable for the advanced anode of lithium ion batteries', *ACS Sustainable Chemistry & Engineering*, vol. 9, no. 2, pp. 844–852, Jan. 2021. DOI: 10.1021/acssuschemeng.0c07484.

[10] A. N. Norberg, N. P. Wagner, H. Kaland, F. Vullum-Bruer and A. M. Svensson, 'Silica from diatom frustules as anode material for li-ion batteries', *RSC Advances*, vol. 9, no. 70, pp. 41 228–41 239, 2019. DOI: 10.1039/c9ra07271c.

[11] M. V. Blanco, V. Renman, F. Vullum-Bruer and A. M. Svensson, 'Nanostructured diatom earth SiO2 negative electrodes with superior electrochemical performance for lithium ion batteries', *RSC Advances*, vol. 10, no. 55, pp. 33 490–33 498, 2020. DOI: 10.1039/d0ra05749e.

[12] V. Renman, M. V. Blanco, A. N. Norberg, F. Vullum-Bruer and A. M. Svensson, 'Electrochemical activation of a diatom-derived SiO2/c composite anode and its implementation in a lithium ion battery', *Solid State Ionics*, vol. 371, p. 115 766, Nov. 2021. DOI: 10.1016/j.ssi.2021.115766.

[13] R. Ragni, S. R. Cicco, D. Vona and G. M. Farinola, 'Multiple routes to smart nanostructured materials from diatom microalgae: A chemical perspective', *Advanced Materials*, vol. 30, no. 19, p. 1 704 289, Nov. 2017. DOI: 10.1002/adma.201704289.

[14] J. T. A. Karlsen, 'High performance $SiO_2$ anodes based on microalgae shells', Department of Material Science and Engineering, TMT4500 - Materials technology, specialization project, Dec. 2022.

[15] Z. Liu, Q. Yu, Y. Zhao *et al.*, 'Silicon oxides: A promising family of anode materials for lithium-ion batteries', *Chemical Society Reviews*, vol. 48, no. 1, pp. 285–309, 2019. DOI: 10.1039/c8cs00441b.

[16] Y. Xiong, H. Xing, Y. Fan *et al.*, 'SiOx-based graphite composite anode and efficient binders: Practical applications in lithium-ion batteries', *RSC Advances*, vol. 11, no. 14, pp. 7801–7807, 2021. DOI: 10.1039/d0ra10283k.

[17] W. Luo, X. Wang, C. Meyers *et al.*, 'Efficient fabrication of nanoporous si and si/ge enabled by a heat scavenger in magnesiothermic reactions', *Scientific Reports*, vol. 3, no. 1, Jul. 2013. DOI: 10.1038/srep02222.

[18] K. B. Oldham, J. C. Myland and A. M. Bond, *Electrochemical Science and Technology*. John Wiley & Sons, Ltd, Nov. 2011. DOI: 10.1002/9781119965992.

[19] A. Masias, J. Marcicki and W. A. Paxton, 'Opportunities and challenges of lithium ion batteries in automotive applications', *ACS Energy Letters*, vol. 6, no. 2, pp. 621–630, Jan. 2021. DOI: 10.1021/acsenergylett.0c02584.

[20] 'A vision for a sustainable battrey value chain in 2030', Global Battery Alliance, World Economic Forum, Tech. Rep., 2019. [Online]. Available: https://www3.weforum.org/docs/WEF_A_Vision_for_a_Sustainable_Battery_Value_Chain_in_2030_Report.pdf.

[21] J. B. Goodenough and K.-S. Park, 'The li-ion rechargeable battery: A perspective', *Journal of the American Chemical Society*, vol. 135, no. 4, pp. 1167–1176, Jan. 2013. DOI: 10.1021/ja3091438.

[22] J. Lu, Z. Chen, F. Pan, Y. Cui and K. Amine, 'High-performance anode materials for rechargeable lithium-ion batteries', *Electrochemical Energy Reviews*, vol. 1, no. 1, pp. 35–53, Mar. 2018. DOI: 10.1007/s41918-018-0001-4.

[23] P. Zhu, D. Gastol, J. Marshall, R. Sommerville, V. Goodship and E. Kendrick, 'A review of current collectors for lithium-ion batteries', *Journal of Power Sources*, vol. 485, p. 229 321, Feb. 2021. DOI: 10.1016/j.jpowsour.2020.229321.

[24] H. Berg, 'Batteries for electric vehicles', Aug. 2015. DOI: 10.1017/cbo9781316090978.

[25] K. Xu, 'Nonaqueous liquid electrolytes for lithium-based rechargeable batteries', *Chemical Reviews*, vol. 104, no. 10, pp. 4303–4418, Sep. 2004. DOI: 10.1021/cr030203g.

[26] J. R. Dahn, T. Zheng, Y. Liu and J. S. Xue, 'Mechanisms for lithium insertion in carbonaceous materials', *Science*, vol. 270, no. 5236, pp. 590–593, Oct. 1995. DOI: 10.1126/science.270.5236.590.

[27] K. Amine, I. Belharouak, Z. Chen *et al.*, 'Nanostructured anode material for high-power battery system in electric vehicles', *Advanced Materials*, vol. 22, no. 28, pp. 3052–3057, Jun. 2010. DOI: 10.1002/adma.201000441.

[28] C.-M. Park, J.-H. Kim, H. Kim and H.-J. Sohn, 'Li-alloy based anode materials for li secondary batteries', *Chemical Society Reviews*, vol. 39, no. 8, p. 3115, 2010. DOI: 10.1039/B919877F.

[29] M. T. McDowell, S. W. Lee, W. D. Nix and Y. Cui, '25th anniversary article: Understanding the lithiation of silicon and other alloying anodes for lithium-ion batteries', *Advanced Materials*, vol. 25, no. 36, pp. 4966–4985, Aug. 2013. DOI: 10.1002/adma.201301795.

[30] K. Cao, T. Jin, L. Yang and L. Jiao, 'Recent progress in conversion reaction metal oxide anodes for li-ion batteries', *Materials Chemistry Frontiers*, vol. 1, no. 11, pp. 2213–2242, 2017. DOI: https://doi.org/10.1039/C7QM00175D.

[31] E. N. Primo, F. Eroles, M. del Carmen Rojas *et al.*, 'Mechanical properties vs. interaction strength: Comprehensive understanding of aqueous binders' formulation on si-based anodes for lithium-ion batteries', *Journal of Power Sources*, vol. 563, p. 232 800, Apr. 2023. DOI: 10.1016/j.jpowsour.2023.232800.

[32] A. Magasinski, B. Zdyrko, I. Kovalenko *et al.*, 'Toward efficient binders for li-ion battery si-based anodes: Polyacrylic acid', *ACS Applied Materials & Interfaces*, vol. 2, no. 11, pp. 3004–3010, Nov. 2010. DOI: 10.1021/am100871y.

[33] N.-S. Choi, S.-Y. Ha, Y. Lee *et al.*, 'Recent progress on polymeric binders for silicon anodes in lithium-ion batteries', *Journal of Electrochemical Science and Technology*, vol. 6, no. 2, pp. 35–49, Jun. 2015. DOI: 10.33961/jecst.2015.6.2.35.

[34] P. B. Balbuena and Y. Wang, *Lithium-Ion Batteries*. May 2004. DOI: 10.1142/p291.

[35] R. by Sarah Ball, 'Electrolytes for lithium and lithium-ion batteries', *Johnson Matthey Technology Review*, vol. 59, no. 1, pp. 30–33, Jan. 2015. DOI: 10.1595/205651315x685517.

[36] J. B. Goodenough and Y. Kim, 'Challenges for rechargeable li batteries', *Chemistry of Materials*, vol. 22, no. 3, pp. 587–603, Aug. 2009. DOI: 10.1021/cm901452z.

[37] C. Zhang, F. Wang, J. Han *et al.*, 'Challenges and recent progress on silicon-based anode materials for next-generation lithium-ion batteries', *Small Structures*, vol. 2, no. 6, p. 2 100 009, Apr. 2021. DOI: 10.1002/sstr.202100009.

[38] M. Ashuri, Q. He and L. L. Shaw, 'Silicon as a potential anode material for li-ion batteries: Where size, geometry and structure matter', *Nanoscale*, vol. 8, no. 1, pp. 74–103, 2016. DOI: 10.1039/c5nr05116a.

[39] L. Li, C. Fang, W. Wei *et al.*, 'Nano-ordered structure regulation in delithiated si anode triggered by homogeneous and stable li-ion diffusion at the interface', *Nano Energy*, vol. 72, p. 104 651, Jun. 2020. DOI: 10.1016/j.nanoen.2020.104651.

[40] B. Campbell, R. Ionescu, M. Tolchin *et al.*, 'Carbon-coated, diatomite-derived nanosilicon as a high rate capable li-ion battery anode', *Scientific Reports*, vol. 6, no. 1, Oct. 2016. DOI: 10.1038/srep33050.

[41] Z. Favors, H. H. Bay, Z. Mutlu *et al.*, 'Towards scalable binderless electrodes: Carbon coated silicon nanofiber paper via mg reduction of electrospun SiO2 nanofibers', *Scientific Reports*, vol. 5, no. 1, Feb. 2015. DOI: 10.1038/srep08246.

[42] B. Jiang, S. Zeng, H. Wang *et al.*, 'Dual core–shell structured si@siox@c nanocomposite synthesized via a one-step pyrolysis method as a highly stable anode material for lithium-ion batteries', *ACS Applied Materials & Interfaces*, vol. 8, no. 46, pp. 31 611–31 616, Nov. 2016. DOI: 10.1021/acsami.6b09775.

[43] W.-S. Chang, C.-M. Park, J.-H. Kim, Y.-U. Kim, G. Jeong and H.-J. Sohn, 'Quartz (SiO2): A new energy storage anode material for li-ion batteries', *Energy & Environmental Science*, vol. 5, no. 5, p. 6895, 2012. DOI: 10.1039/c2ee00003b.

[44] B. Gao, S. Sinha, L. Fleming and O. Zhou, 'Alloy formation in nanostructured silicon', *Advanced Materials*, vol. 13, no. 11, pp. 816–819, Jun. 2001. DOI: 10.1002/1521-4095(200106)13:11⟨816::aid-adma816⟩3.0.co;2-p.

[45] X. Liu, Y. Chen, H. Liu and Z.-Q. Liu, 'SiO 2 @c hollow sphere anodes for lithium-ion batteries', *Journal of Materials Science & Technology*, vol. 33, no. 3, pp. 239–245, Mar. 2017. DOI: 10.1016/j.jmst.2016.07.021.

[46] G. Lener, M. Otero, D. Barraco and E. Leiva, 'Energetics of silica lithiation and its applications to lithium ion batteries', *Electrochimica Acta*, vol. 259, pp. 1053–1058, Jan. 2018. DOI: 10.1016/j.electacta.2017.10.126.

[47] Q. Sun, B. Zhang and Z.-W. Fu, 'Lithium electrochemistry of SiO2 thin film electrode for lithium-ion batteries', *Applied Surface Science*, vol. 254, no. 13, pp. 3774–3779, Apr. 2008. DOI: 10.1016/j.apsusc.2007.11.058.

[48] H. Li and H. Zhou, 'Enhancing the performances of li-ion batteries by carbon-coating: Present and future', *Chem. Commun.*, vol. 48, no. 9, pp. 1201–1217, 2012. DOI: 10.1039/c1cc14764a.

[49] J. Meng, Y. Cao, Y. Suo, Y. Liu, J. Zhang and X. Zheng, 'Facile fabrication of 3d SiO2@graphene aerogel composites as anode material for lithium ion batteries', *Electrochimica Acta*, vol. 176, pp. 1001–1009, Sep. 2015. DOI: 10.1016/j.electacta.2015.07.141.

[50] N. Yan, F. Wang, H. Zhong *et al.*, 'Hollow porous SiO2 nanocubes towards high-performance anodes for lithium-ion batteries', *Scientific Reports*, vol. 3, no. 1, Mar. 2013. DOI: 10.1038/srep01568.

[51] J. Tu, Y. Yuan, P. Zhan *et al.*, 'Straightforward approach toward SiO2 nanospheres and their superior lithium storage performance', *The Journal of Physical Chemistry C*, vol. 118, no. 14, pp. 7357–7362, Mar. 2014. DOI: 10.1021/jp5011023.

[52] C. Liang, L. Zhou, C. Zhou *et al.*, 'Submicron silica as high-capacity lithium storage material with superior cycling performance', *Materials Research Bulletin*, vol. 96, pp. 347–353, Dec. 2017. DOI: 10.1016/j.materresbull.2017.03.072.

[53] X. Yang, H. Huang, Z. Li, M. Zhong, G. Zhang and D. Wu, 'Preparation and lithium-storage performance of carbon/silica composite with a unique porous bicontinuous nanostructure', *Carbon*, vol. 77, pp. 275–280, Oct. 2014. DOI: 10.1016/j.carbon.2014.05.030.

[54] C.-Y. Chou and G. S. Hwang, 'Lithiation behavior of silicon-rich oxide (SiO1/3): A first-principles study', *Chemistry of Materials*, vol. 25, no. 17, pp. 3435–3440, Aug. 2013. DOI: 10.1021/cm401303n.

[55] F. Lepoivre, D. Larcher and J.-M. Tarascon, 'Electrochemical activation of silica for enhanced performances of si-based electrodes', *Journal of The Electrochemical Society*, vol. 163, no. 13, A2791–A2796, 2016. DOI: 10.1149/2.1221613jes.

[56] J. Yang, 'SiOx-based anodes for secondary lithium batteries', *Solid State Ionics*, vol. 152-153, pp. 125–129, Dec. 2002. DOI: 10.1016/s0167-2738(02)00362-4.

[57] A. Raza, S. Y. Kim, J.-H. Choi, J.-S. Kim, M.-S. Park and S.-M. Lee, 'Crystallinity-controlled siox anode material prepared through a salt-assisted magnesiothermic reduction for lithium-ion batteries', *International Journal of Energy Research*, vol. 46, no. 13, pp. 18 269–18 277, Jul. 2022. DOI: 10.1002/er.8443.

[58] H. Ruan, S. Guo, L. Zhang *et al.*, 'Boosting lithium storage performance of diatomite derived si/SiOx micronplates via rationally regulating the composition, morphology and crystalline structure', *Ceramics International*, vol. 48, no. 12, pp. 17 510–17 517, Jun. 2022. DOI: 10.1016/j.ceramint.2022.03.015.

[59] C. Yang, Y. Zhang, J. Zhou *et al.*, 'Hollow si/SiOx nanosphere/nitrogen-doped carbon superstructure with a double shell and void for high-rate and long-life lithium-ion storage', *Journal of Materials Chemistry A*, vol. 6, no. 17, pp. 8039–8046, 2018. DOI: 10.1039/c8ta00010g.

[60] B.-C. Yu, Y. Hwa, C.-M. Park and H.-J. Sohn, 'Reaction mechanism and enhancement of cyclability of SiO anodes by surface etching with NaOH for li-ion batteries', *Journal of Materials Chemistry A*, vol. 1, no. 15, p. 4820, 2013. DOI: 10.1039/c3ta00045a.

[61] Q. Pan, P. Zuo, T. Mu *et al.*, 'Improved electrochemical performance of micro-sized SiO-based composite anode by prelithiation of stabilized lithium metal powder', *Journal of Power Sources*, vol. 347, pp. 170–177, Apr. 2017. DOI: 10.1016/j.jpowsour.2017.02.061.

[62] K. Yasuda, Y. Kashitani, S. Kizaki, K. Takeshita, T. Fujita and S. Shimosaki, 'Thermodynamic analysis and effect of crystallinity for silicon monoxide negative electrode for lithium ion batteries', *Journal of Power Sources*, vol. 329, pp. 462–472, Oct. 2016. DOI: 10.1016/j.jpowsour.2016.08.110.

[63] M. Zhang, N. Liang, D. Hao *et al.*, 'Recent advances of SiOx-based anodes for sustainable lithium-ion batteries', *Nano Research Energy*, pp. 1–23, May 2023. DOI: 10.26599/nre.2023.9120077.

[64] S. Chae, S.-H. Choi, N. Kim, J. Sung and J. Cho, 'Integration of graphite and silicon anodes for the commercialization of high-energy lithium-ion batteries', *Angewandte Chemie International Edition*, vol. 59, no. 1, pp. 110–135, Oct. 2019. DOI: 10.1002/anie.201902085.

[65] S. Y. Kim, J. Lee, B.-H. Kim, Y.-J. Kim, K. S. Yang and M.-S. Park, 'Facile synthesis of carbon-coated silicon/graphite spherical composites for high-performance lithium-ion batteries', *ACS Applied Materials Interfaces*, vol. 8, no. 19, pp. 12 109–12 117, May 2016. DOI: 10.1021/acsami.5b11628.

[66] M. Ko, S. Chae, J. Ma *et al.*, 'Scalable synthesis of silicon-nanolayer-embedded graphite for high-energy lithium-ion batteries', *Nature Energy*, vol. 1, no. 9, Sep. 2016. DOI: 10.1038/nenergy.2016.113.

[67] Q. Xu, J.-Y. Li, J.-K. Sun, Y.-X. Yin, L.-J. Wan and Y.-G. Guo, 'Watermelon-inspired si/c microspheres with hierarchical buffer structures for densely compacted lithium-ion battery anodes', *Advanced Energy Materials*, vol. 7, no. 3, p. 1 601 481, Oct. 2016. DOI: 10.1002/aenm.201601481.

[68] S. He, S. Huang, S. Wang, I. Mizota, X. Liu and X. Hou, 'Considering critical factors of silicon/graphite anode materials for practical high-energy lithium-ion battery applications', *Energy & Fuels*, vol. 35, no. 2, pp. 944–964, Dec. 2020. DOI: 10.1021/acs.energyfuels.0c02948.

[69] N. Kim, S. Chae, J. Ma, M. Ko and J. Cho, 'Fast-charging high-energy lithium-ion batteries via implantation of amorphous silicon nanolayer in edge-plane activated graphite anodes', *Nature Communications*, vol. 8, no. 1, Oct. 2017. DOI: 10.1038/s41467-017-00973-y.

[70] X. Li, P. Yan, X. Xiao *et al.*, 'Design of porous si/c–graphite electrodes with long cycle stability and controlled swelling', *Energy & Environmental Science*, vol. 10, no. 6, pp. 1427–1434, 2017. DOI: 10.1039/c7ee00838d.

[71] M. Klett, J. A. Gilbert, K. Z. Pupek, S. E. Trask and D. P. Abraham, 'Layered oxide, graphite and silicon-graphite electrodes for lithium-ion cells: Effect of electrolyte composition and cycling windows', *Journal of The Electrochemical Society*, vol. 164, no. 1, A6095–A6102, Oct. 2016. DOI: 10.1149/2.0131701jes.

[72] N. Liu, K. Huo, M. T. McDowell, J. Zhao and Y. Cui, 'Rice husks as a sustainable source of nanostructured silicon for high performance li-ion battery anodes', *Scientific Reports*, vol. 3, no. 1, May 2013. DOI: 10.1038/srep01919.

[73] J. Liu, P. Kopold, P. A. van Aken, J. Maier and Y. Yu, 'Energy storage materials from nature through nanotechnology: A sustainable route from reed plants to a silicon anode for lithium-ion batteries', *Angewandte Chemie International Edition*, vol. 54, no. 33, pp. 9632–9636, Jun. 2015. DOI: 10.1002/anie.201503150.

[74] J. Bradbury, 'Nature's nanotechnologists: Unveiling the secrets of diatoms', *PLoS Biology*, vol. 2, no. 10, e306, Oct. 2004. DOI: 10.1371/journal.pbio.0020306.

[75] D. Zhang, Y. Wang, J. Cai, J. Pan, X. Jiang and Y. Jiang, 'Bio-manufacturing technology based on diatom micro- and nanostructure', *Chinese Science Bulletin*, vol. 57, no. 30, pp. 3836–3849, Sep. 2012. DOI: 10.1007/s11434-012-5410-x.

[76] R. Flower, 'DIATOM METHODS | diatomites: Their formation, distribution, and uses', in *Encyclopedia of Quaternary Science*, Elsevier, 2013, pp. 501–506. DOI: 10.1016/b978-0-444-53643-3.00220-x.

[77] M.-S. Wang, L.-Z. Fan, M. Huang, J. Li and X. Qu, 'Conversion of diatomite to porous si/c composites as promising anode materials for lithium-ion batteries', *Journal of Power Sources*, vol. 219, pp. 29–35, Dec. 2012. DOI: 10.1016/j.jpowsour.2012.06.102.

[78] N. Khelifa, J.-P. Basly, B. Hamdi and M. Baudu, 'Preparation of novel diatomite-based composites: Applications in organic effluents sorption', *Desalination and Water Treatment*, vol. 57, no. 27, pp. 12 443–12 452, Jun. 2015. DOI: 10.1080/19443994.2015.1052994.

[79] J. Sheehan, T. Dunahay, J. Benemann and P. Roessler, 'Look back at the u.s. department of energys aquatic species program: Biodiesel from algae close-out report', Tech. Rep., Jul. 1998. DOI: 10.2172/15003040.

[80] D. D.-W. Tsai, P. H. Chen and R. Ramaraj, 'The potential of carbon dioxide capture and sequestration with algae', *Ecological Engineering*, vol. 98, pp. 17–23, Jan. 2017. DOI: 10.1016/j.ecoleng.2016.10.049.

[81] Y. Tan, T. Jiang and G. Z. Chen, 'Mechanisms and product options of magnesiothermic reduction of silica to silicon for lithium-ion battery applications', *Frontiers in Energy Research*, vol. 9, Mar. 2021. DOI: 10.3389/fenrg.2021.651386.

[82] A. Rasouli, K. E. Herstad, J. Safarian and G. Tranell, 'Magnesiothermic reduction of natural quartz', *Metallurgical and Materials Transactions B*, vol. 53, no. 4, pp. 2132–2142, Apr. 2022. DOI: 10.1007/s11663-022-02513-6.

[83] F. Beguin and E. Frackowiak, Eds., *Carbons for Electrochemical Energy Storage and Conversion Systems*. CRC Press, Nov. 2009. DOI: 10.1201/9781420055405.

[84] C. Julien and Z. Stoynov, Eds., *Materials for Lithium-Ion Batteries*. Springer Netherlands, 2000. DOI: 10.1007/978-94-011-4333-2.

[85] W. Zhou and Z. L. Wang, Eds., *Scanning Microscopy for Nanotechnology*. Springer New York, 2007. DOI: 10.1007/978-0-387-39620-0.

[86] D. B. Williams and C. B. Carter, *Transmission Electron Microscopy*. Springer US, 2009. DOI: 10.1007/978-0-387-76501-3.

[87] N. Yao, 'Focused ion beam systems', N. Yao, Ed., Sep. 2007. DOI: 10.1017/cbo9780511600302.

[88] Y. Waseda, E. Matsubara and K. Shinoda, *X-Ray Diffraction Crystallography*. Springer Berlin Heidelberg, 2011. DOI: 10.1007/978-3-642-16635-8.

[89] S.-M. Bak, Z. Shadike, R. Lin, X. Yu and X.-Q. Yang, 'In situ/operando synchrotron-based x-ray techniques for lithium-ion battery research', *NPG Asia Materials*, vol. 10, no. 7, pp. 563–580, Jul. 2018. DOI: 10.1038/s41427-018-0056-z.

[90] O. A. Drozhzhin, I. V. Tereshchenko, H. Emerich, E. V. Antipov, A. M. Abakumov and D. Chernyshov, 'An electrochemical cell with sapphire windows for operando synchrotron x-ray powder diffraction and spectroscopy studies of high-power and high-voltage electrodes for metal-ion batteries', *Journal of Synchrotron Radiation*, vol. 25, no. 2, pp. 468–472, Feb. 2018. DOI: 10.1107/s1600577517017489.

[91] M. Thommes, K. Kaneko, A. V. Neimark *et al.*, 'Physisorption of gases, with special reference to the evaluation of surface area and pore size distribution (IUPAC technical report)', *Pure and Applied Chemistry*, vol. 87, no. 9-10, pp. 1051–1069, Jul. 2015. DOI: 10.1515/pac-2014-1117.

[92] C. Prescher and V. B. Prakapenka, 'Dioptas: A program for reduction of two-dimensional x-ray diffraction data and data exploration', *High Pressure Research*, vol. 35, no. 3, pp. 223–230, Jun. 2015. DOI: 10.1080/08957959.2015.1059835.

[93] K. K. Larbi, M. Barati and A. McLean, 'Reduction behaviour of rice husk ash for preparation of high purity silicon', *Canadian Metallurgical Quarterly*, vol. 50, no. 4, pp. 341–349, Oct. 2011. DOI: 10.1179/000844311x13117643274677.

[94] J. Entwistle, A. Rennie and S. Patwardhan, 'A review of magnesiothermic reduction of silica to porous silicon for lithium-ion battery applications and beyond', *Journal of Materials Chemistry A*, vol. 6, no. 38, pp. 18 344–18 356, 2018. DOI: 10.1039/c8ta06370b.

[95] M. J. Loveridge, M. J. Lain, I. D. Johnson *et al.*, 'Towards high capacity li-ion batteries based on silicon-graphene composite anodes and sub-micron v-doped LiFePO4 cathodes', *Scientific Reports*, vol. 6, no. 1, Nov. 2016. DOI: 10.1038/srep37787.

[96] T. Chen, J. Wu, Q. Zhang and X. Su, 'Recent advancement of SiOx based anodes for lithium-ion batteries', *Journal of Power Sources*, vol. 363, pp. 126–144, Sep. 2017. DOI: 10.1016/j.jpowsour.2017.07.073.

[97] T. Kim, H. Li, R. Gervasone, J. M. Kim and J. Y. Lee, 'Review on improving the performance of SiOx anodes for a lithium-ion battery through insertion of heteroatoms: State of the art and outlook', *Energy & Fuels*, Jun. 2023. DOI: 10.1021/acs.energyfuels.3c00785.

[98] M. N. Obrovac and L. Christensen, 'Structural changes in silicon anodes during lithium insertion/extraction', *Electrochemical and Solid-State Letters*, vol. 7, no. 5, A93, 2004. DOI: 10.1149/1.1652421.

[99] M. N. Obrovac and L. J. Krause, 'Reversible cycling of crystalline silicon powder', *Journal of The Electrochemical Society*, vol. 154, no. 2, A103, 2007. DOI: 10.1149/1.2402112.

[100] C. L. Berhaut, D. Z. Dominguez, P. Kumar *et al.*, 'Multiscale multiphase lithiation and delithiation mechanisms in a composite electrode unraveled by simultaneous operando small-angle and wide-angle x-ray scattering', *ACS Nano*, vol. 13, no. 10, pp. 11 538–11 551, Sep. 2019. DOI: 10.1021/acsnano.9b05055.

# Appendix

## A Mass loading of cells

The mass loading of the active material of the cells are given in Table A.1

**Table A.1:** Active material mass loading of different cell compositions. Cells that underwent an activation cycle at 50 $mAg^{-1}$ is denoted with an A and cells that started cycling directly at 100 $mAg^{-1}$ is denoted NA. The table also includes the mass loading for the anode used in the in-situ cell.

| Cell | Mass loading [$mgcm^{-2}$] |
|---|---|
| $SiO_2$-A | 0.229 |
| $SiO_x$-A | 0.390 |
| $SiO_x$-NA | 0.306 |
| $SiO_x$/Gr-A | 0.671 |
| $SiO_x$/Gr-NA | 0.640 |
| In-situ cell | 0.361 |

## B Additional SEM micrographs

Additional SEM micrographs of agglomorated $SiO_x$ are given in Figure B.1 and B.2.

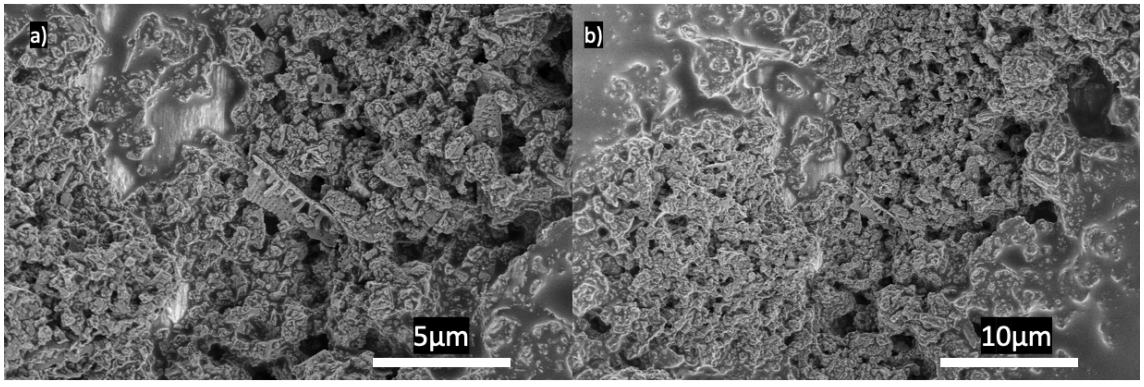


**Figure B.1:** SEM micrographs of agglomerated diatom frustules post MgTR.

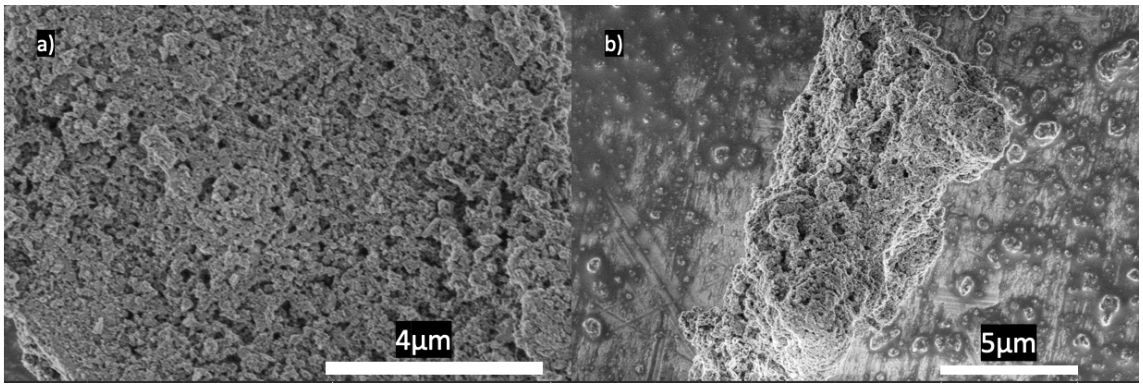


**Figure B.2:** SEM micrographs of agglomerated diatom frustules post MgTR and acid treatment.

# C Additional EDS

The map sum spectra corresponding to the EDS maps given in Figure 4.11 and 4.12, are given in Figure C.1 and Figure C.2 respectively.

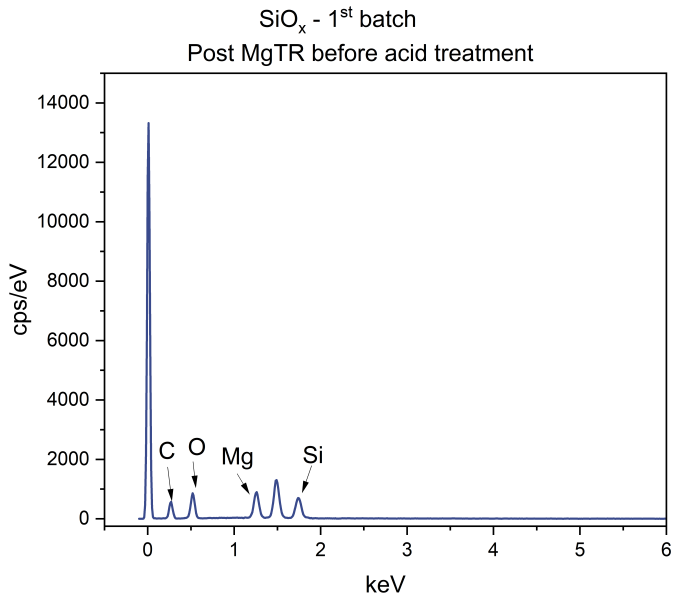


**Figure C.1:** Map sum spectra corresponding to the EDS maps of post MgTR $SiO_x$ given in Figure 4.11. The unmarked peak in between Si and Mg belongs to Al, originating from the sample holder.

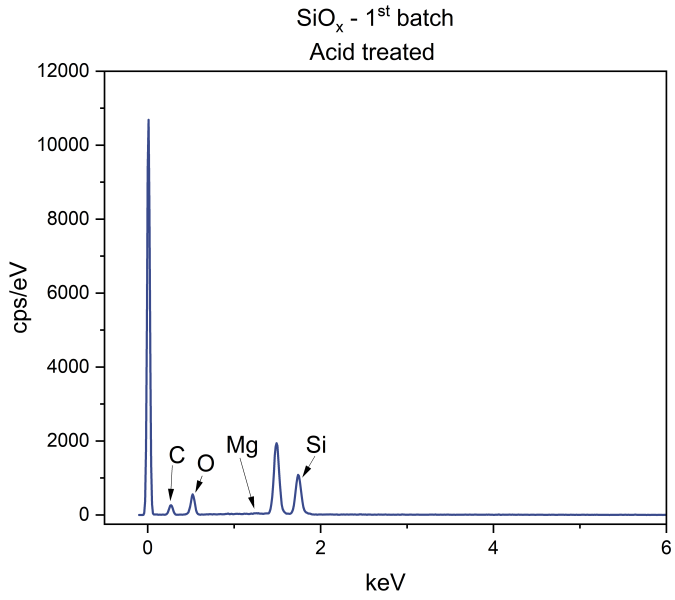


**Figure C.2:** Map sum spectra corresponding to the EDS maps of post MgTR and acid treated $SiO_x$ given in Figure 4.12. The unmarked peak in between Si and Mg belongs to Al, originating from the sample holder.

EDS maps and corresponding map sum spectra for the second batch of $SiO_x$ synthesized with 1:1 molar ratio at 650°C before acid treatment is given in Figure C.3 and C.4.

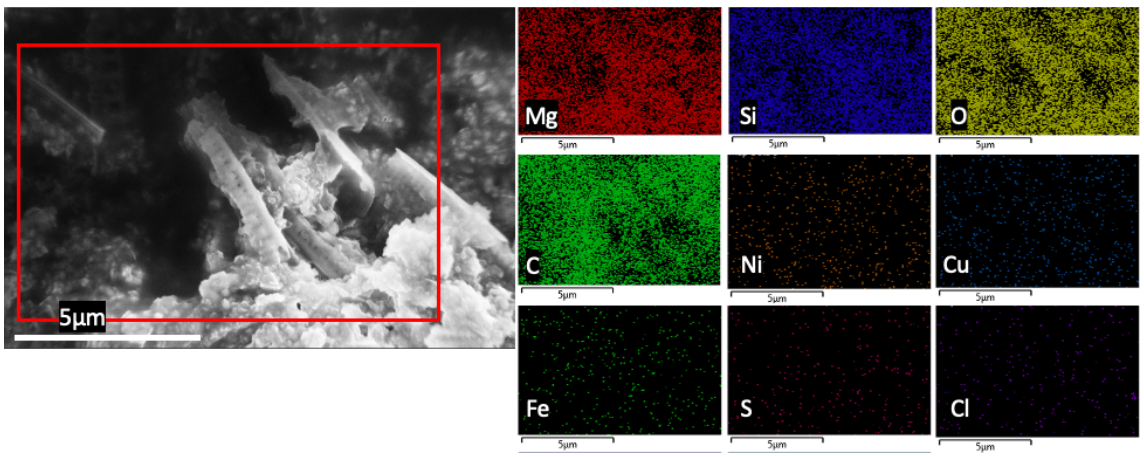


**Figure C.3:** SEM micrograph and EDS maps of $SiO_x$ particles of the second synthesis with 1:1 molar ratio at 650°C post MgTR. EDS maps acquired from area marked with red.

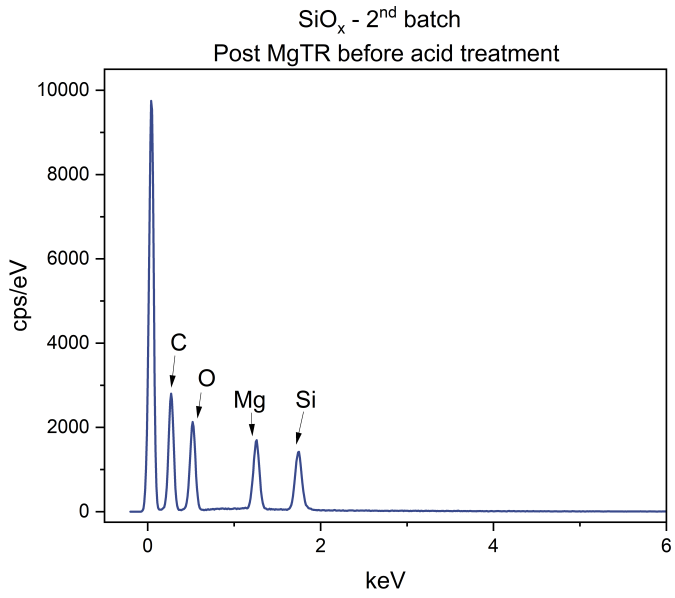


**Figure C.4:** Map sum spectra corresponding to the EDS maps of post MgTR $SiO_x$ given in Figure C.3.

EDS maps and corresponding map sum spectra for the second batch of $SiO_x$ synthesized with 1:1 molar ratio at 650°C after acid treatment is given in Figure C.5 and Figure C.6.

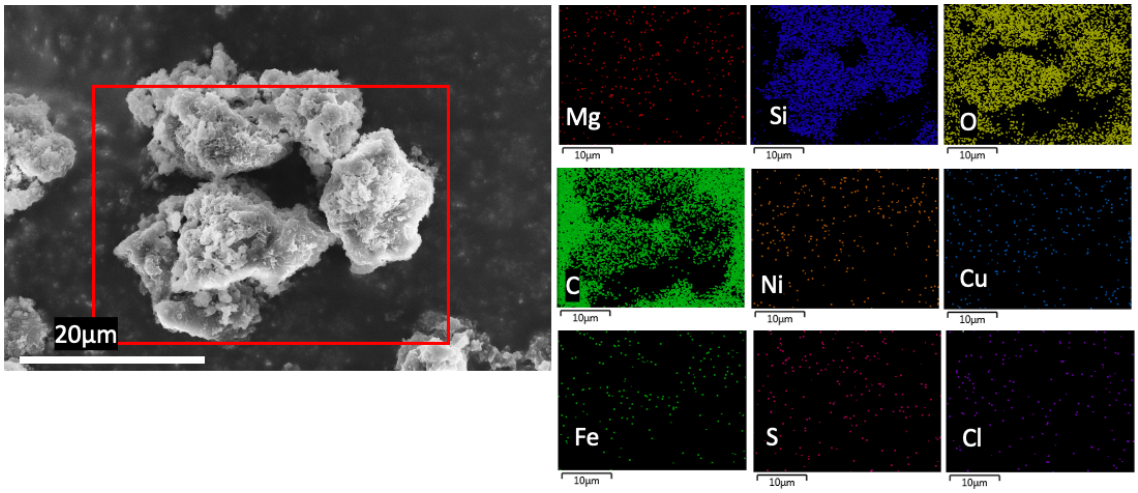


**Figure C.5:** SEM micrograph and EDS maps of $SiO_x$ particles of the second synthesis with 1:1 molar ratio at 650°C post MgTR and acid treatment. EDS maps acquired from area marked with red.

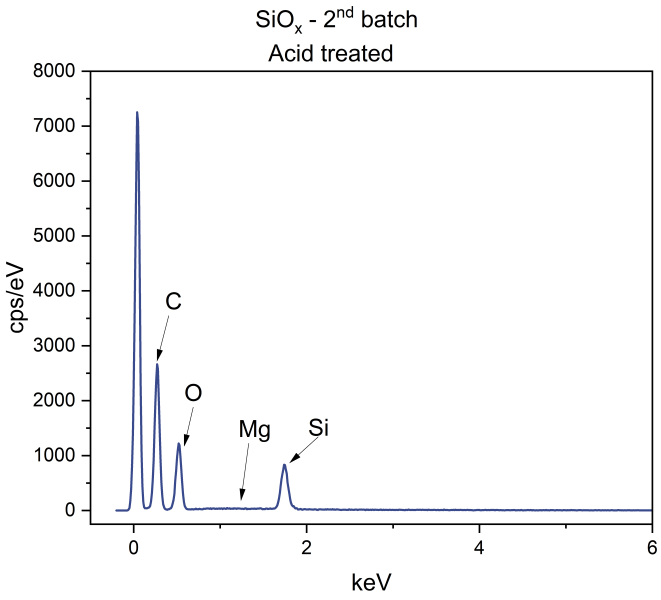


**Figure C.6:** Map sum spectra corresponding to the EDS maps of post MgTR and acid treatment $SiO_x$ given in Figure C.5.

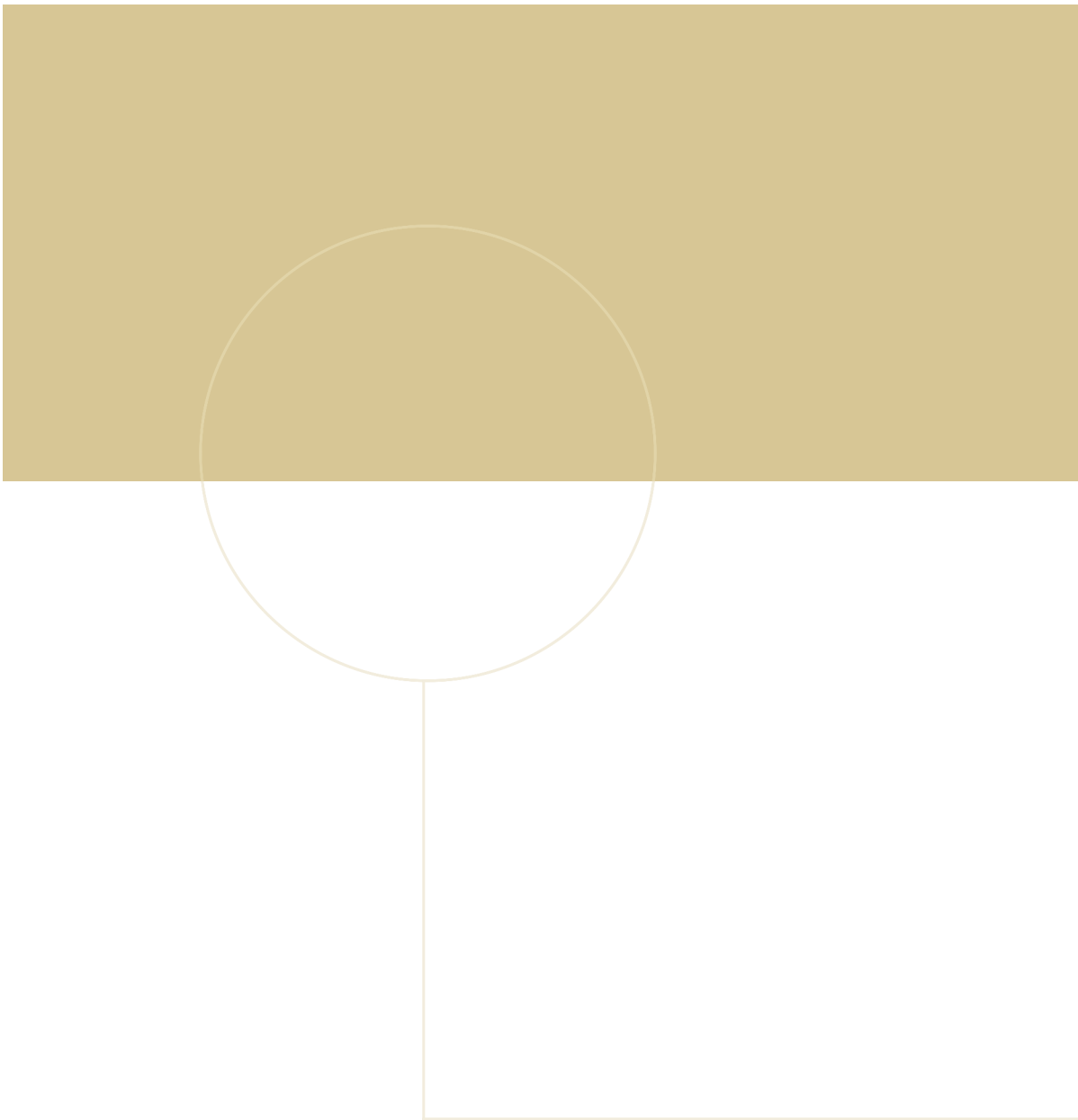

NTNU

Norwegian University of
Science and Technology